

**THERMAL AND MECHANICAL BEHAVIOR OF A  
Y<sub>3</sub>AL<sub>5</sub>O<sub>12</sub> BI-CRYSTAL**

**by**

**Maria I. Peters**

ProQuest Number: 10796851

All rights reserved

INFORMATION TO ALL USERS

The quality of this reproduction is dependent upon the quality of the copy submitted.

In the unlikely event that the author did not send a complete manuscript and there are missing pages, these will be noted. Also, if material had to be removed, a note will indicate the deletion.



ProQuest 10796851

Published by ProQuest LLC (2019). Copyright of the Dissertation is held by the Author.

All rights reserved.

This work is protected against unauthorized copying under Title 17, United States Code  
Microform Edition © ProQuest LLC.

ProQuest LLC.  
789 East Eisenhower Parkway  
P.O. Box 1346  
Ann Arbor, MI 48106 – 1346

A thesis submitted to the Faculty and the Board of Trustees of the Colorado School of Mines in partial fulfillment of the requirements for the degree of Doctor of Philosophy (Materials Science).

Golden, Colorado

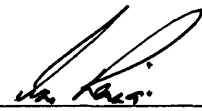
Date 4/5/2000

Signed: \_\_\_\_\_



Maria Isela Peters

Approved \_\_\_\_\_



Ivar Reimanis  
Thesis Advisor

Golden, Colorado

Date 4/7/00

\_\_\_\_\_  
John J. Moore  
Head, Metallurgical and Materials  
Engineering Department

## ABSTRACT

A  $\Sigma 5$  yttrium aluminum garnet ( $Y_3Al_5O_{12}$ , YAG) bi-crystal was examined after high temperature ( $>1550^\circ\text{C}$ ) deformation using a variety of techniques with the intent of identifying mechanisms of deformation. Two experimental approaches were used. First, high temperature compression experiments were performed using a compression apparatus which was developed here. For these experiments, the boundary was oriented at 45 degrees to the compression axis to maximize the resolved shear stress on the grain boundary. Observations of dislocations and directional sliding imply that dislocations are involved in the mechanism of sliding. Second, grain boundary grooving experiments were conducted on the bi-crystal to characterize diffusion in YAG. Peak to peak measurements of the grooves were measured and applied to Mullins' grain boundary grooving theory which resulted in diffusion coefficients calculations made at different temperatures to estimate the role of diffusion in the overall deformation of the grain boundary. The diffusion coefficient is expressed as:

$$D(Y_3Al_5O_{12}) = 3.9 \times 10^{-10} \exp(-330 \pm 75 (\text{kJ/mol})/RT) \text{m}^2/\text{s}$$

An activation energy of 330 kJ/mol was calculated and found to be in close agreement with previous measurements of oxygen volume diffusion in YAG [1] suggesting that diffusion of YAG is limited by the diffusion rate of oxygen ions.

It is concluded that deformation of the boundary occurs through both diffusion and dislocation motion. Implications regarding the deformation of polycrystalline ceramics are discussed.

## TABLE OF CONTENTS

	Page
<b>ABSTRACT</b> .....	iii
<b>LIST OF FIGURES</b> .....	vii
<b>LIST OF TABLES</b> .....	xv
<b>ACKNOWLEDGMENTS</b> .....	xvi
<b>DEDICATION</b> .....	xvii
<b>1. INTRODUCTION</b> .....	1
1.1.MOTIVATION FOR STUDY .....	1
1.2.PROJECT OVERVIEW .....	3
<b>2. BACKGROUND INFORMATION</b> .....	6
2.1.TAILORING OF GRAIN BOUNDARIES.....	6
2.2.OXIDE CERAMIC MATERIALS FOR STRUCTURAL APPLICATIONS.....	7
2.3.DIFFUSION INDUCED DEFORMATION IN CERAMICS .....	10
2.3.1. <i>High Temperature Diffusion Aided Deformation</i> .....	10
2.3.2. <i>Lifshitz Sliding</i> .....	11
2.4.DISLOCATION INDUCED DEFORMATION IN CERAMICS .....	12
2.4.1. <i>Dislocations in Oxides</i> .....	12
2.5.CRITICAL RESOLVED SHEAR STRESS .....	17
2.5.1. <i>Slip</i> .....	20
2.5.2. <i>Rachinger Sliding</i> .....	21
2.6.BOUNDARY SHAPE CHANGES .....	23

2.7.MIGRATION.....	24
2.8.CAVITATION IN CERAMICS.....	26
2.9.COMBINED PROCESSES .....	27
2.10.SINGLE CRYSTAL VS. POLYCRYSTAL DEFORMATION.....	28
2.10.1.Mullin's Theory.....	31
2.10.2.Diffusion Coefficient .....	34
2.10.3.Diffusion Mechanisms.....	35
<b>3. LITERATURE SURVEY .....</b>	<b>38</b>
3.1.GENERAL MECHANICAL BEHAVIOR.....	39
3.2.DEFORMATION MECHANISMS .....	41
3.3.ACTIVATION ENERGY .....	42
3.4.LOW VS. HIGH STRAIN RATES.....	45
3.5.SUMMARY.....	46
<b>4. EXPERIMENTAL DETAILS .....</b>	<b>47</b>
4.1.PRODUCTION OF BI-CRYSTALS .....	47
4.2.COMPRESSION TESTING .....	48
4.3.GRAIN BOUNDARY GROOVING .....	52
4.4.ANALYSIS TECHNIQUES .....	55
4.4.1.Profilometry.....	56
4.4.2.Atomic Force Microscopy.....	56
4.4.3.Electron Microscopy.....	58
<b>5. RESULTS.....</b>	<b>61</b>
5.1.DISLOCATION STRUCTURE OF AS-RECEIVED BOUNDARY .....	62
5.2.SAMPLE ORIENTATION.....	62
5.3.COMPRESSION TESTING .....	65
5.4.FRACTURE AT GRAIN BOUNDARY .....	68

5.5.TEM ANALYSIS OF DEFORMED BOUNDARY .....	69
5.6.SEM OF DEFORMED YAG BI-CRYSTAL .....	74
5.7.BOUNDARY STEPS.....	75
5.8.DIFFUSION COEFFICIENT MEASUREMENTS .....	83
5.9.GEOMETRY OF BOUNDARY GROOVES.....	88
<b>6. DISCUSSION.....</b>	<b>90</b>
6.1.GRAIN BOUNDARY QUALITY .....	90
6.1.1.Undeformed Boundary (Dislocations).....	90
6.1.2.Orientation Misfit.....	92
6.2.BI-CRYSTAL ORIENTATION .....	94
6.3.THE ROLE OF GRAIN BOUNDARY STEPS (GRAIN BOUNDARY SLIDING).....	95
6.4.DEFORMATION GRAIN BOUNDARY SHAPE.....	100
6.5.THE ROLE OF DISLOCATIONS AT THE BOUNDARY .....	102
6.5.1.Dislocations at Grain Boundaries .....	104
6.6.MIGRATION OF YAG GRAIN BOUNDARY (GRAIN BOUNDARY MOBILITY)	109
6.7.CAVITATION DEFORMATION OF YAG BOUNDARY .....	110
6.8.OBSERVATIONS ON MIGRATION AND SLIDING .....	112
6.9.OBSERVATIONS ON DISLOCATIONS .....	114
6.10.DIFFUSION COEFFICIENT CALCULATIONS .....	116
6.11.DEFORMATION MECHANISMS. ....	120
<b>7. SUMMARY AND CONCLUSIONS.....</b>	<b>121</b>
<b>APPENDIX.....</b>	<b>123</b>



## LIST OF FIGURES

Figure 1-1 The crystal structure of YAG [5]. .....	3
Figure 2-1 Frequency of $\Sigma$ grain boundaries for a directionally solidified Ni <sub>3</sub> Al material, which deforms up to 60% in tensile elongation[2]. .....	7
Figure 2-2 A detailed sketch of the yttrium iron garnet [9]. .....	9
Figure 2-3A sketch of a grain and grain boundary showing the atomic mobility for “Nabarro-Herring” and “Coble” creep. [13]. .....	11
Figure 2-4 Lifshitz sliding described by the sliding of grain boundaries aided by a diffusion mechanism[15]. .....	12
Figure 2-5 Dislocation glide-climb deformation mechanism, which occurs at higher temperatures. [13]. .....	14
Figure 2-6 A single crystal showing applied forces, slip direction, slip plane and angles between these planes, directions and axis of applied stresses [6]. .....	18
Figure 2-7 Sketch of YAG bi-crystal with possible (310) planes. The (310) planes are 45 degrees from the boundary and are the planes perpendicular to the compression axis. ....	19
Figure 2-8 A model describing the amount of strain needed to plastically deform a lattice for a perfect crystal[2]. .....	20
Figure 2-9 A model describing the amount of strain needed to plastically deform a non-perfect crystal[13]. .....	21
Figure 2-10 A sketch of grains exhibiting Rachinger sliding under an applied stress ( $\sigma$ )[15]. .....	22
Figure 2-11 Grain boundary shape of a grain boundary exhibiting diffusive grain boundary sliding [22]. .....	23

Figure 2-12 Cavitation show mostly at two-grain facets on crept samples of Lucalox alumina tested at 1600°C [30].	26
Figure 2-13 Possible cavitation nucleation sites resulting from creep deformation for materials in general [30].	27
Figure 2-14 A sketch of combined deformation mechanisms resulting from an applied stress[13].	28
Figure 2-15 A frequency chart of deformation mechanisms for polycrystal materials[13].	30
Figure 2-16 A frequency chart of deformation mechanisms for single crystal materials[13].	30
Figure 2-17 A sketch of a grain boundary groove showing the equilibrium angle ( $\beta$ ),the two-dimensional axis used to describe the geometry of the growing boundary groove and the peak to peak distance ( $W$ ) [modified from 32].	31
Figure 2-18 Graph of diffusion coefficients plotted against the inverse of temperature for different ceramic materials [6].	36
Figure 2-19 Sketches showing the three grain boundary groove growth diffusion mechanism (evaporation/condensation, surface and volume diffusion)[redrawn from 34].	37
Figure 3-1 Stress-strain deformation curve for single crystal [135] YAG compressed at 1785°C at a constant strain rate of $4.5 \times 10^{-5}$ /sec. The sample deformed ~7% [4].	39
Figure 3-2 Stress-strain for single crystal [100] oriented YAG at 1700°C at a constant strain rate of $3.4 \times 10^{-6}$ /sec [35].	40
Figure 3-3 Stress-time curve obtained from a constant strain compression experiment on [111] oriented single crystal YAG at different temperatures[3].	41
Figure 3-4 Axial strain rate vs. axial steady state stress relationship for single crystal YAG. Comparison of different crystal orientations performed at 1635°C[3].	43
Figure 3-5 Stress exponents depicted on strain rate vs. stress relationships for two temperature regions: a)~1635°C and b)~1515°C[31].	44

Figure 3-6 Activation energies for polycrystalline and single crystalline YAG. Comparison of two studies (Corman and Parthasathary)[31].	45
Figure 4-1 Materials bonding chamber specifying chambers and guns. The production of the YAG bi-crystals required high vacuum to reduce boundary contamination and also required a tool to precisely orient the bonded planes[5].	48
Figure 4-2 Relative orientation of YAG compression samples with the bulk YAG bi-crystal. The boundary is 45° to the length of the compression axis.	49
Figure 4-3 YAG compression sample shown with a sketch of the position of the boundary with respect to the surface of the sample.	49
Figure 4-4 Compression testing apparatus showing the YAG rams used to compress the YAG sample, the self aligning ball and socket (#1) and the sapphire spacers used to avoid bonding of YAG/YAG surfaces in the hot zone.	51
Figure 4-5 Standard sample used for diffusion groove growth measurements. Sketch shows the positioning of the grain boundary with respect to the surface of the sample.	53
Figure 4-6 Cooling and heating curves of the furnace used to heat-treat the boundary to obtain grain boundary grooves.	54
Figure 4-7 Typical groove geometry of YAG grain boundary after heat-treating. The geometry of the groove varied in height with testing time.	55
Figure 4-8 A typical 20 micron scan obtained from the atomic force microscopy	57
Figure 4-9 Sketch of YAG bi-crystal compression sample showing sectioned TEM specimens.	59
Figure 4-10 Final TEM specimen mounted on copper ring. Arrows designate the ion beams.	60
Figure 5-1 Sketch of boundary and edge faces designated on the compression sample.	61
Figure 5-2 High-resolution image of $\Sigma 5$ YAG boundary after processing and before deformation [5].	63

Figure 5-3 YAG unit cell showing the relative orientations of the (210) boundary and the calculated slip system using Schmidt factors.....	64
Figure 5-4 Laue pattern of YAG bi-crystal.....	64
Figure 5-5 Stress-time curves for all compression experiments for the YAG bi-crystalline material. ....	66
Figure 5-6 Compliance curve of single crystal ram compression apparatus at 1700°C at a crosshead speed of $3.4 \times 10^{-5}$ . ....	67
Figure 5-7 Optical micrograph of as-received (non-deformed) boundary surface of YAG. ....	68
Figure 5-8 Optical micrograph of deformed boundary surface after 1.5% calculated strain.....	69
Figure 5-9 Transmission electron microscopy micrograph of the YAG (YAG1) grain boundary after ~0.7% ( $\pm 4\%$ ) deformation. 1600°C, $3.4 \times 10^{-5}$ in/min crosshead speed, in air. ....	71
Figure 5-10 Transmission electron microscopy image of tilted YAG (YAG1) boundary for a specimen deformed to ~0.7% ( $\pm 7\%$ , 20:1). 1600°C, $3.4 \times 10^{-5}$ in/min crosshead speed, in air. ....	71
Figure 5-11 Transmission electron microscopy image of a YAG (YAG1) deformed grain boundary (~0.6% $\pm 7\%$ , 20:1). Grain boundary is perpendicular to the image plane along the [001] direction.....	72
Figure 5-12 TEM images of the YAG bi-crystal tested at low stresses. Testing conditions: 1650°C, constant crosshead speed, in air. a) YAG bi-crystal. ~37 degree specimen tilt. 52,000X. ....	73
Figure 5-13 TEM image of YAG bi-crystal tested at high stress. Testing conditions: 1700°C, variable crosshead speed, in air. 89,000X. ....	74
Figure 5-14 SEM image of void formation at the grain boundary of a deformed YAG bi-crystal exposed after fracture at room temperature.....	75

Figure 5-15 Profilometry scan of a YAG (MP1) bi-crystal boundary face (Face A) surface after deformation. ....	76
Figure 5-16 Profilometry scan of a YAG (MP1) bi-crystal edge face (Face B) surface after deformation.....	77
Figure 5-17 Stress-time curve of constant low stress compression test performed on a YAG bi-crystal at 1650C. ....	79
Figure 5-18 Profilometer scan of a deformed YAG bi-crystal after a constant stress experiment at 1650°C. Scan was made on Face A-side 1.....	79
Figure 5-19 Profilometer scan of a deformed YAG bi-crystal after a constant stress experiment at 1650°C. Scan was made on Face A-side 2.....	80
Figure 5-20 Profilometer scan of a deformed YAG bi-crystal after a constant stress experiment at 1650°C. Scan was made on Face B-side 1.....	80
Figure 5-21 Profilometer scan of a deformed YAG bi-crystal after a constant stress experiment at 1650°C. Scan was made on Face B-side 2.....	81
Figure 5-22 Profilometer scan of a deformed YAG bi-crystal after a constant stress experiment at 1700°C. Scan was made on Face A-side 1.....	81
Figure 5-23 Profilometer scan of a deformed YAG bi-crystal after a constant stress experiment at 1700°C. Scan was made on Face A-side 2.....	82
Figure 5-24 Profilometer scan of a deformed YAG bi-crystal after a constant stress experiment at 1650°C. Scan was made on Face B-side 1.....	82
Figure 5-25 Profilometer scan of a deformed YAG bi-crystal after a constant stress experiment at 1650°C. Scan was made on Face B-side 2.....	83
Figure 5-26 Linear relationship between the groove growth and time for the YAG bi-crystal. ....	85
Figure 5-27 Mass pile up of the YAG bi-crystal boundary shown in an atomic force microscopy scan.....	86

Figure 5-28 Acceptable grain boundary groove geometries used for calculating the diffusion coefficient of YAG. ....	86
Figure 5-29 Graph of the diffusion and temperature data with error bars. ....	88
Figure 5-30 Atomic force microscopy scan of a migrating grain boundary as seen on a compression sample of the YAG bi-crystal after heat treating. ....	89
Figure 5-31 Atomic force microscopy profile showing a residual groove in a YAG bi-crystal compression sample after deformation. ....	89
Figure 6-1 TEM of $\Sigma 5$ YAG grain boundary before deformation [5]. Possible dislocations are present at the boundary. ....	91
Figure 6-2 Micrograph of the undeformed YAG boundary [5]. ....	91
Figure 6-3 Kikuchi pattern taken from one grain of the bi-crystal using an electron microscope. ....	93
Figure 6-4 Kikuchi pattern taken from second grain in the YAG bi-crystal. ....	93
Figure 6-5 YAG bi-crystal showing the boundary plane and the $\{111\}$ family of planes as determined by an x-ray technique. ....	94
Figure 6-6 Relative movement of bi-crystals past each other. ....	97
Figure 6-7 Graph illustrating the stress dependence of diffusion and dislocation mechanisms [9]. ....	98
Figure 6-8 Direction of slip of one YAG bi-crystal determined by surface step measurements. The boundary slid 79 degrees from the P direction. ....	100
Figure 6-9 AFM scan and profiles of the fractured YAG bi-crystal boundary surface. The features are measured to be a maximum of 250nm high. ....	101
Figure 6-10 TEM image of YAG bi-crystal boundary deformed under a high stress. A dislocation spacing of 84nm ( $\pm 5$ nm) was measured. ....	102
Figure 6-11 TEM image of YAG bi-crystal boundary deformed under a constant low stress stress. A dislocation spacing of 113nm ( $\pm 6$ nm) was measured. ....	103

Figure 6-12 YAG crystal structure viewed along [001] direction showing two possible planes which will result in grain boundary symmetry when rotated 180 degrees. [36].	105
Figure 6-13 Resulting grain boundary atomic positioning for planes A and B resulting from an atomic model. A top view of the model shows the structure formed at the boundary [36].	106
Figure 6-14 Two symmetric grain boundaries shown before dislocation and boundary interaction (14-a, c) and after interaction (14b,d)[38].	107
Figure 6-15 Possible dislocation splitting for BCC materials[39].	108
Figure 6-16 A simple sketch showing the movement of dislocations moving along the grain boundary of a grain[40].	109
Figure 6-17 TEM of the MP7 YAG bi-crystal showing voids approximately 1nm ( $\pm 0.2\text{nm}$ ) along the axis of the boundary	112
Figure 6-18 Surface of a zinc bi-crystal showing the movement and shape change of marker lines [23].	113
Figure 6-19 The correlation between grain boundary sliding and grain boundary migration for a zinc bi-crystal [23].	114
Figure 6-20 TEM micrograph of a deformed silicon grain boundary with intrinsic and partial dislocations [45].	115
Figure 6-21 Sketch of the different dislocations present at a deformed silicon grain boundary [45].	115

## LIST OF TABLES

Table 1-1 A number of important details about YAG including melting point and density. .....	4
Table 2-1 Most probable dislocations grown from melt in the [111] direction for YAG [16]......	16
Table 2-2 Calculated slip systems for YAG using most densely packed planes and directions [16]. .....	16
Table 2-3 Calculated slip planes for the orientation in Figure 2-10. ....	19
Table 3-1 Summary of deformation experiments performed on YAG single crystalline and polycrystalline. P=polycrystalline, S=single crystalline .....	38
Table 5-1 Experimental details of the compression experiments performed on the YAG bi-crystals. ....	67
Table 5-2 Details of the "peak-to-peak" measurements made on the YAG bi-crystalline material to determine the diffusion coefficient at different temperatures.....	87
Table 6-1 Measured steps using a profilometer for the high stress and low constant stress experiments on YAG bi-crystalline compression samples. ....	96
Table 6-2 Average atomic distances traveled by the YAG atoms in 2.5 hours. ....	117



## ACKNOWLEDGMENTS

I would first like to thank God for the strength and faith that I find in life.

Thank you to Dr. Reimanis who has given me considerable support and advice throughout this endeavor and to my thesis committee for their input.

I would also like to acknowledge those who have helped in their expertise: Goeff Campbell, Dennis Readey and John Petrovic. I would also like to thank Alice Jensen and Scott Pawelka who made all the major problems into minor ones. Special thanks also to Rick Hugo at Los Alamos National Laboratory for taking time to help out on the TEM. Thank you to Michael who helped out with the Laue scans and I am also indebted to the CCAC for its support.

I also want to thank all the students in CCAC and ACSEL who gave advice, warnings and ideas to help me with this thesis. Special thanks to Jesus Chapa, Roberto Souza, Augusto Kunrath and Michael Peters for their perspective on the research.

Finally, I want to thank all those who gave their personal support throughout these last four years: Michael, my family (especially to my grandma who keeps our family strong and united), The Peter's (especially to Ryan; for making some very difficult days worthwhile), Roberto & Bia, Jesus & Nannette, Jesus & Vicky, Mark, Augusto & Claudia, Raph & Francis, Ricardo & Carmen. Thank you all.

## **DEDICATION**

This dissertation is dedicated to my wonderful husband,  
Michael. Thanks for all the love and support.

## 1. INTRODUCTION

The need for materials with high toughness and high strength at high service temperatures has yielded interest in the deformation behavior of ceramics. Understanding the plasticity of ceramics at high temperatures is the key for developing these materials for structural applications. Grain boundaries can strongly affect the overall plastic flow and/or fracture of the material and the behavior of grain boundaries is especially important at high temperatures where the added energy of the systems allows for the initiation of deformation processes such as sliding, migration, segregation and fracture [2]. The following thesis focuses on the shear deformation (as induced by compression loads) of a specific boundary in an oxide. This deformation is studied through observations made using a number of surface and optical techniques. The present study focuses on using diffusion and dislocation mechanisms to describe boundary deformation.

### *1.1. Motivation for study*

The focus on grain boundaries for ceramic materials is important for mechanisms such as creep and grain boundary sliding. Very little is known of the deformation behavior of grain boundaries for ceramic systems due to the large variety of grain

boundary structures and the complexity of oxide crystal structures [2]. The deformation of grain boundaries may include diffusion of the material and dislocation motion. In ceramic materials, the large Peierl's stresses needed for dislocation motion result in deformation mechanisms that are dominated by diffusion. However, at higher temperatures and stresses, dislocation motion and activation of slip systems may also become significant.

Yttrium aluminum garnet ( $\text{Y}_3\text{Al}_5\text{O}_{12}$ ), usually referred to as YAG, is the most creep resistant oxide known [3]. It has a comparable and sometimes higher creep resistance than c-axis sapphire and is fairly isotropic in creep behavior [3]. In contrast, sapphire must be oriented to within a few degrees of the c-axis to exhibit high creep resistance [4]. The large crystal lattice and complex structure of YAG are reasons why this material is highly creep resistant. YAG has 160 atoms in its unit cell with a Burger's vector of  $\sim 10.4\text{\AA}$  (Figure 1-1) [5]. This large Burger's vector requires high stresses for dislocation movement.

YAG has been suggested as a fiber material for an alumina/YAG composite as it has a similar thermal expansion as alumina ( $\sim 9 \times 10^{-6}/^\circ\text{C}$ ) [6]. Other important properties of YAG are shown in table 1-1. These properties lead to a high interest in YAG for use in structural applications.

## 1.2. Project Overview

After deformation at high temperatures, a well-defined boundary in YAG was examined after deformation at high temperatures using a variety of materials characterization techniques. The  $\Sigma 5$  boundary bi-crystals made at Lawrence Livermore Laboratory were deformed in a high temperature

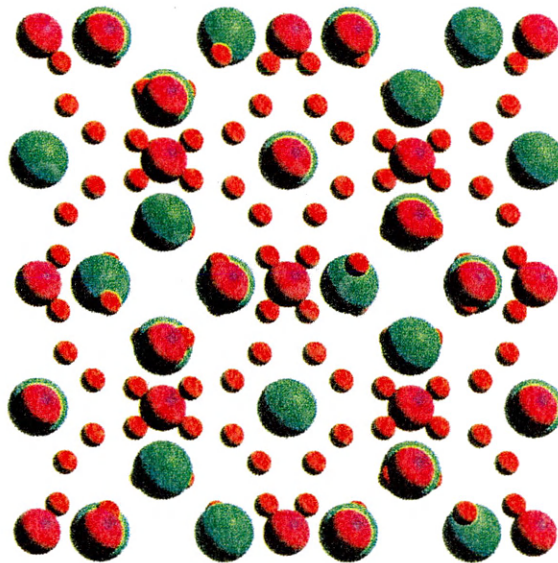


**Figure 1-1** The crystal structure of YAG has cubic symmetry. The red atoms are oxygen atoms. The purple atoms are aluminum atoms. The green atoms are yttrium atoms. YAG has 160 atoms per unit cell and has a lattice parameter of 12.01 Angstroms. [5].

**Table 1-1 A number of important details about YAG including melting point and density.**

Melting point	1940°C
Density	4.55 g/cm <sup>3</sup>
Stiffness	334 GPa
Thermal expansion	8.7E-6/°C
Burger's vector	10.4 Å, 1/2 <111>

furnace in air. The bi-crystals were compressed at a constant crosshead speed and at different temperatures between 1600°C and 1700°C. The deformation of this boundary was analyzed using profilometry, atomic force microscopy (AFM), optical microscopy, transmission electron microscopy (TEM) and scanning electron microscopy (SEM). Through the observation of dislocations, steps and other features formed at the surface of the compression samples and through groove geometry changes during deformation, the deformation behavior of this boundary was characterized.

Diffusion in YAG was also examined by performing a set of grain boundary grooving experiments between 1550°C and 1700°C. The resulting groove geometry at the boundary was related to the diffusion coefficient. Thus, the diffusion coefficient and the activation energy for diffusion of YAG can be indirectly measured.

These two techniques, grain boundary sliding and grain boundary grooving, were used for the first time to study high temperature behavior of YAG. This thesis describes the methods used to develop these techniques. In addition, significant insight concerning the high temperature deformation behavior in YAG has been obtained.

## 2. BACKGROUND INFORMATION

### 2.1. *Tailoring of Grain Boundaries*

It is important to understand the intrinsic behavior of grain boundaries in a material before the addition of dopants or the implementation of grain boundary altering processes is attempted. Material properties can be improved by the addition of second phases which, for ceramics, inhibit fracture but increase the creep rate (generally a grain boundary mechanism).

One well-known example of grain boundary tailoring is the increase in fracture toughness of  $\text{Ni}_3\text{Al}$  with the addition of boron. The mechanisms responsible for increased fracture toughness have been explained by either a boron-enhanced cohesive strength model or a boron-facilitated slip transfer model [7]. However, at elevated temperatures, a phenomenon called pesting reduces the material to an oxidized powder. Hirano found that processing  $\text{Ni}_3\text{Al}$  without boron but with a unidirectional solidification zone melting process increases the room temperature elongation to ~60% while retaining high temperature chemical stability [8]. This increase in ductility was attributed to a large number of low-angle boundaries and  $\Sigma 3$  coincidence boundaries.



Figure 2-1 shows the frequency of low angle and coincident boundaries found in directionally solidified Ni<sub>3</sub>Al [2].

The tailoring of oxide boundaries such as the YAG bi-crystal studied here can be more easily performed if the deformation mechanism of an undoped YAG boundary is identified. As in the case of Ni<sub>3</sub>Al, tailoring of the grain boundary in a material can greatly enhance the structural properties of the material.

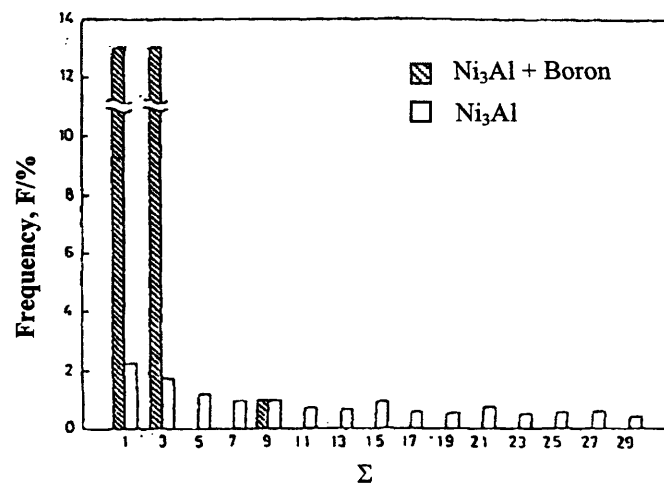


**Figure 2-1 Frequency of  $\Sigma$  grain boundaries for a directionally solidified Ni<sub>3</sub>Al material, which deforms up to 60% in tensile elongation. Note the high frequency of low Sigma boundaries ( $\Sigma$ 1 and  $\Sigma$ 3). Tailoring of grain boundaries increased the plasticity of Ni<sub>3</sub>Al significantly [2].**

## 2.2. Oxide Ceramic Materials for Structural Applications

Oxide ceramics are important for high temperature applications because of their stability in these environments. Their high temperature stability and corrosion resistance

is sometimes preferred to materials such as carbides, nitrides or silicides. However, oxides must be developed to exhibit higher fracture toughness and creep resistance if they are to be used at high temperatures and under applied stresses such as for reinforcement fibers. The study of a single oxide grain boundary should help develop an understanding of how grain boundaries need to be tailored to advance these materials into structural applications.

The primarily covalent and ionic bonding in ceramic materials provides a highly directional bond between atoms which requires high debonding energies thus making ceramics strong materials. However, cracks in the material are detrimental to the mechanical behavior of ceramics. Once a crack exists, the energy necessary to continue crack propagation is small and failure of the ceramic material can occur. Increasing the resistance to crack propagation will allow for plastic deformation of the ceramic material. Plastic deformation is difficult to achieve in oxide systems but testing at high temperatures and low strain rates helps induce plasticity.

The crystal structure of ceramics is an important characteristic that can dictate the material's structural behavior. In particular, the crystal structure of oxides is more easily understood by focusing on the position of the close-packed oxygen ions [6]. The anions and other cations are present mostly in interstitial sites of these oxygen structures. Some oxide structures include the rock salt structure, the spinel structure, rutile and the garnet structures [6]. YAG has the garnet structure as shown in Figure 2-2. [9]. In this structure, an octahedron, a tetrahedron and two dodecahedra build the garnet structure

[9]. (In this Figure only one dodecahedra is shown for clarity.) This figure illustrates the exact atomic positioning for yttrium iron garnet but the substitution of aluminum for iron will give the exact YAG structure.

The plastic behavior of oxides is also limited by their complicated crystal structure. These crystal structures result in large unit cells which in turn result in large Burger's vectors thus making dislocation movement (i.e. plasticity) difficult. The bonding character of the structure (directional bonding) also contributes to the difficulty in achieving plasticity.

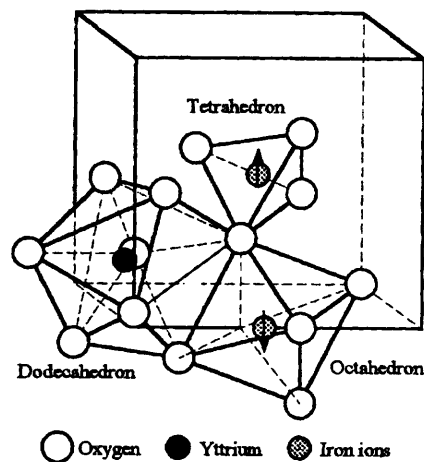


**Figure 2-2 A detailed sketch of the yttrium iron garnet. Note the tetrahedron, octahedron and dodecahedron, which make up this crystal structure. One dodecahedron is not shown for structure quality. Substituting the aluminum atom for the iron atom changes this molecule to YAG [9].**

### ***2.3. Diffusion Induced Deformation in Ceramics***

At elevated temperatures, the diffusion of atoms is an important deformation mechanism that must be examined. Diffusion can cause deformation of the material through bulk diffusion, grain boundary diffusion, diffusion-aided dislocation movement and a combination of the three.

#### ***2.3.1. High Temperature Diffusion Aided Deformation***

Deformation of ceramic materials at high temperatures tends to be dominated by diffusion-controlled mechanisms. High temperature diffusion controlled deformation (creep) consists of the diffusion of atoms along the grain boundaries of a polycrystal or the diffusion of atoms inside the grains of polycrystals. Creep is normally measured by testing in a compressive mode, as tensile tests in ceramics tend to drive cracks which result in failure of the specimen.

“Nabarro-Herring” creep [10, 11] is described as the deformation of a material by the diffusion of atoms in the lattice of grains in a polycrystal. The diffusion of atoms inside the grains of a material is driven by the difference in stress states of each individual grain. The flux of atoms occurs from regions experiencing compressive forces to regions experiencing tensile forces. “Coble” creep [12] involves atom diffusion along the grain boundaries in a polycrystal. Figure 2-3 shows “Nabarro-Herring” and “Coble” creep and details the movement of atoms from compressive regions to tensile regions, the flux of atoms along grain boundaries and the different diffusion coefficients that

represent each mechanism. In this figure,  $D_L$  and  $D_G$  are the diffusion coefficients for lattice diffusion and grain boundary diffusion respectively [13].

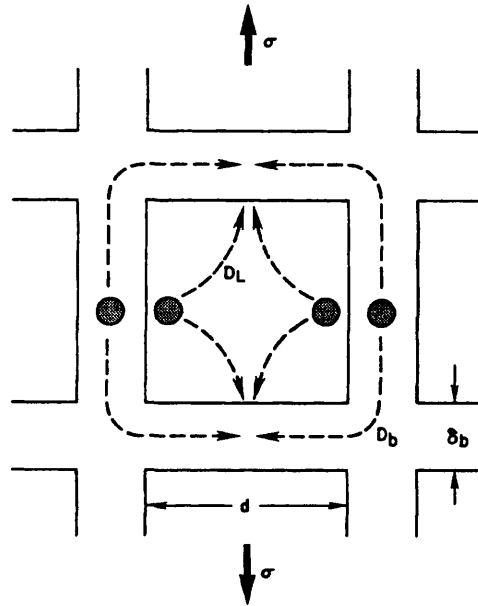


**Figure 2-3A sketch of a grain and grain boundary showing the atomic mobility for “Nabarro-Herring” and “Coble” creep.  $D_L$  and  $D_b$  are the lattice and grain boundary diffusivities,  $\delta_b$  is the grain boundary width and  $\sigma$  is the applied stress [13]. These are two deformation mechanisms responsible for high temperature deformation.**

### 2.3.2. Lifshitz Sliding

One model of sliding of grains along each other by the aid of a diffusional process, either “Nabarro-Herring”, or “Coble” creep, is termed Lifshitz [14] sliding. The resulting grain boundary shape from grain boundary sliding from a diffusional process is

shown in Figure 2-4. Accommodation of the grains to maintain "coherency" results in relative movement of the grains against each other [15]. The Lifshitz model of sliding requires the presence of vacancy sources or sinks to allow for diffusion of the species. Typically, these sinks (or sources) are grain boundaries [14]. Lifshitz has described a detailed analysis of the stresses developed during diffusion and the theory explaining grain size dependency. Small grain size results in surface diffusion as opposed to volume diffusion controlling the deformation of the grains [14].

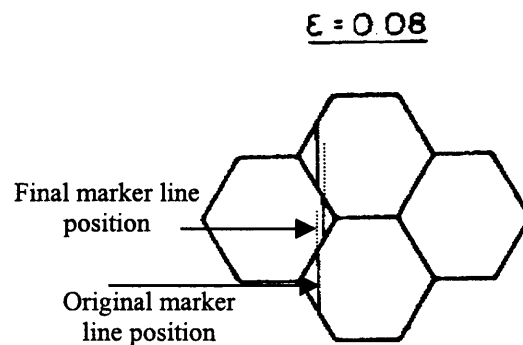


**Figure 2-4 Lifshitz sliding described by the sliding of grain boundaries aided by a diffusion mechanism. Note the shift in the marker lines, which is a result of the grain boundary accommodation [15]. Lifshitz sliding is a result of plastic deformation of the grains.**

## **2.4. Dislocation Induced Deformation in Ceramics**

### *2.4.1. Dislocations in Oxides*

The role of dislocations during deformation can change as the temperature of the system changes. At low temperatures, especially for ceramics, grain boundaries act as

barriers to dislocation motion and dislocation pile-ups are common [2]. Stresses concentrated at grain boundaries result in fracture if dislocation motion is inhibited. However, at higher temperatures ( $>1000^{\circ}\text{C}$  for oxide ceramics), these stresses are relaxed by processes such as grain boundary migration, sliding and fracture [2]. The relaxation of stresses by the aid of these processes results in plastic deformation around the grain boundary.

Dislocations can be present in materials by one of two sources. First, dislocations can be grown into the material during melt processing in single crystal growth. Second, dislocations can be mechanically introduced into the material by imposing stresses into the material that result in the formation of dislocations by a dislocation source. Once present, dislocations can move along slip planes and directions in the bulk of the grains until a barrier such as a grain boundary is encountered. Dislocation motion is also possible along the grain boundary itself which will be discussed later in section 6.5.1.

Dislocations are important in many areas including magnetic, microwave and optical applications as well as mechanical properties [16]. Unfortunately, the crystal structure of oxides, in particular garnets, makes the study of dislocations in oxides difficult. The study of dislocations at grain boundaries is made more difficult by the unknown structure of the boundary. This makes the quantitative study of dislocations at a bi-crystal boundary beyond the scope of this study. On the other hand, more qualitative observations of dislocations, i.e., without knowing the Burger's vector, can still provide useful information.

The presence of dislocations in a material reduces the amount of stresses needed to result in plastic deformation. To result in plastic deformation, motion of the dislocation such as glide or climb must occur. Glide of dislocations involves the movement of the dislocation in the plane containing both its line and Burger's vector. Climb of a dislocation occurs when the dislocation moves out of the gliding surface in a direction perpendicular to its Burger's vector [17]. This latter mechanism is highly dependent on the diffusive properties of the material for movement of an atom (or atoms) is necessary to move the dislocation from one glide plane to another.

Figure 2-5 shows the dislocation glide-climb diffusion aided mechanism activated in ceramics at higher temperatures. Dislocation glide-climb is described as the movement of a dislocation which involves glide of a dislocation (produced by a source S) encountering an obstacle. The obstacle hinders the movement of the dislocation and the dislocation moves to another plane by climb. The climb process results in the movement of the dislocation to another glide plane where it continues to glide [13].

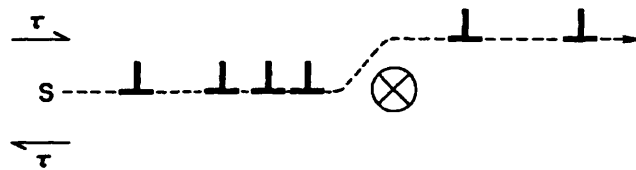


**Figure 2-5 Dislocation glide-climb deformation mechanism, which occurs at higher temperatures. The dislocations, under a shear stress, are generated by a source (S) and will glide along a plane, stop at a barrier, climb to a plane in which glide is not inhibited and will continue to glide [13]. The continuing movement of dislocation can include a climb mechanism as shown in this figure.**



The slower deformation mechanism (glide or climb) determines the creep rate of the material. According to Weertman [13, 18] the controlling step is climb because the diffusion of vacancies to the core of the dislocation takes more time and energy than the glide of dislocations. Other possible controlling mechanisms include edge dislocation climb (Nabarro 1967), glide of screw dislocation with climb of edge jogs (Barret and Nix 1965) and hampered glide controlled creep due to solute atmospheres (Weertman 1957)[18,19,20].

The most probable dislocations grown from melt for YAG are shown in Table 2-1. Table 2-1 was constructed by employing the theory that dislocations, which have the lowest line energy, are produced during melt processing. The calculations assumed that the crystals are grown in the [111] direction. The dislocations grown from the melt are of screw, edge and mixed character. The predicted dislocations produced from the melt were calculated by using a dislocation line energy ( $W$ ) [16].

$$W = \frac{K}{\cos \alpha} = \text{Minimum} \quad (2-1)$$

where the line energy per unit length grown ( $W$ ) is calculated from the angle  $\alpha$  (angle between the growth direction normal and the dislocation line direction) and the energy factor ( $K$ ).

Prediction of slip systems was patterned by Roberts using the highest atomically close packed planes and directions [16]. The calculations for Table 2-2 were made by Roberts using planar densities.

**Table 2-1 Most probable dislocations grown from melt in the [111] direction for YAG [16].**

Burger'ss vector	Growth direction	Probable character
$1/2[111]$	[111]	Screw
$1/2[111]$	[111]	Mixed
[001]	[111]	Mixed
[110]	[111]	Mixed and Screw

**Table 2-2 Calculated slip systems for YAG using most densely packed planes and directions [16].**

<i>Slip Plane</i>	<i>Burger'ss Vector</i>
(211)	$1/2[\bar{1}11][011]$
(110)	$1/2[\bar{1}\bar{1}\bar{1}][001][1\bar{1}0]$
(321)	$1/2[\bar{1}11]$
(100)	$[010][011]$
(411)	$[01\bar{1}]$
(332)	$[\bar{1}10]$
(431)	$1/2[\bar{1}11]$

### 2.5. Critical Resolved Shear Stress

The slip systems (plane and direction) activated during plastic deformation have a tendency to be on the planes of highest atomic density and in the direction of highest linear atomic density. As the energy needed to move a dislocation is added to the system by the system temperature and by applied stresses, one or more slip systems are activated and the movement of dislocations results in plastic deformation. To activate these slip systems, the critical resolved shear stress (CRSS) on any particular grain must be met on that specific system. Figure 2-6 shows a single crystal system which has the slip direction at  $\psi$  degrees to the applied stress axis [6]. The slip plane of the system is  $\phi$  degrees from the stress axis. The equation, which describes the critical resolved shear stress, is expressed in equation 2-2 [6].

$$\tau_{crit} = \frac{F}{A} \cos \phi \cos \psi \quad (2-2)$$

The quantity  $(\cos \phi \cos \psi)$  is known as the Schmidt factor and is used to determine which systems may be activated during the application of stress. Using the orientation of the bi-crystal, the different preferred slip systems can be located and a prediction of the activation of these systems can be made [6].

The most closed packed planes and directions for YAG (slip systems) are shown in Table 2-2. Figure 2-7 shows a sketch of the bi-crystal with respect to the boundary orientation and the possible orientation of the (310) planes. However, for the orientation

shown in this sketch, an analysis of Schmidt factors reveals that the predicted slip systems are the  $\{110\}$  and the  $\{211\}$  planes. Table 2-3 shows the calculated slip system for the bi-crystal orientation using Schmidt factors. The calculated slip systems for the orientation of the YAG bi-crystal are not only included in Robert's [16] predicted YAG slip systems, but they are the two primary systems predicted.

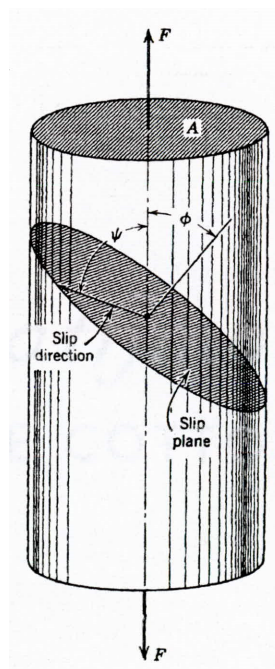


**Figure 2-6 A single crystal showing applied forces, slip direction, slip plane and angles between these planes, directions and axis of applied stresses [6]. The slip systems in a single grain can be predicted when orientation of the grain is known.**

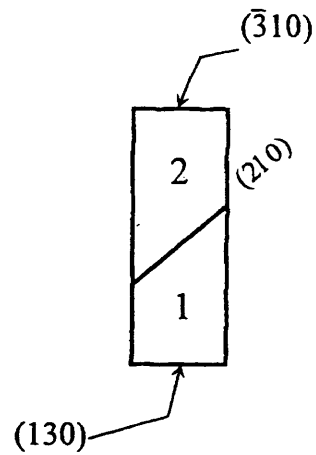


**Figure 2-7 Sketch of YAG bi-crystal with possible (310) planes. The (310) planes are 45 degrees from the boundary and are the planes perpendicular to the compression axis.**

**Table 2-3 Calculated slip planes for the orientation in Figure 2-10.**

<i>Crystal</i>	<i>Schmidt Factor (cos φ sin φ)</i>
<b>Crystal 1</b>	
{110}	0.49
{211}	0.47
<b>Crystal 2</b>	
{110}	0.49
{211}	0.47

### 2.5.1. Slip

The variables that determine the amount of sliding at a grain boundary include boundary tilt angle, temperature, applied stresses and the intrinsic bonding character of the grain boundary [2]. In this section, the general details of the mechanisms of slip are discussed.

Plastic deformation of ceramics (by grain boundary sliding) can occur by atomic slip and dislocation movement. Slip can occur in different directions depending on the activated system. The sketch shown in Figure 2-8 predicts the yield of a perfect material. Here, a perfect array of atoms must move relative to each other to result in plastic deformation. In this sketch the calculated shear strain is ~60% [2].

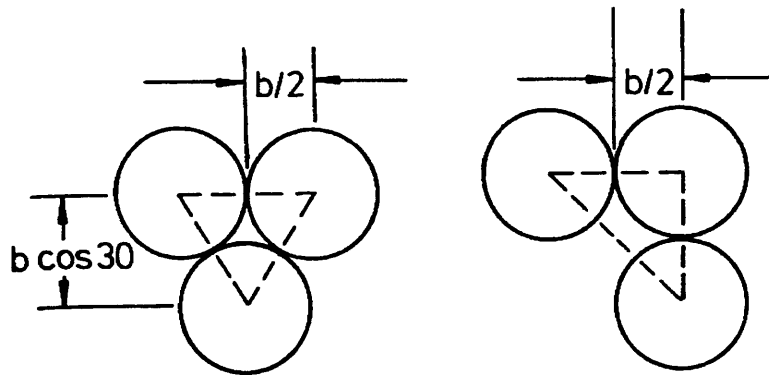


**Figure 2-8 A model describing the amount of strain needed to plastically deform a lattice for a perfect crystal. Strain needed to plastically deform material is ~60% [2]. Ceramic materials do not tend to plastically deform to this extent.**

In actuality, yield strains for ceramics are commonly  $<1\%$ , although this value depends on temperature, purity of material and other factors. This demands the analysis of another atomic array. In this example, dislocations are used to explain that low strains are needed to induce plastic deformation. Figure 2-9 shows that the atoms in the extra half plane must only move a small distance to the right or left to result in plastic deformation [13]. Thus, grain boundary sliding is possible through small atomic strain.

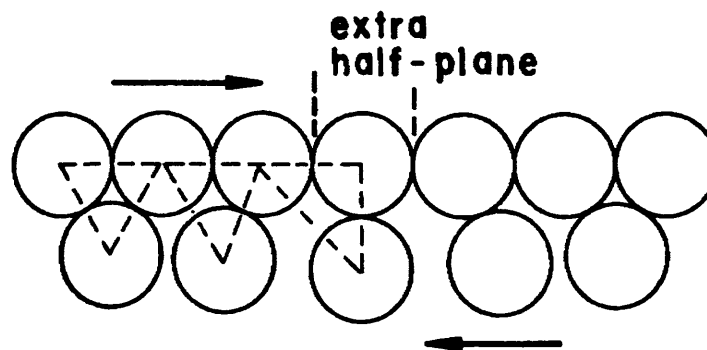


**Figure 2-9 A model describing the amount of strain needed to plastically deform a non-perfect crystal. Strain needed to plastically deform is  $\sim 1\%$  [13]. Ceramic materials, in general, only deform to a few percent strain.**

### 2.5.2. *Rachinger Sliding*

Sliding of grain boundaries without diffusion accommodation is termed Rachinger sliding [15, 21]. Rachinger sliding is used to describe sliding accommodated by intragranular slip in adjacent grains, localized slip at boundaries, formation of triple points or the opening of wedge cracks as shown in Figure 2-10. Rachinger sliding results

in relative movement of grain boundaries without grain shape change. Rachinger measured grain width and length changes of deformed grains in polycrystal aluminum. The strains found for these measured grains were compared to the total strain of the tested sample. From these measurements, Rachinger determined that the strain in the material was attributed to the relative movement of the grains for the low strain rate tests [21].

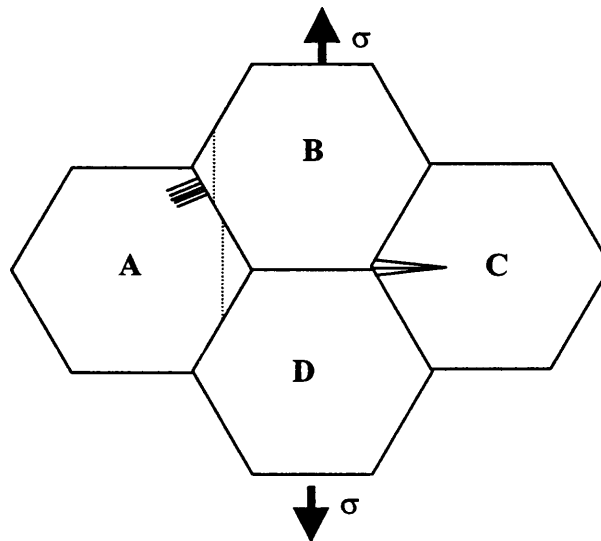


**Figure 2-10 A sketch of grains exhibiting Rachinger sliding under an applied stress ( $\sigma$ ). Rachinger sliding can involve microcracks, slip in the grains and localized boundary Rachinger sliding involves non-grain shape deformation [redrawn from 15]. Rachinger sliding does not involve extensive plastic deformation in the grains.**



## 2.6. Boundary Shape Changes

Slip of the grain boundary is an integral part of creep of polycrystals. Without grain boundary sliding, diffusional creep cannot exist [14, 22]. Raj and Ashby proposed that grain boundary sliding is dependent on the shape of the boundary and the shape of the boundary controls the grain boundary sliding rate. The following observations were made on grain boundary sliding: first, different boundaries, cut from the same bi-crystal were found to have different sliding rates under identical testing conditions. Second, boundary shape changes resulting from the migration of the boundary result in changes in sliding rate. Also, the activation energy of grain boundary sliding is similar to that of the activation energy of bulk diffusion for that material suggesting that grain boundary sliding is a process governed by a diffusion-aided mechanism [22].

The sliding mechanisms resulting in grain boundary sliding considered are elastic, diffusive accommodation and dislocation movement. The boundary shape is described by a sine function and is shown in Figure 2-11.

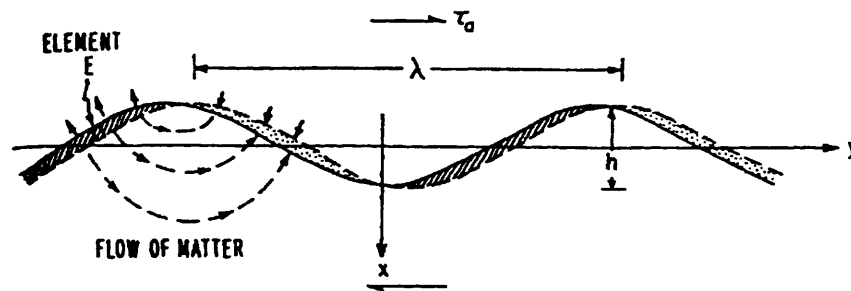


**Figure 2-11 Grain boundary shape of a grain boundary exhibiting diffusive grain boundary sliding [22]. The diffusive grain shape change results in grain boundary sliding rate changes.**

The increase in the frequency ( $\lambda$ ) and amplitude (h) of the boundary shape is the result of applied stress and can result in large grain boundary shape changes. Raj et al. concluded that sliding was found to be dependent on the boundary shape and not on any intrinsic grain boundary property [22].

### **2.7. Migration**

In some metals, sliding of grain boundaries has been found to occur simultaneously with the migration of the boundary [22, 23, 24]. The migration of boundaries is of particular interest in ceramics due to the effect that the activity of grain boundaries contributes to the processing of these materials. In particular, the sintering of ceramics relies heavily on the migration of boundaries and high mobility at grain boundaries results in higher densification of a component [25]. Migration is also important because it can result in grain boundary shape changes, which, as discussed earlier, can alter the sliding rate of the grain boundary.

There are certain characteristics of grain boundary migration (diffusion induced) which can give insight to the behavior of ceramics for a pure YAG bi-crystal. The migration of the boundary can be driven by chemical inhomogeneity and/or grain boundary structure. For the present study, only the latter explanation will be entertained.

Grain boundary migration is a thermally activated, interface-controlled process and the mobility of the boundary is "spasmodic" and not continuous [26, 25]. Thus, it is

possible to observe the migration of boundaries by physically locating the "jumps" associated with the migration of the boundary.

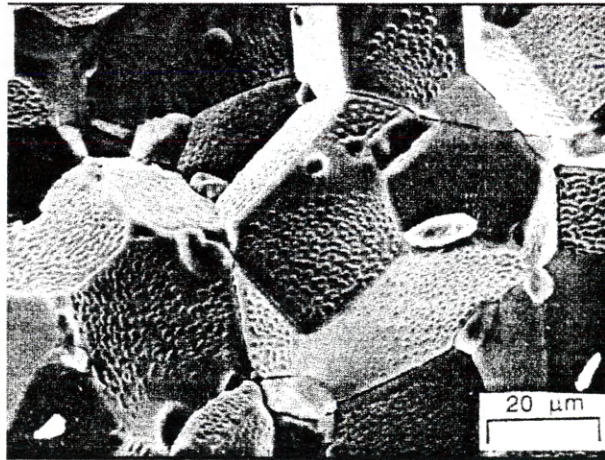
New grains may be nucleated from the migration process and the process may be driven by curvature of the grain boundaries. Migration proceeds by a diffusion mechanism that is faster than observed lattice diffusion rates because diffusion at grain boundaries generally occurs at higher rates due to the availability of dislocations, vacancies and other point defects which aid in the diffusion process [26, 27, 28, 29]. Migration of coincident site lattice boundaries is not sensitive to impurities while random grain boundaries are dependent on the presence of impurities [25].

The mechanisms by which grain boundaries migrate are associated with other grain boundary deformation mechanisms such as sliding. Both migration and sliding of the grain boundary require the presence of defects (grain boundary character) which result in the movement of atoms (or vacancies) about the grain boundary. In the case of grain boundary sliding, the movement of atoms or dislocations occurs parallel to the grain boundary. For migration, the movement of atoms occurs perpendicular to the grain boundary [25].

From the grain boundary shape theory developed by Raj and Ashby, migration of the boundary can also alter the deformation of the boundary. Grain shape changes causes irregular sliding rates in large bi-crystals [22]. Thus, it is important to identify boundary shape after deformation in order to understand the sliding behavior of a bi-crystal.

### 2.8. Cavitation in Ceramics

In the later stages of creep, one possible mechanism of fracture at grain boundaries is cavitation. Blanchard and Chan studied the creep deformation behavior of alumina and found that the controlling mechanism of deformation is nucleation-controlled cavitation [30]. The cavities found on the specimen after fracture were present in three different locations at the grain boundaries as shown in Figure 2-12. The cavities shown are for an alumina sample tested under constant loading conditions (140MPa) at 1600C which resulted in failure after 150 minutes of testing time. A schematic of the different positions of the cavities formed is shown in Figure 2-13.



↑  $\sigma_c$

**Figure 2-12 Cavitation show mostly at two-grain facets on crept samples of Lucalox alumina tested at 1600°C [30]. The voids found at the grain boundaries is a result of diffusive deformation mechanisms resulting from the applied stresses during testing.**

Cavities form in one of three locations: 1) at a triple grain junction, 2) at a two-grain junction and finally 3) at a four-grain junction. The nucleation and coalescence of cavities along two-grain junctions controlled the failure of the alumina. The direction of cavity in cavitation failure mode is governed by the orientation of the grain facet and its energy [30]. The shapes of the voids were consistently similar depending on the grain junction. For three and four grain junctions, ellipsoidal cavities formed. For two-grain junctions, spherical cavities were formed. However, ellipsoidal cavities were also observed on two-grain junctions.

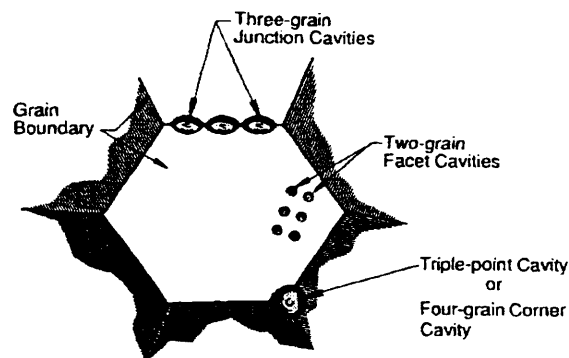


**Figure 2-13 Possible cavitation nucleation sites resulting from creep deformation for materials in general [30]. The void shape changes found on the different facets may be a result of the diffusion mechanism responsible for void formation.**

## 2.9. Combined Processes

Different grain boundary deformation mechanisms can operate at once resulting in grain shape changes and grain boundary sliding and accommodation. Figure 2-14

shows the combination of diffusional creep and grain boundary sliding mechanisms. Under tensile stresses the grains will elongate in the tensile direction due to tensile and compressive forces driving the flux of atoms. The grain boundaries experience shear stresses that slide the grain boundaries against each other. The resultant deformation is an elongated (in the tensile axis) specimen induced by the combination of grain boundary sliding and diffusion of atoms in the material [13].

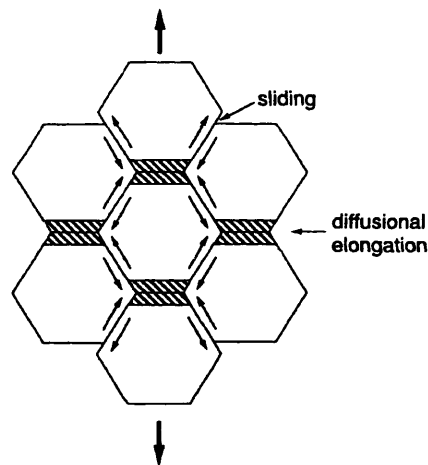


**Figure 2-14** A sketch of combined deformation mechanisms resulting from an applied stress. Diffusional elongation resulting in elongated grains is shown, as is the sliding of grains relative to each other resulting from dislocation motion, diffusion or a combination of the two [13].

### ***2.10. Single Crystal vs. Polycrystal Deformation***

For YAG single crystals, dislocation mechanisms control the deformation process as opposed to the control by diffusional mechanisms for polycrystalline YAG [3,4,31].

Figures 2-15 and 2-16 express the frequency of calculated stress exponents for mechanisms of deformation for a large range of ceramic materials for both polycrystals and single crystals compiled from various studies [13]. Stress exponents (n) express the relationship between stress and the strain rate. Equation 2-3 is a general expression for the steady state creep of ceramics [9].

$$\dot{\epsilon} = \frac{B D G b}{k T} \left(\frac{b}{d}\right)^r \left(\frac{\sigma}{G}\right)^n \quad (2-3)$$

In this equation, B is a constant, D is the diffusion coefficient of the material, G is the shear modulus, b is the Burger's vector, r is the grain size exponent, and n is the stress exponent. The different mechanisms of creep result in different stress exponents. For example, "Nabarro-Herring" creep has a stress exponent of 2 and "Coble" creep exhibits a stress exponent of 3 [9].

The difference in mechanism between single crystalline and polycrystalline materials can be explained by the following reasons: First, resistance to dislocation glide for a specific material, be it polycrystal or single crystal, does not always significantly reduce as temperatures in the system increases. Secondly, ceramics tend to have fine grain sizes and for these microstructures, diffusion mechanisms are enhanced due to the availability of free volume for atomic movement at the grain boundaries [13].

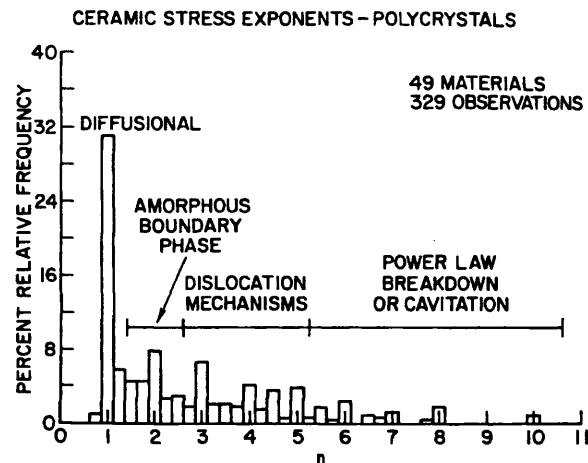


**Figure 2-15** A frequency chart of deformation mechanisms (where  $n$  is the stress exponent for the mechanism of deformation) for polycrystal materials. There is a higher frequency of  $n=1$  governing the deformation of polycrystals [13]. Thus, diffusion ( $n=1$ ) is responsible for the deformation of polycrystals.

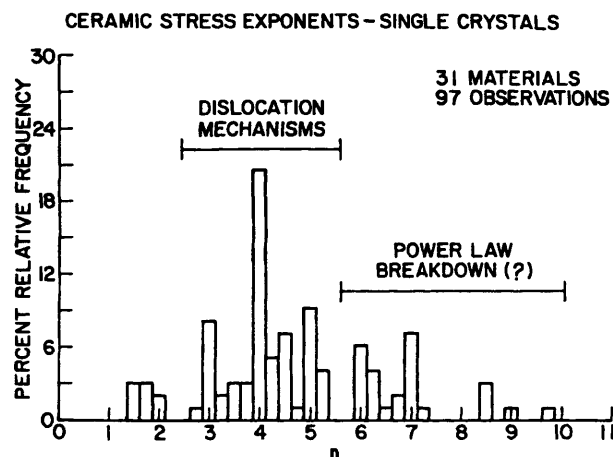


**Figure 2-16** A frequency chart of deformation mechanisms (where  $n$  is the stress exponent) for single crystal materials. For single crystals, there is a higher frequency of  $n=4$ . Thus, dislocations are responsible for deformation of single crystals [13].



### 2.10.1. Mullin's Theory

W.W. Mullins presented the theory to explain grain boundary grooving with respect to the diffusional properties of materials [32]. Figure 2-17 shows the geometry of a typical groove showing the dimensions and important parameters used in the present section.

Grain boundary grooving experiments were performed and analyzed to calculate diffusion coefficients of YAG at different temperatures and implementing Mullins grain boundary grooving theory. Mullins postulated that grooves form where grain boundaries intersect the surface of a solid and generally takes place at high temperatures ( $>0.5 T_{\text{melting}}$ ).

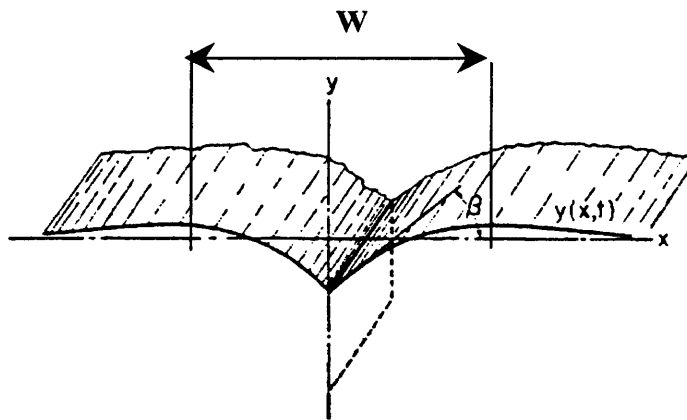


**Figure 2-17 A sketch of a grain boundary groove showing the equilibrium angle ( $\beta$ ), the two-dimensional axis used to describe the geometry of the growing boundary groove and the peak to peak distance ( $W$ ) [modified from 32]. The groove geometry is used to calculate the diffusion coefficient of materials.**

The details of the YAG bi-crystalline groove study must correspond to the assumptions made in the grain boundary groove theory postulated by Mullins. The main assumptions for use in Mullin's theory and the corresponding applicability to the YAG bi-crystal study are the following: 1) The interface properties (such as surface energy) do not depend on the orientation of the two connected crystals. Since the two bonded surface of the crystals are (210) planes, the surface energy of the two bonded surfaces are equal and the corresponding solid/vapor surface energy of each crystal is also equal [33]. The orientation of the crystals at the boundary does not effect the diffusive properties of the interface. 2) Only evaporation/condensation, volume diffusion and surface diffusion are possible mechanisms of groove growth. For a surface diffusion controlled groove growth, the effective contribution to the growth of the groove by volume diffusion or evaporation-condensation is negligible due to order of magnitude differences in surface diffusion, volume diffusion and evaporation-condensation diffusion coefficients. In a system where volume diffusion controls (and limits) the groove growth rate, the same is true for the effect of evaporation-condensation groove growth. For the YAG bi crystal, volume diffusion was assumed to be governing the groove growth after groove growth experiments were performed on the boundary and will be discussed in detail in section 5-8 of this thesis. 3)  $\gamma_b \gg \gamma_s/2 = \sin\beta \cong \tan\beta$ . Where  $\gamma_b$  and  $\gamma_s$  are the grain boundary energy and surface energy respectively and  $\beta$  is shown in Figure 2-17. 4) The grooving process is described macroscopically. Atomic imperfections and atomic grooving effects are ignored, thus focusing on the macroscopic groove change can be employed for grooves

that are more than a few atomic levels deep. The roughness of the YAG bi-crystal was in the order of 0.05 microns and the height of the grooves were in the order of 0.5 microns thus eliminating any atomic or surface roughness effects on the grain boundary grooves.

5) Grain boundary diffusion is negligible and the boundary maintains an equilibrium angle. The experiments on the YAG bi-crystal were performed after a period of time in which the groove maintained a constant equilibrium angle.

The groove develops such that the resultant tension is zero at the grain boundary/surface intersection line. At the intersection line, grooves form due to an equilibrium angle ( $\beta$ ) establishment. The condition for this equilibrium angle is given by:

$$2\gamma_s \sin\beta = \gamma_b \quad (2-4)$$

where  $\gamma_s$  is the surface energy and  $\gamma_b$  is the grain boundary energy. The ridges are sharp when initially formed and the diffusional process (which is driven by curvature differences at the surface) flattens these ridges. The flattening of the groove disturbs the equilibrium angle that in turn results in deepening of the groove. The growth and the geometry of the groove results in measurable information of the groove system.

Based on preliminary calculations done for this thesis, which will be discussed in the Results section, volume diffusion is assumed to control the grooving process for the YAG bi-crystal. The solution to grain boundary grooving kinetics is described using  $x$ ,  $y$  and  $t$  (time) as experimental variables. For a detailed analysis of the solution for volume diffusion grooving see Mullins. Mullins developed the groove width kinetic ( $W$ ) and rate

constant ( $A'$ ) equations shown in 2-5 and 2-6 and are used in the present study to calculate the volume diffusion coefficient for YAG.

$$W=(A't)^{1/3} \quad (2-5)$$

$$A' = 125n\Omega^2 D\gamma\sqrt{kT} \quad (2-6)$$

For equations 2-5 and 2-6,  $W$  is the peak-to-peak distance of the boundary groove as shown in Figure 2-17,  $A'$  is the rate constant,  $t$  is time,  $n$  is the number of atoms per unit volume,  $\Omega$  is the atomic volume and  $kT$  is the thermal energy [34].

### 2.10.2. Diffusion Coefficient

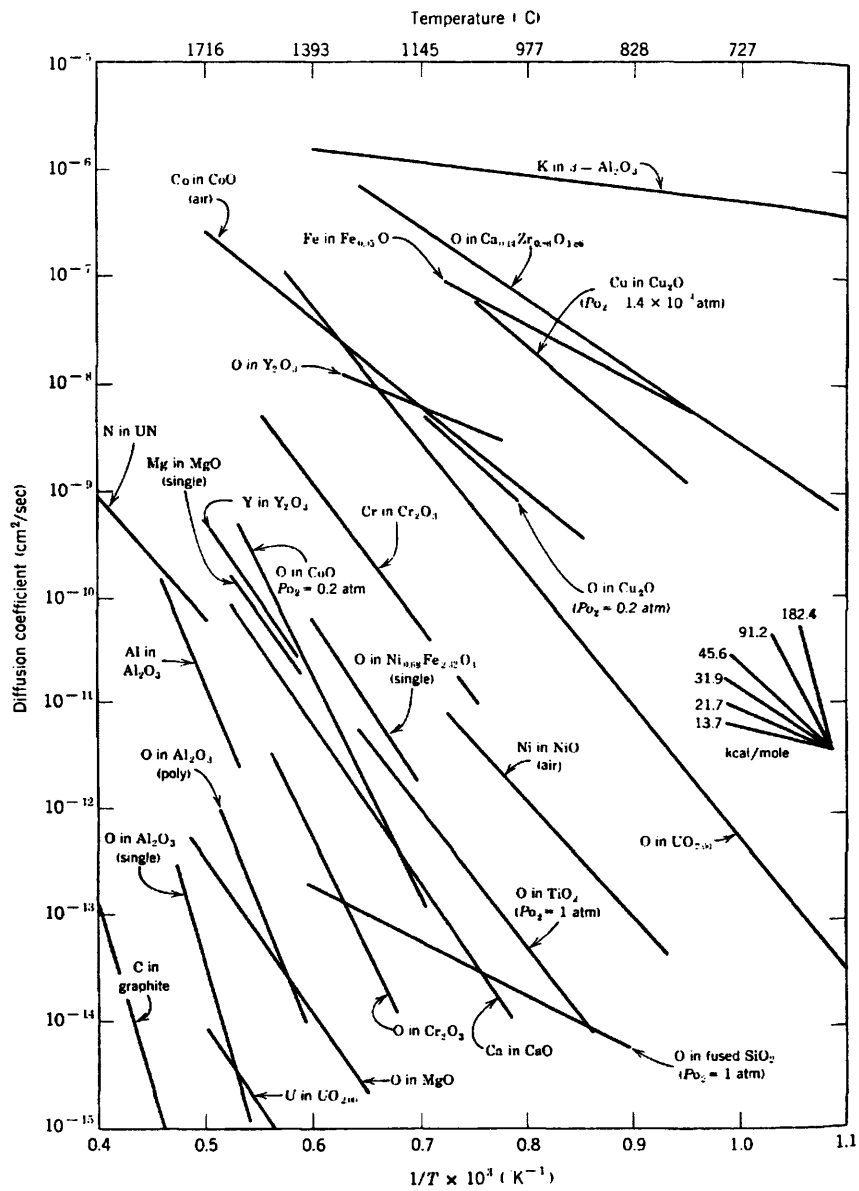
The diffusion coefficient of a material helps in determining other important material characteristics by relating the diffusion coefficient to the energy of a diffusion mechanism. The diffusion coefficient calculation for a single diffusion mechanism at different temperatures gives the activation energy of the process through the following Arrhenius equation:

$$D_v = D_o \exp(-Q_v/RT) \quad (2-7)$$

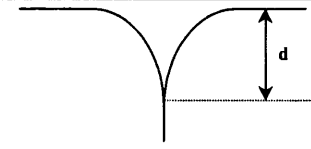
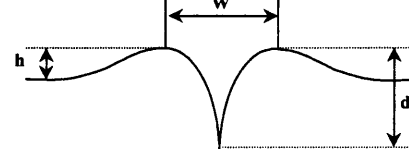
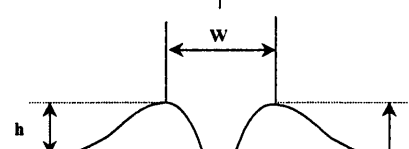
Where  $D_v$  is the volume diffusion coefficient,  $D_o$  is the Diffusion coefficient constant, and  $Q_v$  is the activation energy. Figure 2-18 shows the relationship between temperature ( $T$ ) and the diffusion coefficient ( $D$ ) for different ceramic materials [6]. Here, the slope of the straight line is the activation energy and is expressed in the inset.

### *2.10.3. Diffusion Mechanisms*

The geometry of the groove also gives clues as to the mechanisms controlling the diffusion process. The ratio between the height of the ridge ( $h$ ) and the depth of the ridge ( $d$ ) has been used to determine if the diffusion mechanism is evaporation/condensation, surface or volume diffusion [34]. Figure 2-19 gives general sketches of the three resulting geometries. The evaporation/condensation diffusion process results in ridges that do not extend above the original surface height. Volume and surface diffusion produce ridges that are higher than the original surface height but surface diffusion produces ridges that extend higher and a groove, which is not as deep as for volume diffusion.



**Figure 2-18 Graph of diffusion coefficients plotted against the inverse of temperature for different ceramic materials. The slope inset gives values of the activation energies for these materials [6].**

Transport Mechanism	Time Dependence of Dimension	Relative Ridge Height	Shape of Profile
Evaporation-Condensation	$t^{1/2}$	0.00	
Volume Diffusion	$t^{1/3}$	0.149	
Surface Diffusion	$t^{1/4}$	0.208	

**Figure 2-19 Sketches showing the three grain boundary groove growth diffusion mechanism (evaporation/condensation, surface and volume diffusion). Exponents for each mechanism and ratios of groove height and depth are also given [redrawn from 34].**

### 3. LITERATURE SURVEY

A few studies have been performed on the structural integrity of YAG [4, 3, 31, 35]. These tests include various creep tests on single crystalline YAG and one creep test focused on polycrystalline YAG. All studies were performed at high temperatures (>1500°C) and at comparable strains and stresses. A summary of these studies is given in Table 3-1. Information regarding specimen orientation (for single crystalline studies), testing temperature, strain rate, stresses (for constant stress studies) and activation of creep is given.

**Table 3-1 Summary of deformation experiments performed on YAG single crystalline and polycrystalline. P=polycrystalline, S=single crystalline**

Type of Material (P or S)	Type of Test	Stress Values (sec <sup>-1</sup> or MPa)	Testing Temp. (°C)	Crystal Orientation (direction parallel to compression axis)	Creep Activation Energy (kJ/mol)
S	Constant Strain Rate	10 <sup>-5</sup> to 10 <sup>-7</sup>	1635 & 1785	[135]	596 - low strain rate 1085 - high strain rate
S	Constant Stress	50 to 280MPa	1650 to 1850	[100], [110], [111]	~680 - low strain rates >2000 - high strain rate
S	Constant Strain Rate	10 <sup>-7</sup> to 10 <sup>-6</sup>	1580 to 1690	[100]	~720
P	Constant Strain Rate	10 <sup>-5</sup> to 10 <sup>-3</sup>	1400 to 1610	N/A	~584



### 3.1. General Mechanical Behavior

Single crystalline YAG was found to plastically deform when compressed under low strain rates ( $\sim 5 \times 10^{-6}$ /sec) [4,35]. Under these conditions, a steady state regime was achieved after a "strain hardening" regime as shown for Blumenthal's work in Figure 3-1. A peak stress above 350MPa was achieved at 1785°C. A similar steady state regime is also found for Karato's work [35] for lower temperatures and a higher strain rate as shown in a stress-strain curve (Figure 3-2).

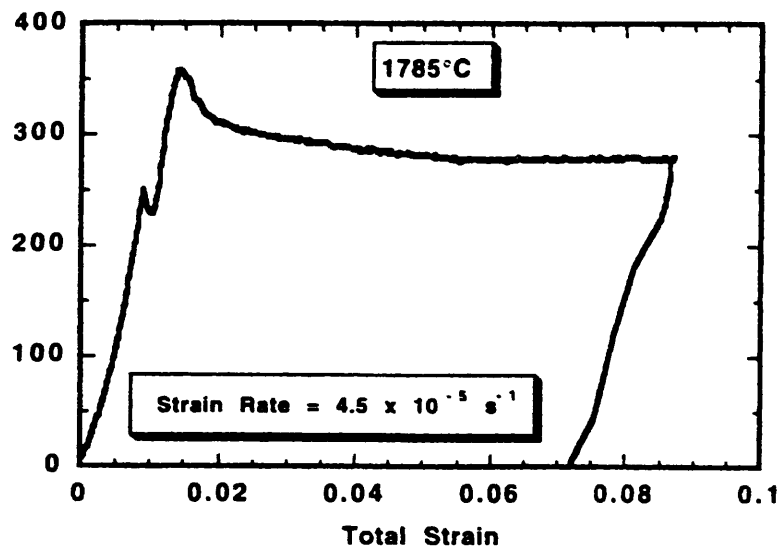


**Figure 3-1** Stress-strain deformation curve for single crystal [135] YAG compressed at 1785°C at a constant strain rate of  $4.5 \times 10^{-5}$ /sec. A peak stress is achieved at  $\sim 1\%$  sample strain followed by a steady state deformation region. The sample deformed  $\sim 7\%$  [4].

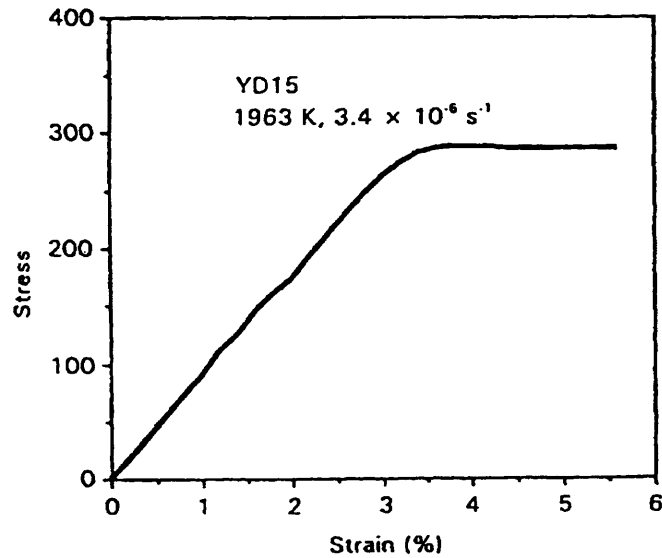


**Figure 3-2 Stress-strain for single crystal [100] oriented YAG at 1700°C at a constant strain rate of  $3.4 \times 10^{-6}$ /sec. A steady state region is achieved after a few percent sample strain [35].**

For the constant stress experiments [3], decreasing strain rates were generally observed although an increase in strain rate was observed for the high temperature/high stress conditions. A strain/time curve is shown for a single crystal oriented to the [111] direction in Figure 3-3. For these studies, the temperature and/or stress was changed during testing. For these tests, strain up to 10% was achieved on the specimens.

The polycrystalline experiments [31] resulted in higher flow stresses at higher strain rates. The fracture stress at low temperatures (1200°C) was found to be ~600MPa whereas the fracture strength at 1600°C for a single crystal oriented in the [100] direction was ~350MPa [35].

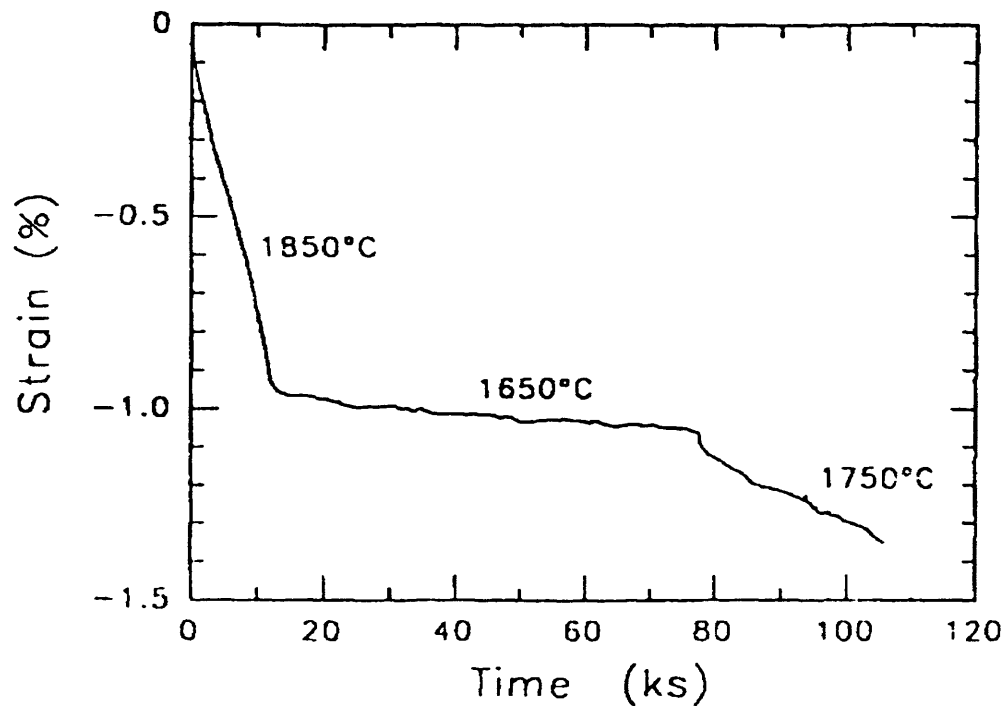


**Figure 3-3 Stress-time curve obtained from a constant strain compression experiment on [111] oriented single crystal YAG at different temperatures. Temperature was changed during the experiment [3].**

### **3.2. Deformation mechanisms**

Dislocation movement was found to be the deformation mechanism for single crystalline YAG [4]. The deformation creep of YAG was explained by the creep rate equation:

$$\dot{\epsilon} = A\sigma^n \exp(E^*/RT) \quad (3-1)$$

A constant ( $A$ ), stress ( $\sigma$ ), activation energy ( $E^*$ ), and thermal energy ( $RT$ ) are used to determine the creep rate. The stress exponent,  $n$ , depends on the mechanism responsible for deformation. A stress exponent of 1 describes a diffusion mechanism deforming the material. For Blumenthal's work, the stress exponents at 1635°C were found to be between 3 and 8. These large exponents suggest that a dislocation-aided mechanism is governing the deformation of YAG oriented in the [135] direction. Corman's study observed stress exponents between 2 and 10 for tests performed at 1635°C also suggesting dislocation motion in the single crystals. Figure 3-4 shows these results.

Polycrystalline YAG exhibits a stress exponent of 1.1 and is compared to Corman's study in Figure 3-5. A stress exponent of  $\sim 1$  indicates that the mechanism of deformation is diffusion. The different exponents suggest that different mechanisms control the deformation behavior between single crystalline and polycrystalline YAG.

### ***3.3. Activation Energy***

The activation energies calculated from the creep data for all the studies (including the polycrystalline study) agree within  $\sim 15\%$ . Figure 3-6 depicts the strain rate vs. temperature for polycrystalline and single crystalline YAG. The agreement in activation energy values indicates that although different mechanisms are controlling the deformation behavior of polycrystalline and single crystalline YAG, both mechanisms are diffusion aided. Since it has been postulated that dislocation are responsible for creep

in single crystalline YAG [4], the mechanism of motion for the dislocations must be a diffusion aided mechanism such as dislocation climb.

The activation energy values of the diffusion creep of YAG for all studies are between 550 and 720 kJ/mol [3,4,31,35], whereas the activation energy of the volume diffusion of oxygen in YAG is 300-320 kJ/mol [1]. The disagreement in activation energies suggests that oxygen is not limiting the diffusional creep of YAG but one of the cations is responsible for the creep rate of YAG. However, the diffusion data for the cations in YAG does not exist.

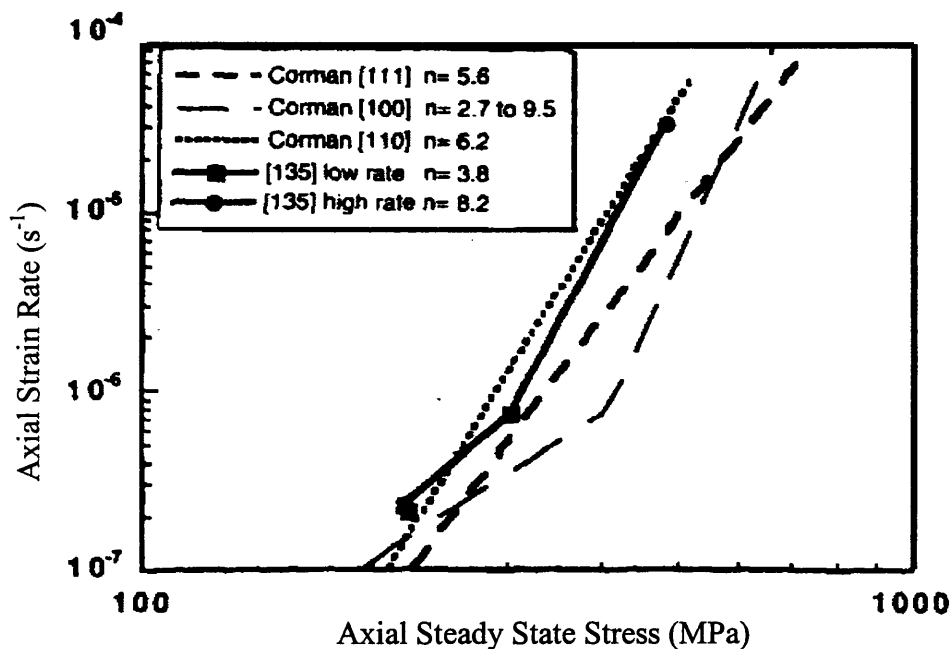
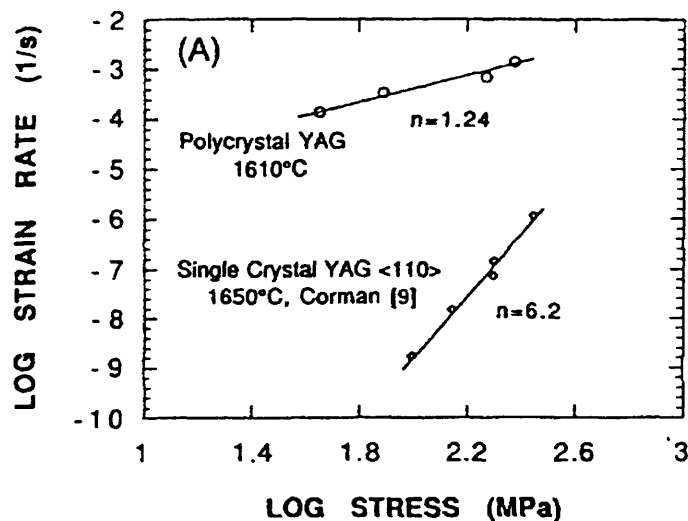
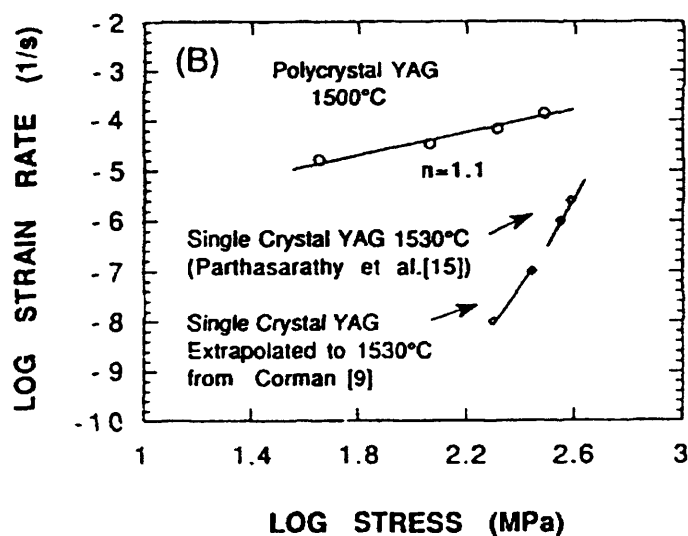


**Figure 3-4 Axial strain rate vs. axial steady state stress relationship for single crystal YAG. Comparison of different crystal orientations performed at 1635°C. Corman's experiments were performed in helium. The [135] orientations were performed in air [modified from 4].**



a)



b)

Figure 3-5 Stress exponents depicted on strain rate vs. stress relationships for two temperature regions: *a*)~1635°C and *b*)~1515°C. At 1635°C polycrystalline and single crystalline YAG have different exponents. Similarly, the exponent increases from polycrystalline YAG to single crystalline YAG at 1530°C. The increase in stress exponents between single crystalline and polycrystalline YAG suggests different controlling deformation mechanisms [31].

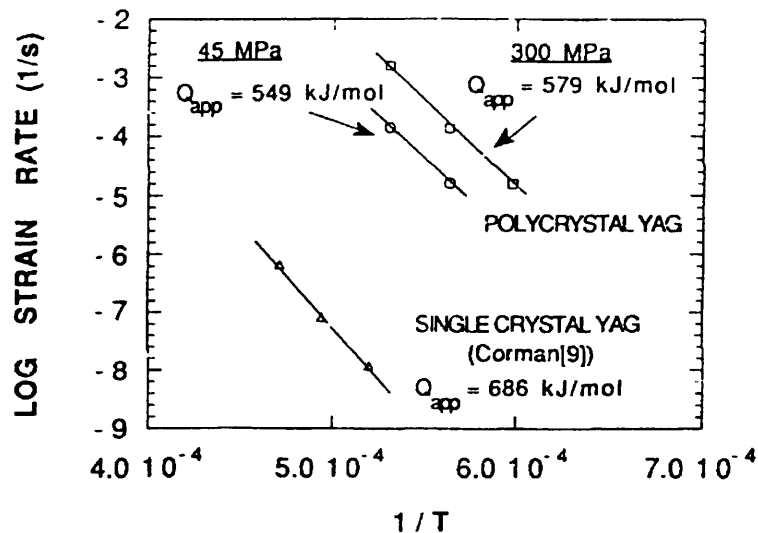


**Figure 3-6 Activation energies for polycrystalline and single crystalline YAG. Comparison of two studies (Corman and Parthasathary). Similar activation energies suggest that diffusion is controlling the creep of these materials [31].**

#### **3.4. Low Vs. High Strain Rates**

Corman and Blumenthal found very large stress exponents for high strain rates which suggest that a different deformation mechanism is activated at these conditions. The activation energies for high strain rates in both studies are above 2000 kJ/mol [3,4]. The stress exponents are also higher ( $>6$ ) suggesting that the dislocation mechanism is different between low strain rate and high strain rate conditions. The mechanism may be changing from a dislocation climb to a dislocation glide mechanism.

### 3.5. *Summary*

Creep deformation of YAG differs for polycrystalline and single crystalline materials. For both materials, the mechanism of deformation is aided by diffusion and is limited by one of the cations except for high strain rate conditions in single crystals. For single crystals dislocation climb is a possible creep deformation mechanism for low strain rate conditions and dislocation glide may be governing the deformation for high strain rate testing conditions.



## 4. EXPERIMENTAL DETAILS

### 4.1. *Production of Bi-Crystals*

The production of a structurally understood boundary was required to allow the boundary structure analysis of the boundary. A boundary was created by choosing a low angle  $\Sigma 5(210)/[001]$  symmetric tilt grain boundary which, for the garnet structure, was made by the rotation of two similar single crystals about the (210) plane. YAG single crystals were grown by Union Carbide Inc. (San Diego, CA) in the [111] orientation. They were sent to Valpey-Fischer (Hopkinton, MA) where they were sectioned and polished to within  $0.1^\circ$  of the desired bonding plane. The prepared surfaces were sputter cleaned with a 1keV  $\text{Xe}^+$  beam energy at a grazing angle of  $15^\circ$  at Lawrence Livermore National Laboratory in a ultra-high vacuum bonding machine (vacuum level  $< 7 \times 10^{-8}$  torr) shown in Figure 4-1,. The crystals were then aligned by reflecting a laser on a flat reference plane located on the crystals. The crystals were subsequently bonded at  $1550^\circ\text{C}$  for six hours under a stress of 5MPa. Each of these steps was performed in a different chamber to reduce contamination. The crystals were moved about in the chambers shown in Figure 4-1 with a robotics-controlled arm [36]. Due to the high costs of the bonding process, a limited number of crystals were made.

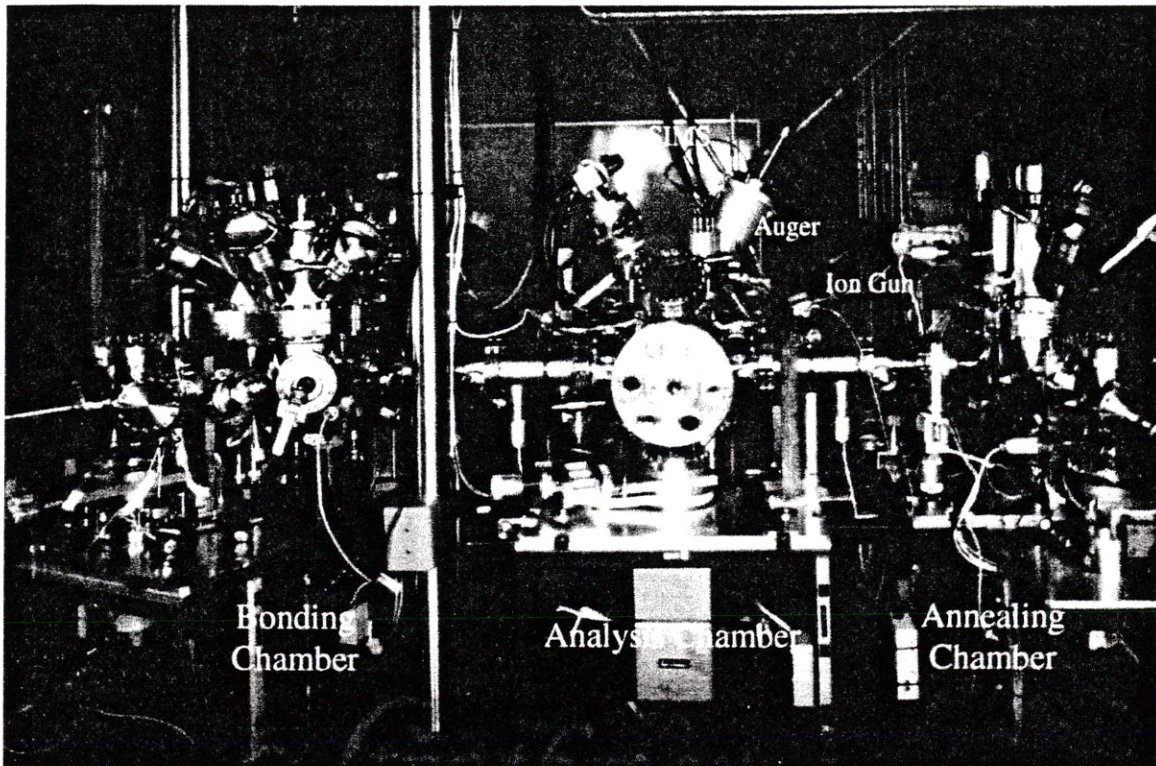


**Figure 4-1 Materials bonding chamber specifying chambers and guns. The production of the YAG bi-crystals required high vacuum to reduce boundary contamination and also required a tool to precisely orient the bonded planes. This apparatus is located at Lawrence Livermore National Laboratory. [5].**

#### ***4.2. Compression Testing***

The bulk YAG bi-crystals were diamond cut to  $2 \times 2 \times 6 \text{ mm}^3$  ( $0.08 \times 0.08 \times 0.24 \text{ in}^3$ ) by Bomas Machining (Somerville, MA). Figure 4-2 shows the general position of the samples machined from the bulk bi-crystal. The orientation of the boundary with respect to the compression axis is shown in Figure 4-3.

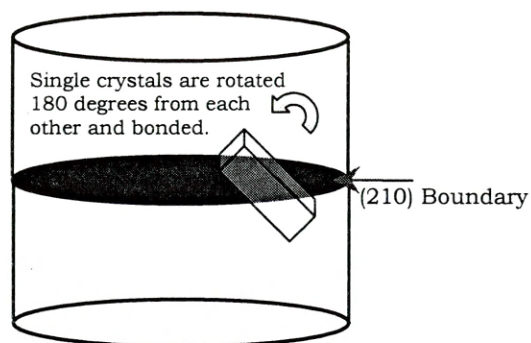


**Figure 4-2 Relative orientation of YAG compression samples with the bulk YAG bi-crystal. The boundary is 45° to the length of the compression axis. All compression samples were sectioned in this same orientation to maximize the stresses on the boundary during compression.**

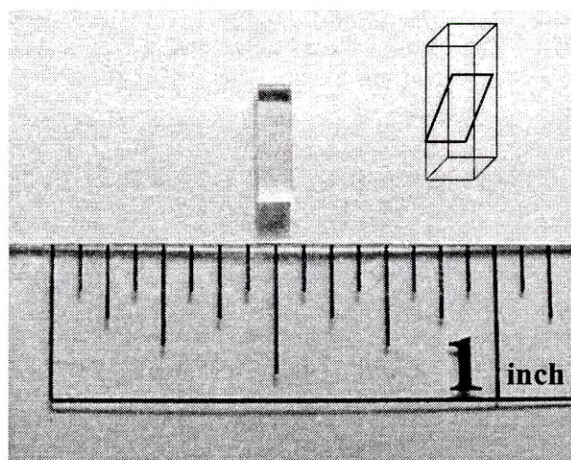


**Figure 4-3 YAG compression sample shown with a sketch of the position of the boundary with respect to the surface of the sample. The sample dimensions were  $\sim 2 \times 2 \times 6 \text{ mm}^3$  or  $0.04 \times 0.04 \times 0.24 \text{ in}^3$ .**

The compression samples were machined randomly about the bulk crystal. Laue x-ray scans performed on the bi-crystals were used to find the exact orientation of the compression samples. The orientation analysis using Laue technique is outlined in the

Appendix. The YAG bi-crystals were tested in compression on an Instron (CM-30) fitted air furnace (CM Furnace, Bloomfield, NJ) with molybdenum di-silicide elements. The furnace has a maximum temperature of 1720°C ( $\pm 10^\circ$ ) and was fitted with yttrium aluminum garnet single crystal rams used for compressing the bi-crystals. Sapphire spacers were used between the YAG compression sample and the YAG single crystal rams to avoid YAG/YAG bonding. Figure 4-4 shows a schematic of the furnace/Instron system used for the compression tests. Initially, 1.25 inch diameter alumina rams were used to compress the YAG bi-crystals, however, these rams exhibited high creep rates at high temperatures and low stresses. The stresses in the bi-crystal YAG samples were not sufficiently high in order to test for structural integrity. The alumina ram system consisted of an 18 inch long top ram and a 12 inch long bottom ram. Sapphire spacers were not necessary since YAG and alumina do not readily bond.

Alignment of the system was accomplished internally with a ball and socket configuration and is designated as #1 in Figure 4-4. The top ram is an alumina ram that has a ball at one end. The alumina ram does not experience temperatures greater than 1100°C. In contact with the alumina ram is a single crystalline YAG ram (12 inch long and 1.25 inch diameter) which extends into the hot zone. A single crystalline YAG ram was also used as the bottom ram and the end rams were locked in by water-cooled aluminum sleeves that are bolted to the Instron frame.

The heating rate of the system is 610°C/hour and heating was conducted with the sample pre-loaded to ~5MPa ( $\pm 1$ MPa). The Instron cycled between 4 and 6 MPa to

allow expansion of the rams and the system during heating and was allowed to equilibrate once it reached maximum temperature. The compression test was initiated and a strain rate of  $5.4 \times 10^{-6}$ /sec was used to calculate the crosshead speed.

With the exception of the high stress tests the compression tests were run until one of the following occurred: 1) The sample fails (load drops significantly or to zero), or 2) A calculated strain of  $\sim 3\%$  was attained. Cooling can occur with or without a low load depending on the test outcome.

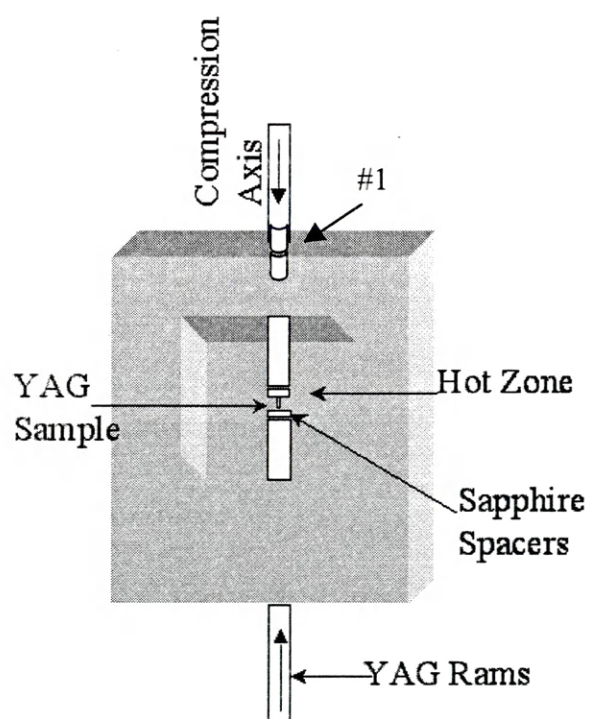


**Figure 4-4 Compression testing apparatus showing the YAG rams used to compress the YAG sample, the self aligning ball and socket (#1) and the sapphire spacers used to avoid bonding of YAG/YAG surfaces in the hot zone.**

Two compression tests were made to establish if diffusion or slip of the boundary were responsible for the deformation of the bi-crystal. The first test consisted of a low constant stress test ( $\sigma_{\text{const}} \sim 60\text{MPa}$ ) performed at  $1700^\circ\text{C}$  designed to minimize the occurrence of slip. The stress was applied slowly with ( $3.4 \times 10^{-5}\text{in/min}$ ) and when  $\sigma_{\text{const}}$  was reached, a stress of  $60 \pm 1\text{MPa}$  was maintained for 2 hours by using the maximum and minimum controllers on the Instron. The second test consisted of a constant crosshead speed and high stress experiment designed to maximize slip. The crosshead speed was increased to more quickly achieve a stress to  $\sim 200\text{MPa}$ . The calculated strain on the sample was found to be  $\sim 5\%$ .

### ***4.3. Grain Boundary Grooving***

A YAG bi-crystal with the grain boundary intersecting the surface at  $90^\circ$  was used for performing the grain boundary grooving experiments. The YAG samples used for the grain boundary grooving experiments were sectioned with an Isomet slow speed saw (sample dimension:  $4 \times 5 \times 6\text{mm}^3$  or  $0.16 \times 0.20 \times 0.24\text{in}^3$ ) and were randomly oriented. Figure 4-5 shows the sample and a sketch of the position of the boundary with respect to the surface of the sample.

The sample was final polished with 0.1micron diamond paper and scanned in the atomic force microscope to insure that a flat surface was present before heat-treating. The temperatures chosen for the grooving study were  $1550^\circ\text{C}$ ,  $1587^\circ\text{C}$ ,  $1623^\circ\text{C}$ ,  $1663^\circ\text{C}$  and  $1700^\circ\text{C}$ . The heating and cooling steps of the heat treatment were recorded and are

shown in Figure 4-6. Eight atomic force microscopy scans were performed along the length of the boundary with a multi-mode atomic force microscopy scanner (Digital Instruments, Santa Barbara, CA). A typical AFM line scan is shown in Figure 4-7.

Each area scan was sectioned ten times at different locations along the boundary to get an average of 80 scans for each temperature. These values were recorded and an average of the peak-to-peak distance of the groove was calculated. The measured peak-to-peak distances were used to calculate diffusion coefficients for each temperature using Mullins equations (equations 2-5 and 2-6).

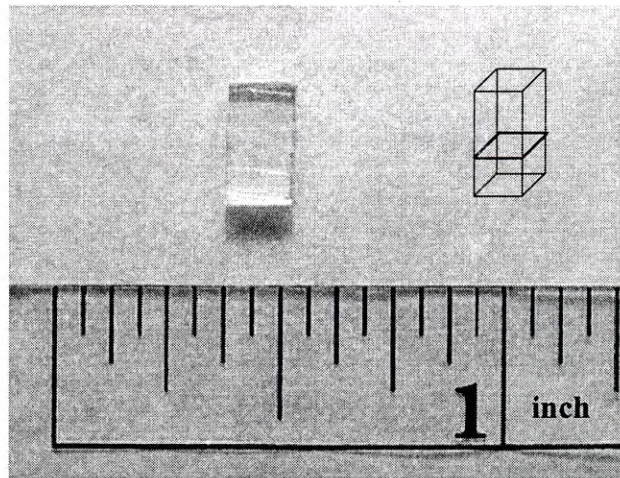


**Figure 4-5 Standard sample used for diffusion groove growth measurements. Sketch shows the positioning of the grain boundary with respect to the surface of the sample. An angle of 90 degrees between the surface and the boundary is needed to correctly measure the geometry of the thermal groove.**

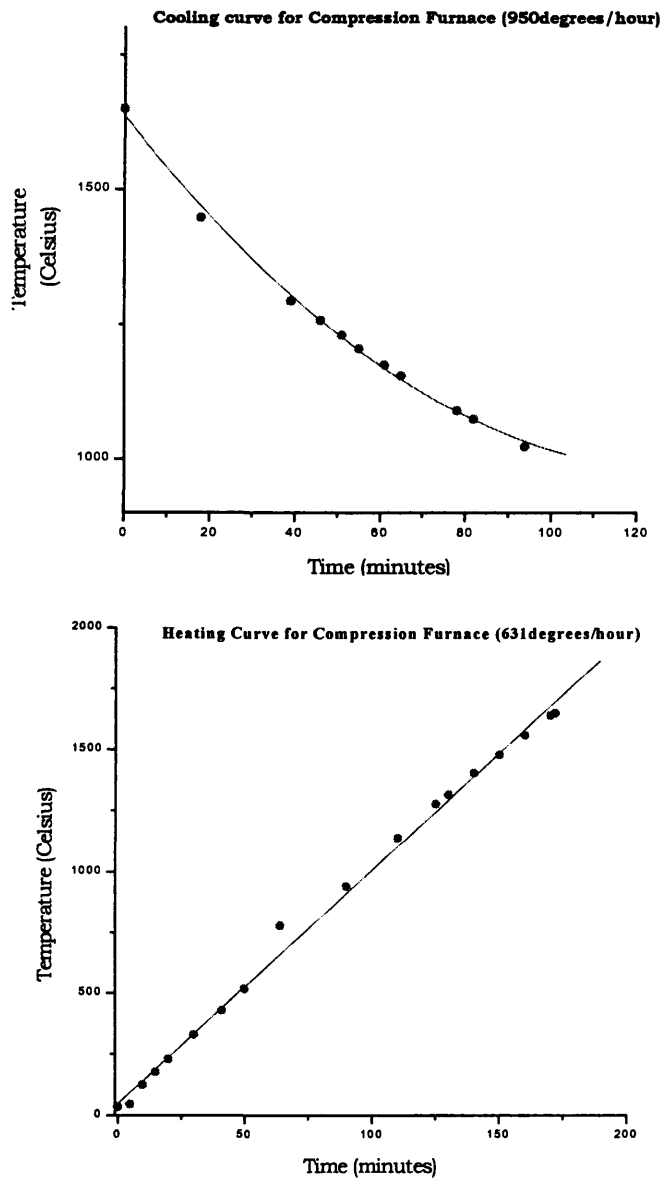


**Figure 4-6 Cooling and heating curves of the furnace used to heat-treat the boundary to obtain grain boundary grooves. The heating and cooling steps were similar (except for the maximum temperature) for all of the experiments performed.**



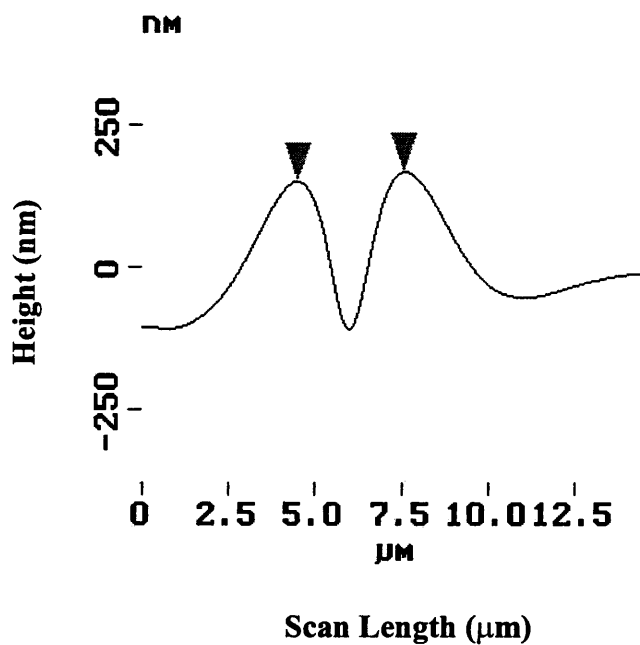


**Figure 4-7 Typical groove geometry of YAG grain boundary after heat-treating. The geometry of the groove varied in height with testing time.**

#### **4.4. Analysis Techniques**

Different techniques were used to analyze all the experimental results. The diffusion tests required only AFM scans as opposed to using a variety of techniques for the compression data. The following is a summary of the different techniques used in the present study.

#### 4.4.1. Profilometry

Two profilometers were used to make surface scans across deformed boundaries to check for any steps present at the boundary/surface intersection created by slip of the boundary. The first profilometer was a Veeco Sloan Dektak 3030 unit (Santa Barbara CA) that uses a mechanical stylus to scan across the surface of samples. The second profilometer was a Veeco Dektak<sup>3</sup> unit that uses an optical system to detect features of different heights at the surface of specimens. Only three compressed bi-crystals were scanned with profilometers. For one compression sample, only two scans were taken of the bi-crystal; one scan was made at one boundary face and the other was made at one edge face. For the last two compression samples, the profilometer scans were performed on all four surfaces where the boundary meets the surface of the sample. Scanning the steps on all four faces revealed if the boundary was sliding or if the crystals were increasing in cross sectional area by a diffusion mechanism. To perform the scans, the instrument was leveled such that the sample surface was perpendicular to the vertical axis. Different scan lengths were used ranging from 100 $\mu\text{m}$  to 1200 $\mu\text{m}$ .

#### 4.4.2. Atomic Force Microscopy

Atomic force microscopy was used to observe changes in groove geometry of the boundary after heat treatment and compression. The scans were performed at 2MHz frequency in "contact" mode and were made with a cantilever stylus. The scan size ranged from (20 $\mu\text{m}$ )<sup>2</sup> to (150 $\mu\text{m}$ )<sup>2</sup> and a typical scan is shown in Figure 4-8. The scan

consists of the surface area scanned showing the height of the surface features using a color code shown to the right of the figure.

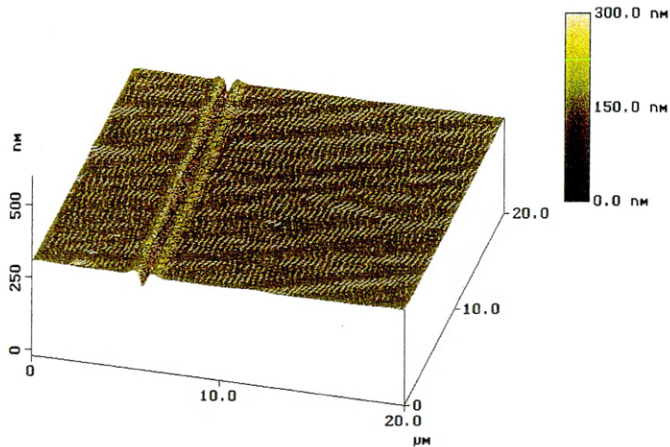


**Figure 4-8 A typical 20 micron scan obtained from the atomic force microscopy. The scan shown is 20x20 microns in area and the color spectrum bar identifies the height level of each point in the scan. This scan is further sectioned to measure the groove for calculating the diffusion coefficient of YAG.**

Atomic force microscopy in the “contact” mode was used to perform the groove “peak-to-peak” measurement. The “contact” mode consists of the interaction between the tip and the surface to be scanned. Other effects (such as an electric field present from the material) do not affect the scans produced using the “contact” mode. A change in the tip size did not significantly change the measurement of the peak to peak distances. Similarly, a change in the frequency of the scans did not alter the measurement of peak-to-peak distances.

#### 4.4.3. *Electron Microscopy*

Scanning electron microscopy was used to observe deformation induced features. Scanning electron microscopy was used to find any signs of boundary migration. The samples were not coated so as to preserve any surface features that may have contained information about the deformation mechanism of the bi-crystal.

Transmission electron microscopy was used to detect the presence of dislocations in both the bulk of the material and at the boundary. TEM analysis of the boundary involved the preparation of the boundary such that the boundary is perpendicular to the TEM specimen. The compression sample was first sectioned to make at least three wafers as shown in Figure 4-9. The dotted lines in Figure 4-9a show the cuts made on the compression sample to make three TEM specimens. Each wafer was subsequently sectioned such that the boundary was located diagonally across the square TEM specimen as shown in Figure 4-9b. The thickness of the wafers was approximately 250 to 600 microns. The TEM specimens were ground with a Gatan (Pleasanton, CA) hand grinder until they were between 80 and 110 microns thick. Silicon carbide grinding paper of 600 grit was used for the grinding step. Each TEM specimen was polished using diamond film paper starting with 30-micron diamond film to 0.1  $\mu\text{m}$  diamond film. Final specimen thickness was between 40  $\mu\text{m}$  and 70  $\mu\text{m}$ . The specimen was mounted on a 3mm-diameter (2.3mm I.D.) copper ring using super glue. The specimen was ion milled on a Gatan Model 691 Precision Ion Polishing system (Pleasanton, CA) which uses a

focused ion beam to thin the TEM specimen. A completed TEM specimen is sketched in Figure 4-10. The ion guns on the ion mill were positioned at  $8^\circ$  and  $6^\circ$  for the bottom and top beams respectively as shown in the figure. The ion beams move across the TEM sample while the ion mill rotates the sample. Ion milling of the YAG bi-crystal required approximately 2 to 4 hours for a  $40\mu\text{m}$  thick sample.

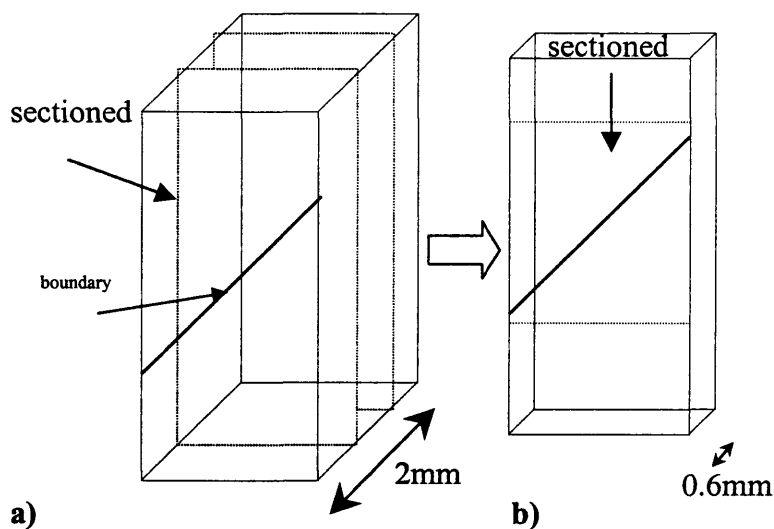


**Figure 4-9 Sketch of YAG bi-crystal compression sample showing sectioned TEM specimens. a) Each compression sample was sectioned into three wafers. b) Each wafer was sectioned to make a thin rectangular TEM specimen.**

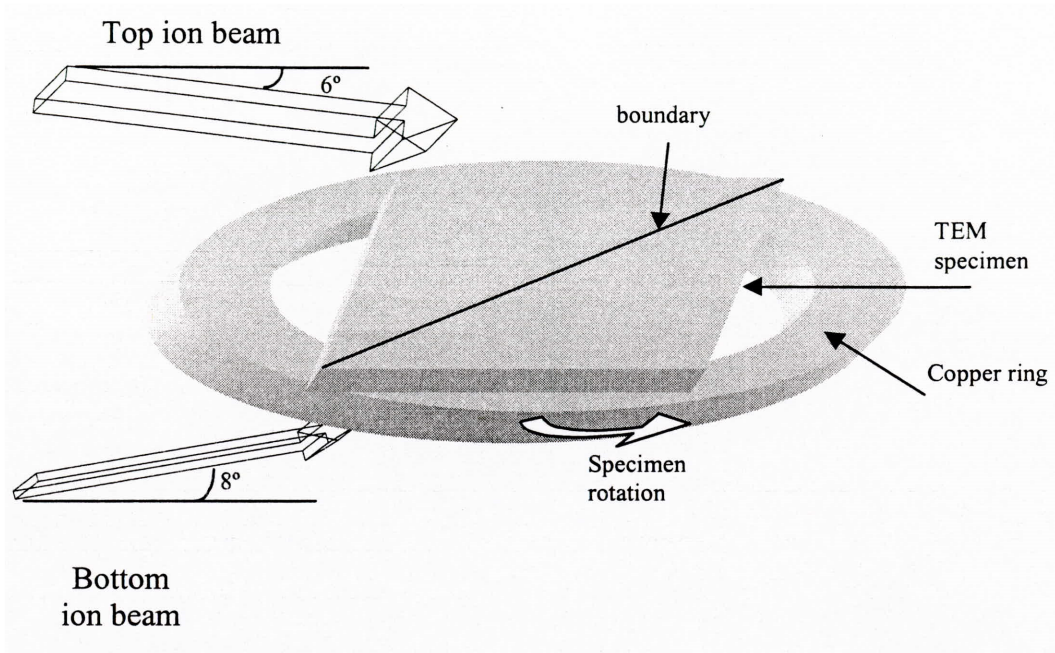


**Figure 4-10 Final TEM specimen mounted on copper ring. Arrows designate the ion beams. Specimen was milled with high energy beams while rotating. The result was a YAG TEM quality specimen.**

## 5. RESULTS

After testing and analyzing of the experiments, the following compilation of results has been made. The geometry of the compression samples has a designation as to which face is used for certain observations throughout the present section. Figure 5-1 shows the compression sample and the designation of either the edge or the boundary face.

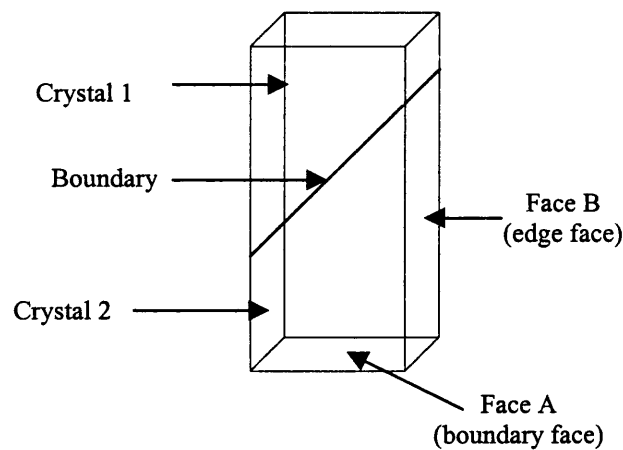


**Figure 5-1 Sketch of boundary and edge faces designated on the compression sample. Face A designates the face which has the boundary intersecting it at 90 degrees. Face B designates the face which has the boundary intersecting it at 45 degrees.**

### ***5.1. Dislocation Structure of As-Received Boundary***

The HREM micrographs of the undeformed boundary were taken by Goeff Campbell at Lawrence Livermore National Laboratory. HREM on the undeformed boundary is important to show the state of the boundaries before deformation. The micrographs show a very low density of dislocations which were most likely a result of the crystal misfit due to the error in polishing and orientation of the bonding surfaces. High resolution imaging (HREM) shows a flat, clean boundary (Figure 5-2). The figure shows three different images. The inset to the far left is a sketch of the atomic model used to identify the predicted structure of the boundary. The simulated image shows the predicted TEM image obtained from the model. The third image is the actual experimental image formed.

### ***5.2. Sample Orientation***

The bi-crystalline compression samples were machined without control of the orientation of the bi-crystal. However, all the compression samples were cut at the same orientation and the boundary structure was consistent for all of the specimens. The planes of interest are identified on Figure 5-3 since these planes are either the major slip plane or slip direction in YAG as identified on the sketch. The major slip system for YAG is shown in this figure as a plane and direction (arrow) of preferred. To identify the exact orientation of the samples, Laue was performed on each sample. The results of the Laue patterns show that all the compression samples were cut in the same exact



orientation, thus all of the compression samples have the same orientation. The boundary face was found to be  $\sim 11$  degrees ( $\pm 1^\circ$ ) from the (111) plane. A partially indexed Laue pattern which is representative of all the compression samples is shown in Figure 5-4. For a more detailed explanation of the plane identification of Laue Patterns see the Appendix.

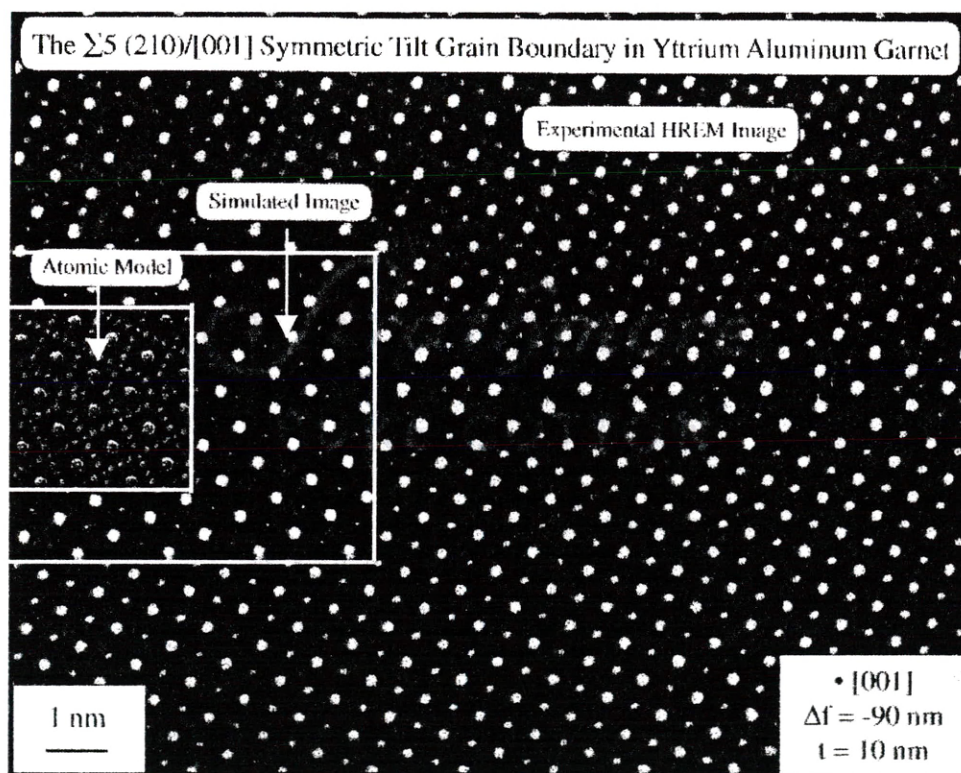


**Figure 5-2 High-resolution image of  $\Sigma 5$  YAG boundary after processing and before deformation [5]. Experimental image of the YAG boundary with an inset showing a simulated boundary structure found using an atomic model. The experimental and predicted images are similar.**

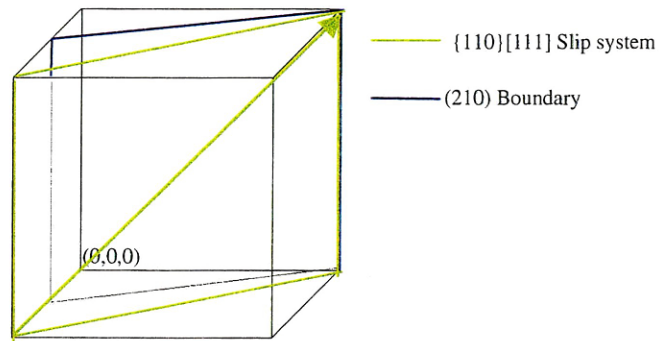


**Figure 5-3** YAG unit cell showing the relative orientations of the (210) boundary and the calculated slip system using Schmidt factors. The slip systems will change with a change in the bi-crystal orientation.

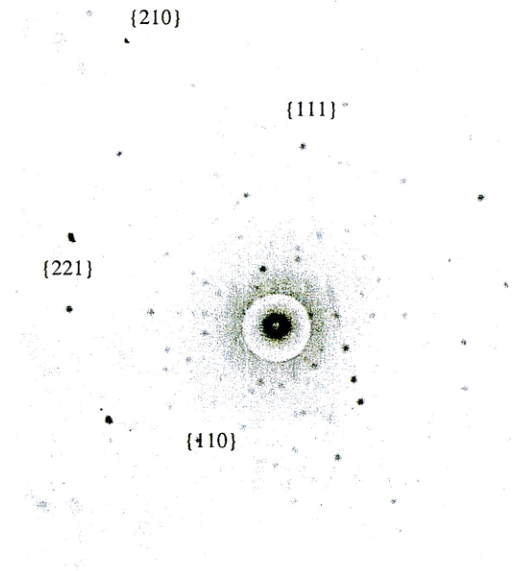


**Figure 5-4** Laue pattern of YAG bi-crystal. Only one crystal was exposed to the x-rays. Major zones are identified on the image. Face B of the bi-crystals are 11 degrees from the {111} planes.

### 5.3. *Compression Testing*

All compression tests were combined into one graph to make direct comparison of each mechanical behavior curve. Figure 5-5 shows all the bi-crystalline compression experiments performed with the exception of the constant stress experiment (sample MP7). Note that sample name and testing temperature identify each curve. The tests performed at 1600°C have higher slopes than the tests performed at 1700°C. Steady state deformation was not observed for any of the tests performed. Table 5-1 identifies each test with the temperature used, strain rate and other important testing information. A compliance curve was performed at 1700°C to check for the rigidity of the apparatus and is shown in Figure 5-6. The compliance curve has a higher slope (at lower stresses) than the testing curves (at higher stresses) and shows that the system is more rigid than the YAG bi-crystal setup. The compliance curve is only used to determine if the system is less rigid than the sample/system deformation experiments.

Each bi-crystal resulted in a different deformation curve. The slopes of those curves are different and there are points in Figure 5-5 for each curve which may represent accommodations or sliding events occurring in the samples or the deformation setup. Some of these events are shown as stars (\*) in the figure. MP6 has a slope change (at ~100 minutes) that was deliberately obtained by increasing the crosshead speed to obtain higher stresses in a shorter amount of time. The short curves in Figure 5-5 are a result of fracture of the specimen and/or sapphire spacers.

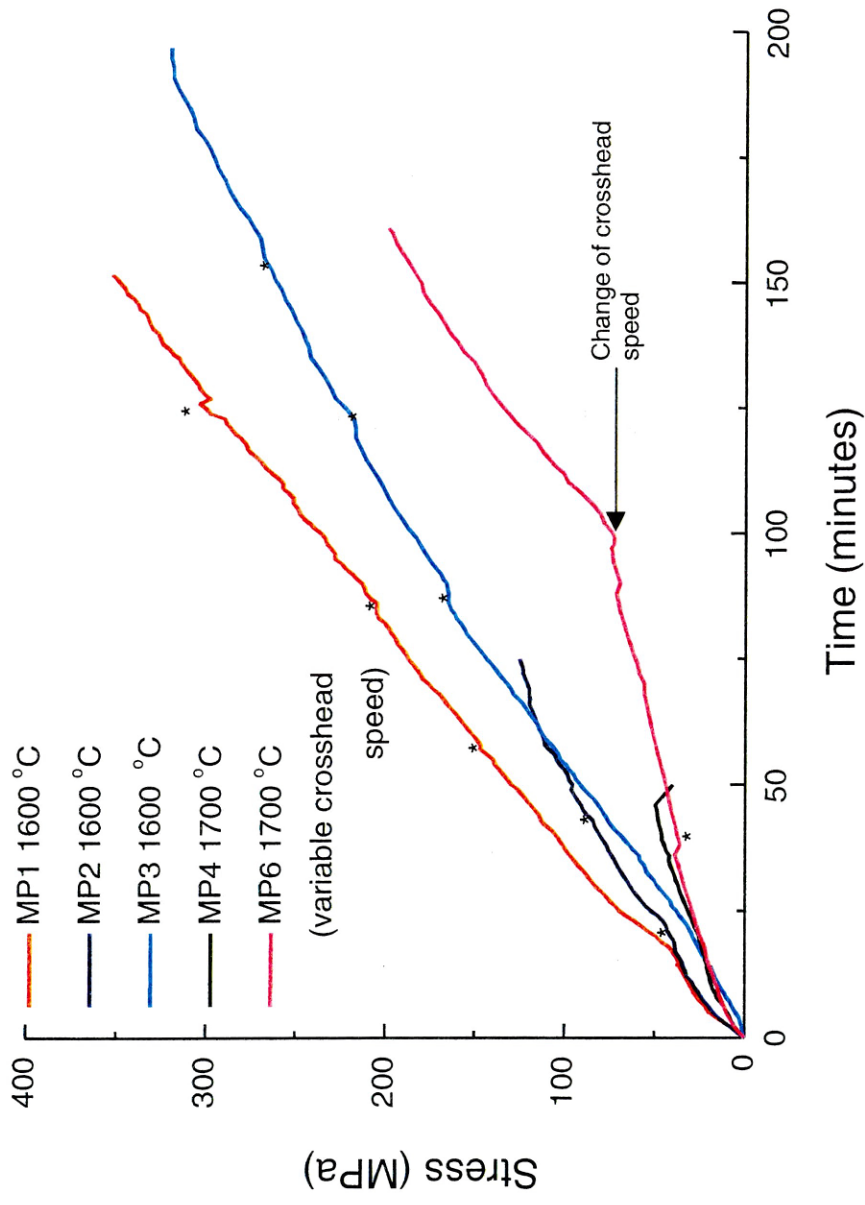
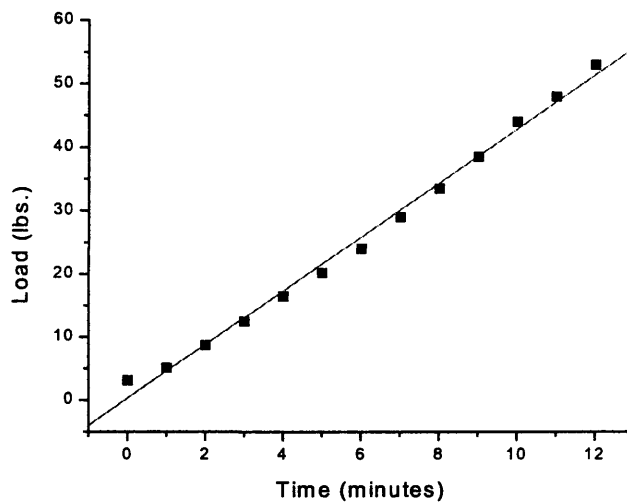


Figure 5-5 Stress-time curves for all compression experiments for the YAG bi-crystalline material. A steady state regime was never achieved and similar curves resulted from the compression tests.



**Figure 5-6 Compliance curve of single crystal ram compression apparatus at 1700°C at a crosshead speed of  $5.2 \times 10^{-5}$  in/min.**

**Table 5-1 Experimental details of the compression experiments performed on the YAG bi-crystals.**

Sample	Temperature (°C)	Cross-head Speed (in/min)	Maximum Stress (MPa)	Boundary State (after deformation)
MP1	1600	$5.2 \times 10^{-5}$	350	Partial fracture
MP2	1600	$5.2 \times 10^{-5}$	120	Intact
MP3	1600	$5.2 \times 10^{-5}$	320	fractured
MP4	1700	$5.2 \times 10^{-5}$	50	Intact
MP6	1700	varied	200	Intact
MP7	1650	$5.2 \times 10^{-5}$	60	Intact

#### 5.4. *Fracture at Grain Boundary*

Two of the compression experiments resulted in the fracture of the compression sample mainly due to misalignment of the specimen. Fortuitously, for MP3, the sample fractured at the boundary and resulted in the exposure of the surface of the boundary. To compare the state of the deformed boundary, an as-received boundary surface was examined. To expose an as-received boundary, an undeformed boundary piece from the edge of a bulk bi-crystal was manually fractured. The undeformed boundary surface was found to be smooth as shown in an optical micrograph (Figure 5-7).

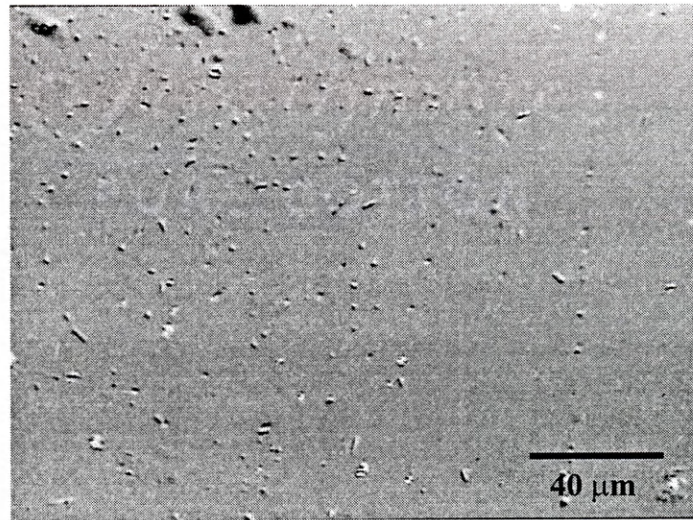


**Figure 5-7 Light micrograph of as-received (non-deformed) boundary surface of YAG. Fracture occurred at room temperature. Small features are observed on this undeformed surface.**

The features shown in this optical micrograph may be cavities that result from diffusion bonding of the bi-crystal. The boundary shape of the fractured MP4 specimen, however, was not smooth and long directional features were observed as shown in Figure 5-8. The significance of these features will be discussed in Section 6-4.

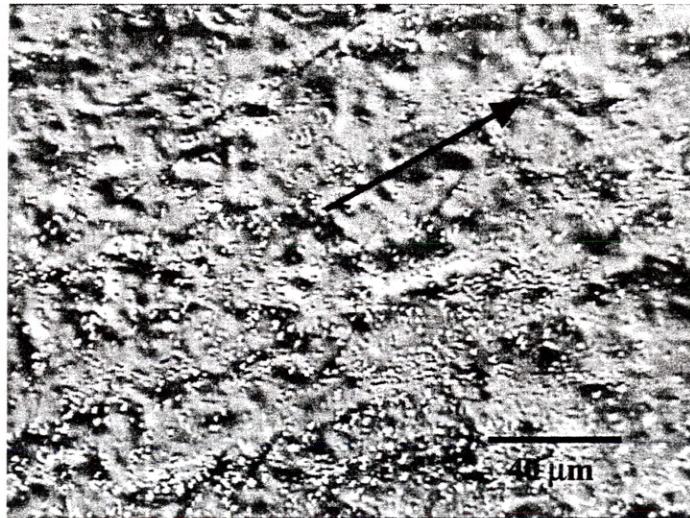


**Figure 5-8 Light micrograph of deformed boundary surface after 1.5% calculated strain. Note the directional features present at the surface of the deformed boundary running parallel to the arrow.**

### **5.5. TEM Analysis of Deformed boundary**

A compression sample (YAG1) deformed to  $\sim 0.7\%$  ( $\pm 4\%$ , 20:1) (uncertainty analysis for single samples [37]) was sectioned and prepared for transmission electron microscopy. This bi-crystal was tested during the preliminary stages of the compression experiments. Testing conditions for this sample were  $1600^{\circ}\text{C}$ ,  $3.4\text{E-}5\text{in/min}$  crosshead

speed and a high steady state stress of 50MPa was achieved. The steady state stress was likely observed due to the creep of alumina rams used for this experiment. The compressed bi-crystal was taken from the second bulk bi-crystal received and thus was not compared with the bi-crystals in Figure 5-5. The microscopy of the boundary resulted in the observation of a dislocation structure. Figures 5-9 to 5-11 show the boundary structure using different tilt angles and imaging conditions.

Figure 5-9 shows the boundary with the sample tilted at 30 degrees. An extensive dislocation structure is observed at the boundary and appears to have a honeycomb geometry. Figures 5-10 and 5-11 show micrographs of the same boundary using different imaging conditions (different specimen tilt angles) that result in different images of the boundary. Figures 10 and 11 also indicate that dislocations may be present at the boundary.

The high stress and low constant stress YAG bi-crystals were also observed in the TEM. Although there is a dislocation structure at the boundary, it does not exhibit a "honeycomb" pattern as in Figure 5-9. Figure 5-12 shows two conventional TEM images of the low stress experiment specimen (MP7). Figure 5-12(a) is an image of the boundary tilted to show the dislocations present and Figure 5-12b shows voids found at the boundary. Figure 5-13 is a TEM image of the high stress experiment specimen (MP6).



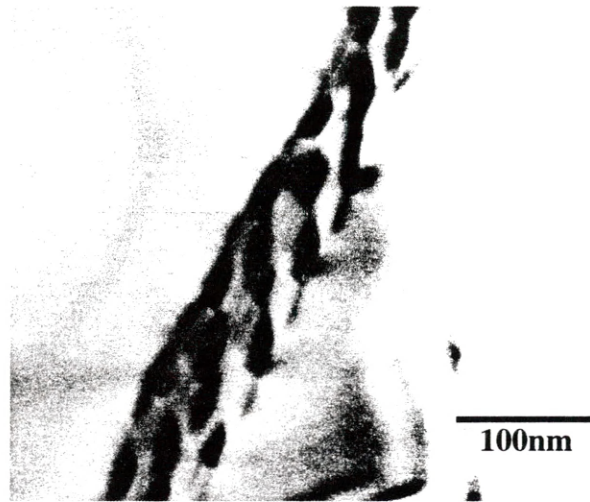


**Figure 5-9** Transmission electron microscopy micrograph of the YAG (YAG1) grain boundary after  $\sim 0.7\%$  ( $\pm 4\%$ ) deformation.  $1600^{\circ}\text{C}$ ,  $3.4 \times 10^{-5}$  in/min crosshead speed, in air. TEM specimen is tilted to  $30^{\circ}$  on the boundary axis. A dislocation structure is present at the boundary.

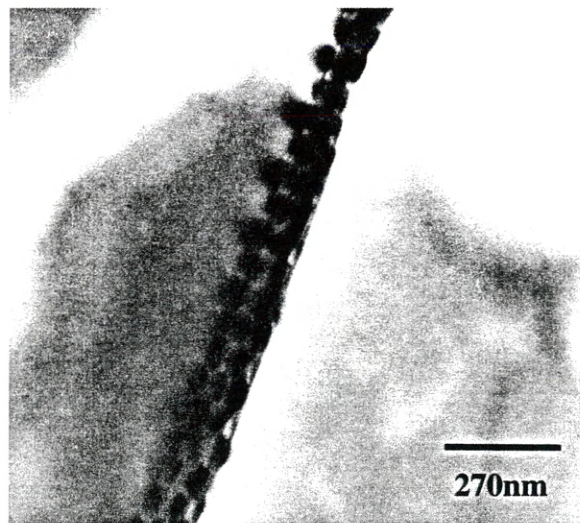


**Figure 5-10** Transmission electron microscopy image of tilted YAG (YAG1) boundary for a specimen deformed to  $\sim 0.7\%$  ( $\pm 7\%$ , 20:1).  $1600^{\circ}\text{C}$ ,  $3.4 \times 10^{-5}$  in/min crosshead speed, in air. Specimen tilted to  $-35^{\circ}$  on the boundary axis. The dislocation structure is observed under different imaging conditions.

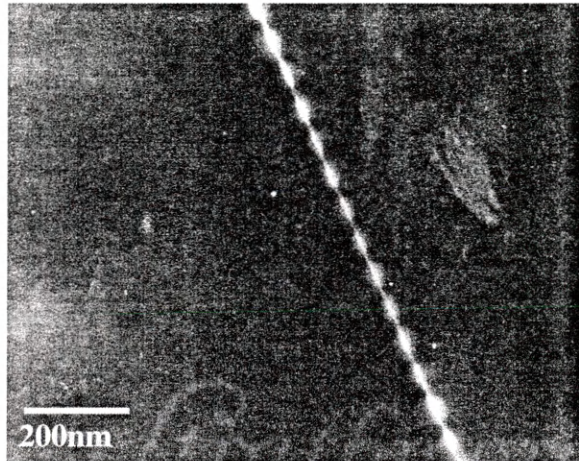
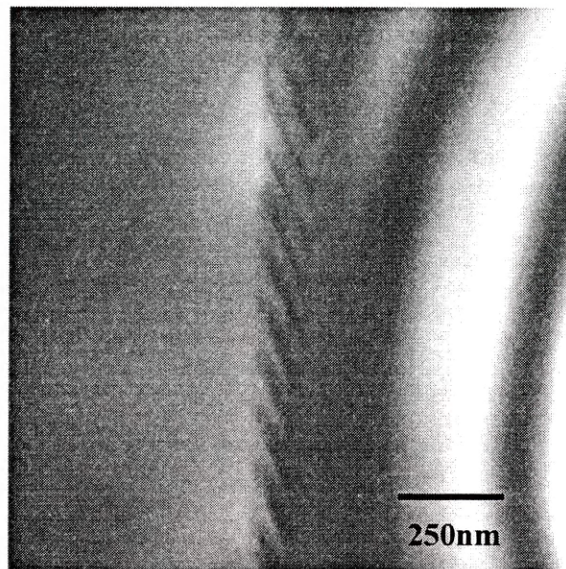
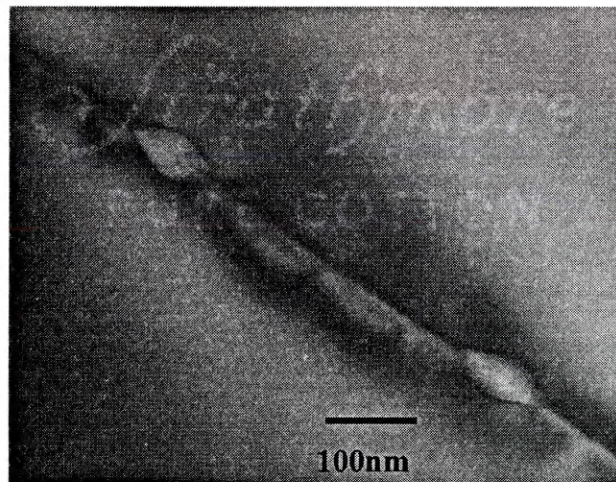


**Figure 5-11 Transmission electron microscopy image of a YAG (YAG1) deformed grain boundary ( $\sim 0.6\% \pm 7\%$ , 20:1). Grain boundary is perpendicular to the image plane along the [001] direction. Testing conditions:  $1600^{\circ}\text{C}$ ,  $3.4 \times 10^{-5}$  in/min crosshead speed, in air. Dislocation strain is observed in this image.**



a)



b)

**Figure 5-12 TEM images of the YAG bi-crystal tested at low stresses. Testing conditions: 1650°C, constant crosshead speed, in air. a) YAG bi-crystal. ~37 degree specimen tilt. 52,000X. Dislocations are observed at the boundary. b) voids found at the boundary (boundary perpendicular to image plane).**

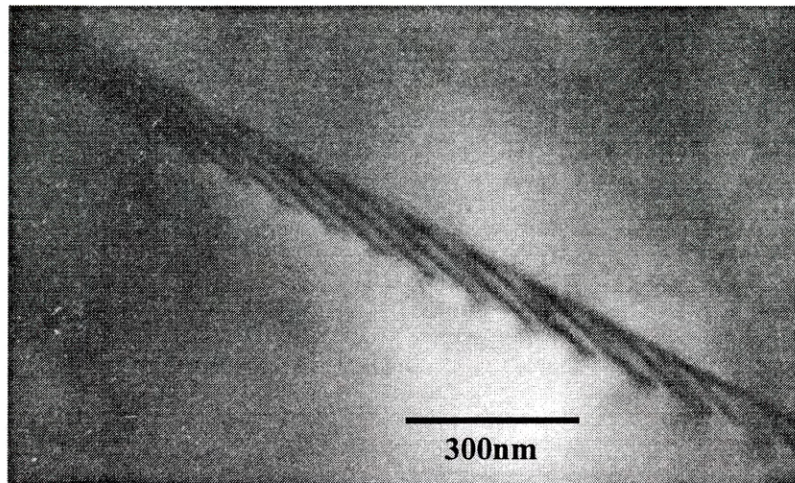


**Figure 5-13 TEM image of YAG bi-crystal tested at high stress. Testing conditions: 1700°C, variable crosshead speed, in air. ~32 degree specimen tilt. 89,000X. A higher dislocation density is observed at the grain boundary compared to the low stress deformed YAG boundary.**

#### ***5.6. SEM of Deformed YAG Bi-crystal***

Using scanning electron microscopy (SEM), the surface of the boundary was observed after deformation. For MP1, fracture of the specimen occurred while removing the sample from the compression unit. The fracture occurred at room temperature and the failure of the specimen was observed to be brittle fracture. Observation of the boundary was possible since the fracture exposed the boundary not located on the surface of the specimen. Figure 5-14 shows the boundary. In the micrograph, there are a number of pores at the boundary.

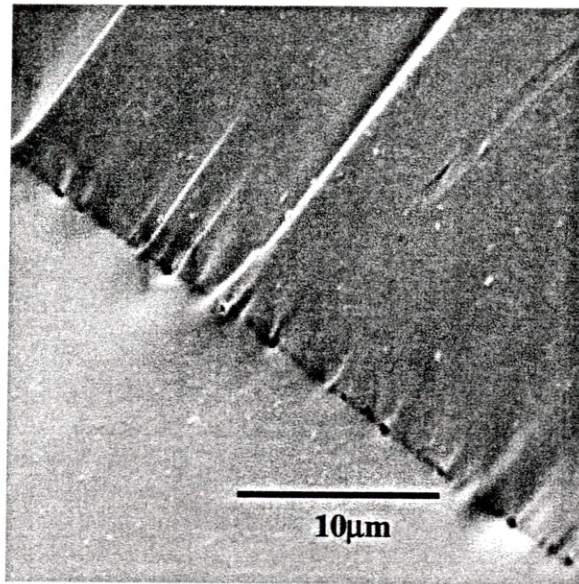


**Figure 5-14 SEM image of voids at the grain boundary of a deformed YAG bi-crystal exposed after fracture at room temperature. Testing conditions: 1600°C,  $3.4 \times 10^{-5}$  in/min crosshead speed, in air. Cavitation results in fracture of ceramics.**

### **5.7. Boundary Steps**

Two different profilometers were used to determine the step heights. A mechanical contact profilometer was used to measure heights on the surface of the first bi-crystal (Dektak 3030 model). These scans were only made on one edge face and one boundary face for one specimen. The scans proceeding these two scans were made with a profilometer which uses optical waves to measure surface height differences (Dektak<sup>3</sup>). All four faces were scanned using the optical profilometer to measure the resulting steps.

Figures 5-15 and 5-16 show the profilometry scans made on sample MP1 with the contact profilometer. For clarity, Figure 5-1 shows which faces each scan was taken at.

The surface of this sample shows that steps were present after deformation, which were not present before deformation. The profilometry scan in Figure 5-15 (including scanning conditions) shows that there is indeed a step and a groove formed at the edge face (Face B) of the boundary for the deformed bi-crystal. Figure 5-15, going from left to right, shows the profilometry scan of first one crystal followed by the grain boundary groove. The step follows the groove and is followed by the second crystal at a lower scan level ( $\sim 5000$  Angstroms lower). The step is measured to be approximately  $0.5 (\pm 0.2)$  microns. However, when the scan was made on the boundary face of this sample, the scan shows a step that is approximately  $2.5 (\pm 0.2)$  microns for the boundary face (Face A). Figure 5-16 shows the scan.

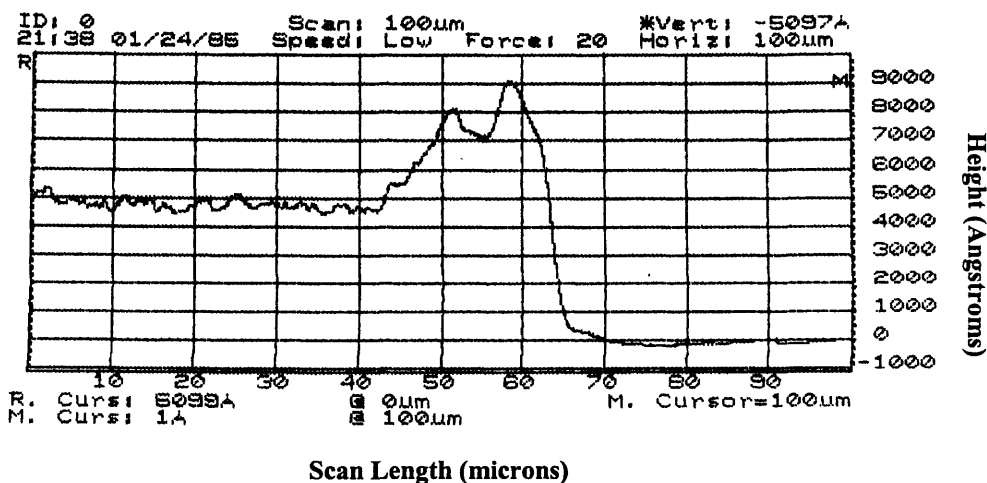


**Figure 5-15 Profilometry scan of a YAG (MP1) bi-crystal boundary face (Face A) surface after deformation. Step size:  $0.5\mu\text{m} (\pm 0.2\mu\text{m})$ .**

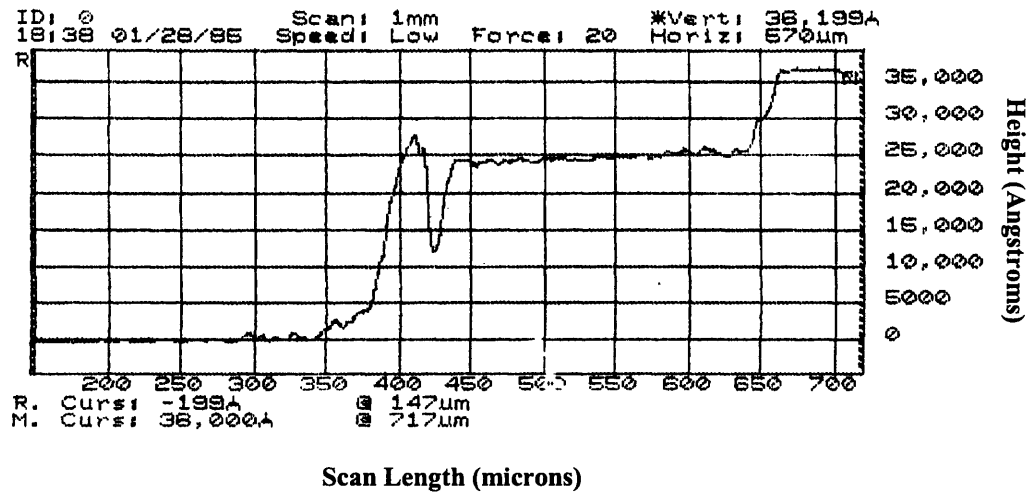


**Figure 5-16 Profilometry scan of a YAG (MP1) bi-crystal edge face (Face B) surface after deformation. Step size:  $2.5 \mu\text{m}$  ( $\pm 0.2 \mu\text{m}$ ).**

To explain the following profilometry results, an explanation of the experimental details for the two scanned samples must be made. The two experiments were made on YAG bi-crystal specimens to try to understand the two mechanisms believed to be responsible for the deformation of the boundary. One experiment, performed on MP7, was a constant stress compression test ( $\sim 60\text{MPa}$ ) and the resulting load-time data are shown in Figure 5-17. Constant stress can be controlled by using the “maximum” and “minimum” control settings on the Instron. The constant stress experiment began with a constant crosshead speed up to a maximum stress of  $60\text{MPa}$  that was maintained for an additional 2 hours. The second experiment, performed on MP6, involved higher crosshead speeds that resulted in a higher stress. The high stress test involved higher stresses ( $\sigma \geq 200\text{MPa}$ ) and a higher testing temperature ( $1700^\circ\text{C}$ ).

The stress-time curve for the low stress experiment is shown in Figure 5-17. Each face of the sample tested at low stresses was scanned with the light profilometer to check for steps. Figures 5-18 to 5-21 show these results.

The resulting deformation in the low stress sample did not produce steps on all faces. Only one scan (Figure 5-21) shows a step of  $\sim 0.1$  microns ( $\pm 0.05$  microns). The second test was performed by increasing the crosshead speed in order to obtain a larger strain and larger stresses (larger than MP7) on the bi-crystal sample. It was expected that the higher testing temperature would result in lower stresses if the strain rate was not varied. The high stress/higher strain rate experiment was performed at the highest temperature ( $1700^{\circ}\text{C}$ ) possible in the furnace. The steps resulting in the sample tested at high stresses are shown in Figures 5-22 to 5-25. Figure 5.1 shows the face each scan was taken at. All faces of the specimen have a step present at the boundary although the steps on each face are not of equal magnitude. All the scans were taken starting from crystal 1 (Figure 5-1) and ending in crystal 2.



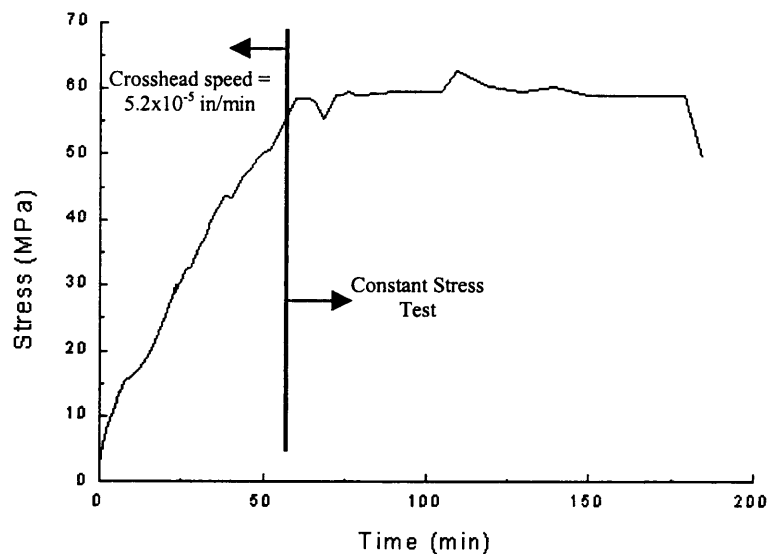


**Figure 5-17** Stress-time curve of constant low stress compression test performed on a YAG bi-crystal at 1650°C. The constant speed, low stress experiment was performed to determine if dislocations play a role the deformation of the boundary in these conditions.

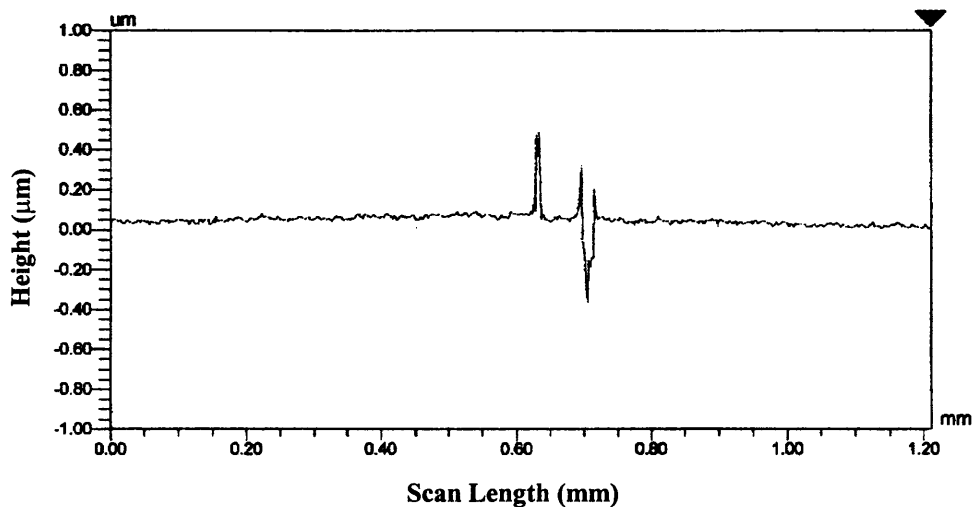


**Figure 5-18** Profilometer scan of a deformed YAG bi-crystal after a constant stress experiment at 1650°C. Scan was made on Face A-side 1. A step at the boundary is not present.

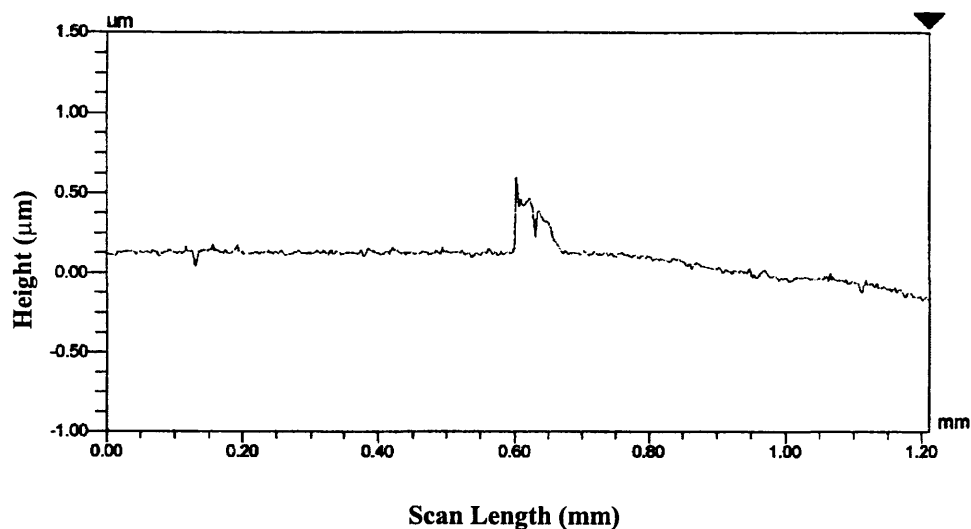


**Figure 5-19** Profilometer scan of a deformed YAG bi-crystal after a constant stress experiment at 1650°C. Scan was made on Face A-side 2. A step at the boundary is not present.

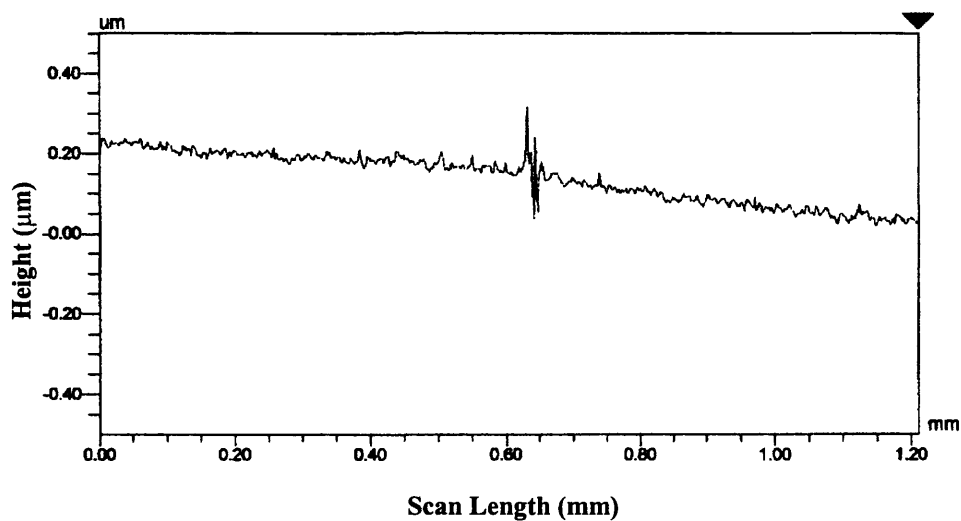


**Figure 5-20** Profilometer scan of a deformed YAG bi-crystal after a constant stress experiment at 1650°C. Scan was made on Face B-side 1. A step at the boundary is not present. The incline is present due to an unlevelled surface.

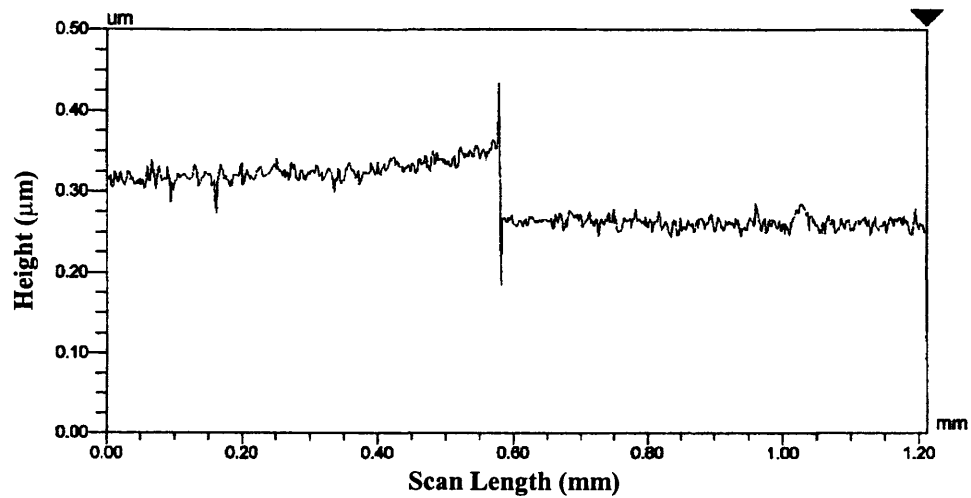


**Figure 5-21** Profilometer scan of a deformed YAG bi-crystal after a constant stress experiment at 1650°C. Scan was made on Face B-side 2. Step size is 0.1 microns ( $\pm 0.04$ microns).

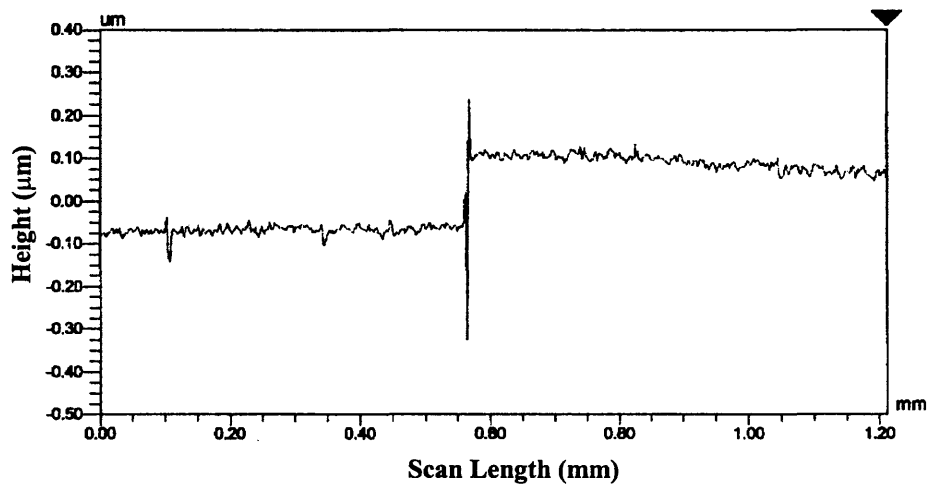


**Figure 5-22** Profilometer scan of a deformed YAG bi-crystal after a constant stress experiment at 1700°C. Scan was made on Face A-side 1. Step size is 0.175microns ( $\pm 0.05$ microns).

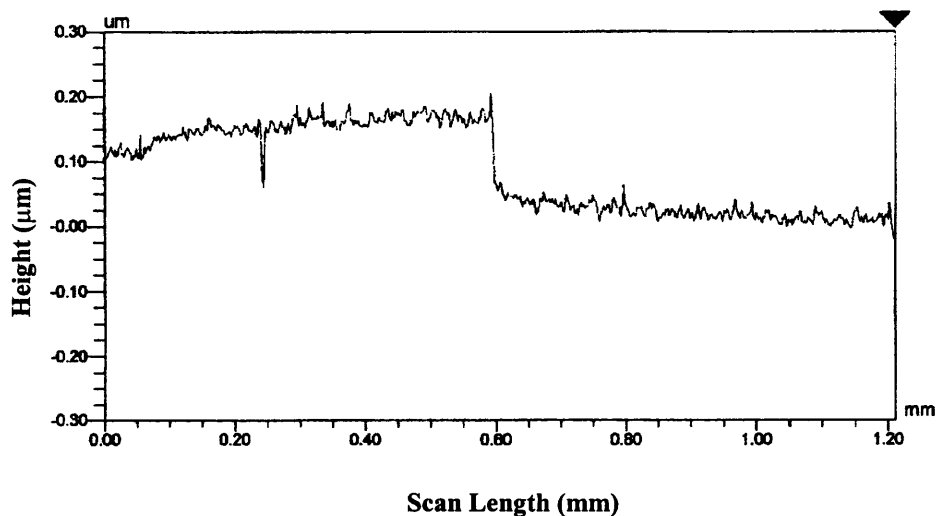


**Figure 5-23** Profilometer scan of a deformed YAG bi-crystal after a constant stress experiment at 1700°C. Scan was made on Face A-side 2. Step size is 0.15 microns ( $\pm 0.05$  microns).

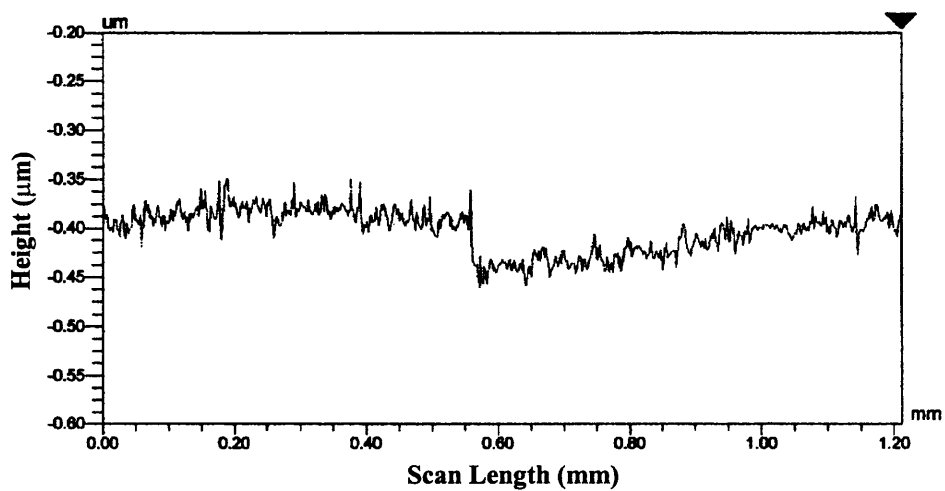


**Figure 5-24** Profilometer scan of a deformed YAG bi-crystal after a constant stress experiment at 1650°C. Scan was made on Face B-side 1. Step size is 0.075 microns ( $\pm 0.037$  microns).

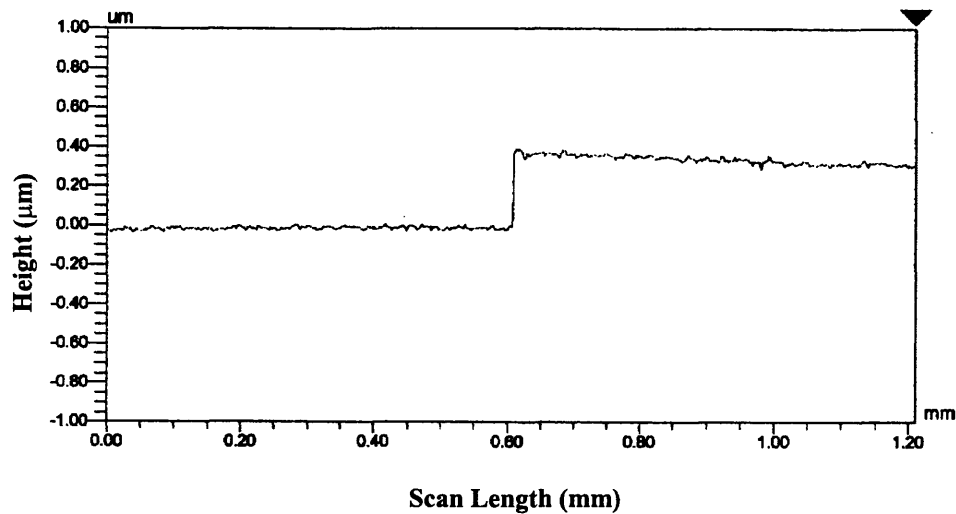


**Figure 5-25** Profilometer scan of a deformed YAG bi-crystal after a constant stress experiment at 1650°C. Scan was made on Face B-side 2. Step size is 0.38 microns ( $\pm 0.02$ microns).

### 5.8. Diffusion Coefficient Measurements

The heat treatments used for Mullin's analysis were performed and the boundary was analyzed for each temperature. Different times were used on a specimen to test for changes in the groove geometry. The preliminary tests, which consisted of annealing one groove for different amount of times, resulted in the growth of the boundary groove at one temperature. The groove "peak-to-peak" distance changed with time and was measured. As shown earlier in Chapter 2, equation 5-1 expresses the kinetics of the groove growth [34].

$$W=(At)^{1/3} \quad (5-1)$$

The growth of the groove was characterized by measuring the growth of the groove peaks of a YAG grain boundary groove three times at a constant temperature of 1600°C and using these measurements to determine the rate exponent ( $s$ ). The experiment consisted of heat treating the boundary for 2.5 hours ( $t$ ) and measuring the peak-to-peak distance ( $W$ ). The groove was heat treated for an additional 5 and 10 hours using the same experimental conditions and  $W$  was measured after each heat treatment. Graph 5-26 shows the results of these measurements with a  $\log W$ - $\log t$  linear relationship. The slope of the line in Figure 5-26 corresponds to the inverse of the rate exponent ( $1/s$ ) in equation 5-1 that in turn corresponds to the diffusion mechanism governing the growth of the groove [34]. The value calculated for  $1/s$  is  $0.346 \pm 0.045$ . The calculated value for the stress exponent ( $s=2.6$  to  $3.3$ ) corresponds to the groove growth by a volume diffusion mechanism. Figure 2-19 expresses that the rate exponent is 3 for volume diffusion [34].

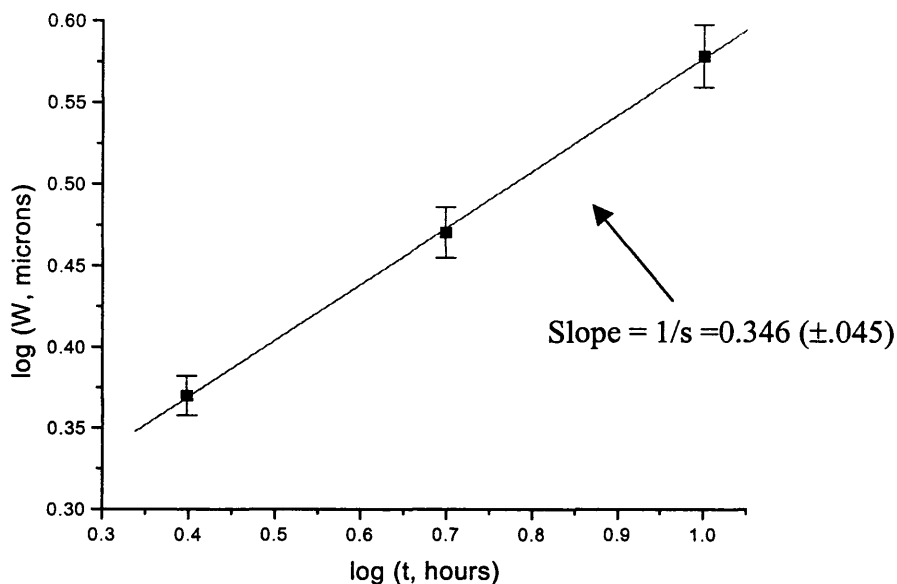


**Figure 5-26 Linear relationship between the groove growth and time for the YAG bi-crystal. The slope of the  $\log W$  and  $\log t$  line is the inverse of the stress exponent ( $s$ ). The value of the stress exponent calculated from this line identifies volume diffusion as the groove growth mechanism.**

As time increased, the geometry of the groove deteriorated. The deterioration of the groove included shape changes that made the groove asymmetrical and the elimination of the groove completely. The geometry changed from a typical groove to a mass pile-up as shown in Figure 5-27. The best time for heat treatment of the YAG bi-crystals was found to be between 2.5 hours for temperatures  $\leq 1625^\circ\text{C}$ , 1 hour for  $1650^\circ\text{C}$  and 30 minutes for  $1700^\circ\text{C}$ .

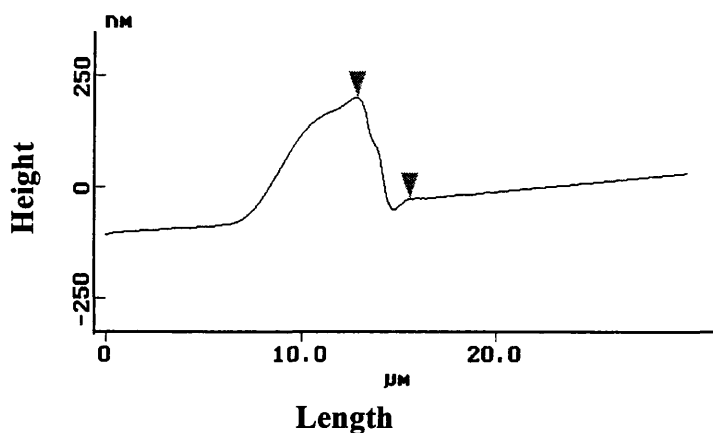


**Figure 5-27 Mass pile up of the YAG bi-crystal boundary shown in an atomic force microscopy scan. A mass pile-up is indicative of grain boundary migration or asymmetrical diffusion.**

During AFM scanning of the heat treated grooves, the geometry of the groove along the length of the boundary was found to be inconsistent. Figure 5-28 shows a schematic of the different observed geometries along the length of the boundary. For the measurements used in calculating the diffusion coefficient, the only acceptable groove geometry had to fall between 5-28a and 5-28b. The acceptable groove geometry was based on two details: 1) the groove depth ( $d$ ) is at least  $\sim 25\%$  of the groove height ( $h$ ), and 2) The groove is symmetrical about the boundary plane.

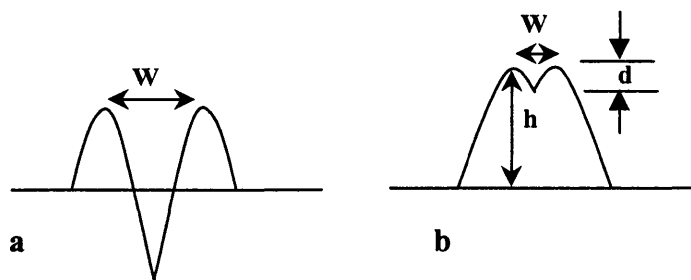


**Figure 5-28 Acceptable grain boundary groove geometries. a) Preferred groove geometry. b) Acceptable groove geometry ( $d/h > .25$ )**



Using equations 2-5 and 2-6, the diffusion coefficients for YAG at different temperatures were calculated. The value for the atomic volume used ( $\Omega$ ) was  $1.73 \times 10^{-21} \text{cm}^3$ . The value for surface energy used was  $2500 \text{ ergs/cm}^2$  (alumina surface energy value at  $1650^\circ\text{C}$ ). The value for the number of atoms per unit volume ( $n$ ) used was  $9.23 \times 10^{22} \text{ atoms/cm}^3$ . Table 5-2 summarizes the "peak-to-peak" distances measured for each temperature.

Using  $W$ , the "peak-to-peak" distance on the grain boundary grooves, and equations 2-5 and 2-6, the volume diffusion coefficients were calculated for each temperature. These values were plotted as  $\ln D$  vs.  $1/T$  as shown in Figure 5-29. Using equation 2-8, the activation energy of the diffusion process was found to be  $\sim 330 \text{ kJ/mol}$  ( $\pm 75 \text{ kJ/mol}$ ).

**Table 5-2 Details of the "peak-to-peak" measurements made on the YAG bi-crystalline material to determine the diffusion coefficient at different temperatures.**

Temperature ( $^\circ\text{C}$ )	Heat treatment time (min)	Average "peak-to-peak" distance ( $W$ ), nm ( $\pm 5\%$ )	Diffusion Coefficient $\text{cm}^2/\text{sec}$ ( $\pm 15\%$ )
1550	150	1040	9.1 E-15
1587	150	835	4.7 E-15
1625	150	957	74 E-15
1663	60	1020	2.3 E-14
1700	30	957	3.8 E-14

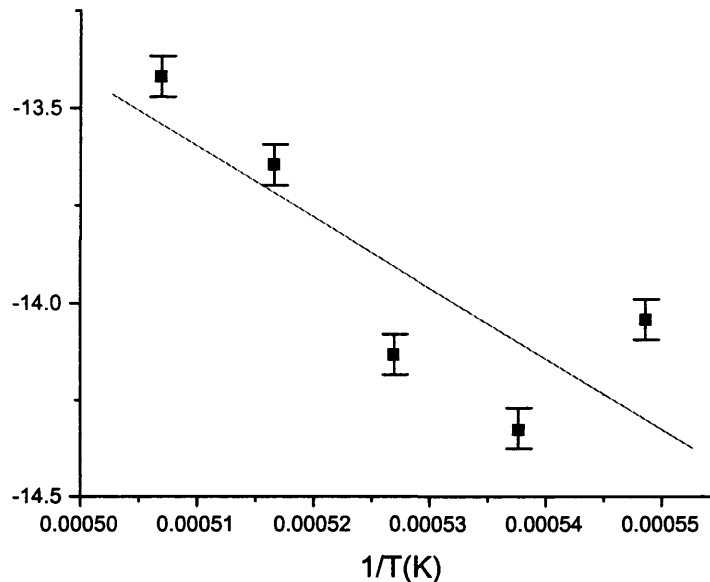


**Figure 5-29 Graph of the diffusion and temperature data with error bars. The slope of this line is used to calculate the activation energy of the diffusion process in the temperature range of 1550 to 1700°C. The error bars represent 15% error for the diffusivity data.**

### **5.9. Geometry of Boundary Grooves**

For the boundary face (Face A) of the compression samples, non-symmetrical grooves were observed throughout the length of the boundary. Figure 5-30 shows the typical non-symmetric groove found for an edge face. Although these grooves cannot be used to calculate the diffusion of the material, the lack of geometry of the grooves indicates that the kinetics of the groove growth is dependent on boundary/surface angle and stresses applied on the boundary.

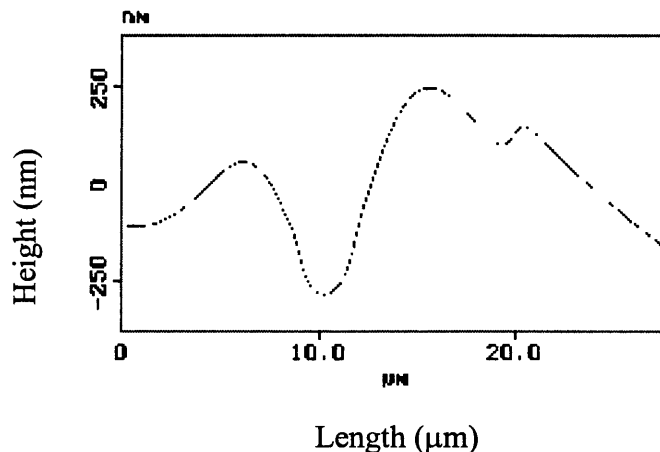


**Figure 5-30 Atomic force microscopy scan of a migrating grain boundary as seen on a compression sample of the YAG bi-crystal after heat treating. The residual groove indicates grain boundary migration.**

The grain boundary grooves on the edge face of a compressed sample also resulted in an interesting geometry shown in Figure 5-31. A residual groove (A), which is a mass of material left behind when a boundary migrates, is observed in the AFM scan.

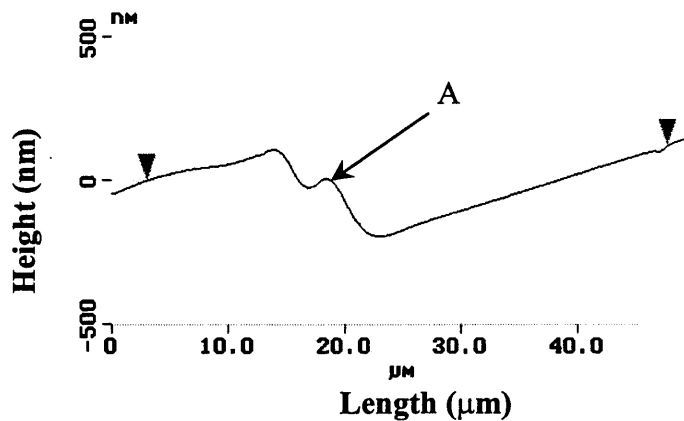


**Figure 5-31 Atomic force microscopy profile showing a residual groove in a YAG bi-crystal compression sample after deformation. The step at the boundary and the asymmetry of the groove indicates that both diffusion and migration may be responsible for the deformation of this boundary.**

## 6. DISCUSSION

The results presented in the previous section all suggest that two major mechanisms could be involved in the deformation of the  $\Sigma 5$  YAG boundary. These mechanisms involve either dislocations at the boundary and/or the diffusion of cations or anions near and around the boundary. In the present section, the specific role of each general mechanism is discussed.

### 6.1. Grain Boundary Quality

#### 6.1.1. Undeformed Boundary (Dislocations)

TEM results obtained from Geoff Campbell on the undeformed YAG  $\Sigma 5$  boundary reveal that relatively few dislocations exist in the vicinity of the boundary [5]. TEM micrographs are shown in Figure 6-1 and 6-2. Figure 6-1 shows a contrast pattern that suggests that arrays of dislocations are present at the boundary. More typically, no evidence for the presence of dislocations was observed (Figure 6-2). It is likely that the dislocations that are present at the boundary were produced during the processing of the bi-crystal by a slight misalignment between the bi-crystals or by surface polishing error.

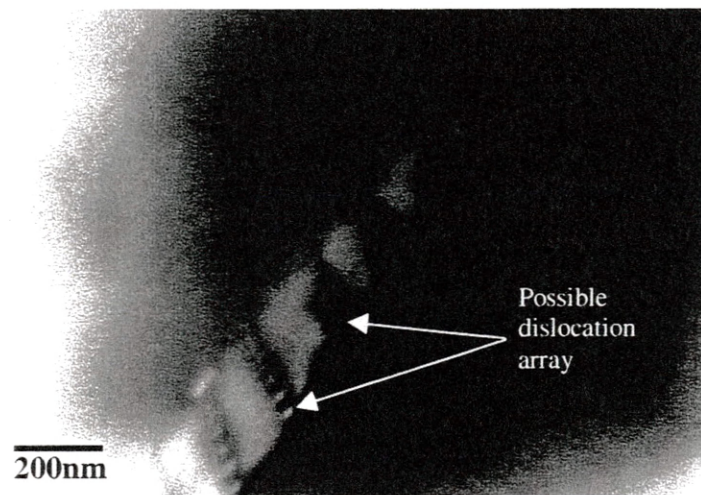


Figure 6-1 TEM of  $\Sigma 5$  YAG grain boundary before deformation [5]. Possible dislocations are present at the boundary. The strain fields indicate this possibility.

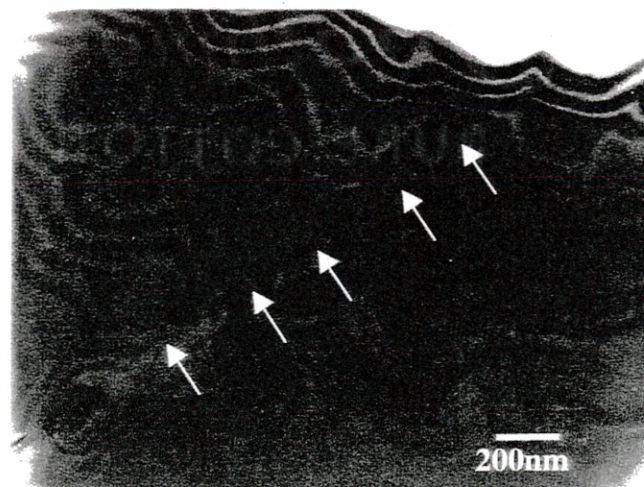
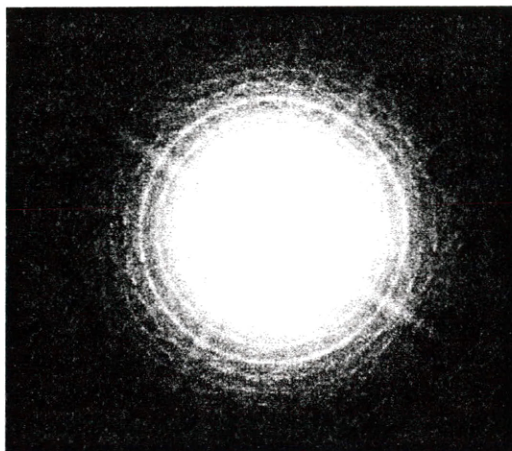


Figure 6-2 Micrograph of the undeformed YAG boundary [5]. The fringe patterns are believed to be an artifact of specimen preparation. An extensive dislocation structure is not present before deformation of the boundary. The dotted line represents the location of the boundary.

### 6.1.2. *Orientation Misfit*

Slight misorientations between crystals prior to bonding result in misfit dislocations and the crystal misorientation was examined. Kikuchi patterns were used as a tool for calculating the misfit of the grain boundary. Kikuchi patterns result from the elastic scattering of electrons. The scattered electrons produce Kikuchi lines that are sensitive to orientation of the crystal since the scattering of electrons is dependent on Bragg's Law. Kikuchi lines can be used to determine crystal orientation or, for the bi-crystals, misorientation [17]. A Kikuchi pattern was taken adjacent to the grain boundary on one crystal and another pattern was taken across the boundary in the adjacent crystal. These Kikuchi patterns are shown in Figures 6-3 and 6-4. The patterns show that there is a slight misfit of the (210) plane across the boundary.

The Kikuchi pattern should show a complete 180° rotation from one crystal to the other because the boundary was produced by cutting along the (210) plane and rotating the crystals 180° about each other. Based on these Kikuchi patterns, the misfit for the YAG  $\Sigma 5$  grain boundary is calculated to be  $\sim 0.1^\circ$ . Since all the boundaries were made in a nearly identical manner, it is assumed that the misfit is representative of all the bi-crystals examined here.



**Figure 6-3** TEM Kikuchi pattern taken from one grain of the bi-crystal using an electron microscope.

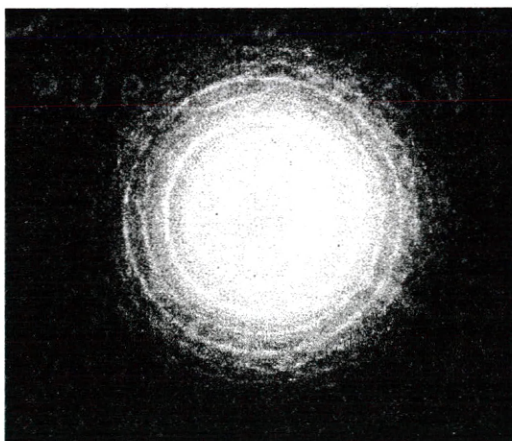


**Figure 6-4** TEM Kikuchi pattern taken from second grain in the YAG bi-crystal. The 180 degree rotation to form the  $\Sigma 5$  boundary is almost perfect. The misfit of the boundary was found to be only  $0.4^\circ$ .

## 6.2. *Bi-crystal Orientation*

The results of the Laue analysis show that all of the samples were cut at the same orientation consistent with the above Kikuchi patterns. Thus, their Laue patterns are identical as shown in the typical Laue scan in Figure 5-4 and are all shown in the Appendix. It was assumed that, since the orientation of all the samples are identical, the boundaries would behave similarly under similar stress and temperature conditions.

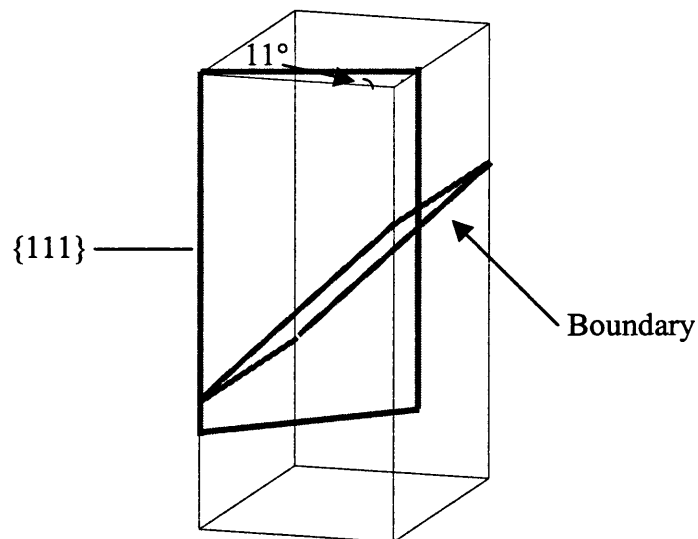


**Figure 6-5 YAG bi-crystal showing the boundary plane and the {111} family of planes as determined by an x-ray technique. All the bi-crystals were machined in this orientation.**

The orientation at which the samples were cut such that the (111) plane is  $\sim 11^\circ$  ( $\pm 1^\circ$ ) degrees from the edge boundary plane. Figure 6-5 shows the position of the (111)



plane with respect to the compression sample as determined by the Laue patterns. The orientation determination (including the Laue indexing) is used to determine if sliding directions are preferred sliding directions for the orientation of the bi-crystals.

### ***6.3. The Role of Grain Boundary Steps (Grain Boundary Sliding)***

The observations made through the profilometry technique (for sample MP1 and MP6) to measure steps formed at the grain boundary during high temperature deformation indicate that the two bonded single crystals slid past each with the components in the directions shown in Figure 6-6. In Table 6-1, MP1 is also summarized although only two faces of the bi-crystal were measured.

Based on the fact that the Schmidt factor is largest along the direction of arrow P in Figure 6-6, it would be expected that sliding would occur only in that direction. However, the sliding occurred such that there was a component of slip in the S direction as shown in Figure 6-6 for samples MP6 and MP1. The observation that a component of sliding also exists along direction S indicates that crystallography is important. Specifically, the directional dependence on sliding suggests that dislocations control sliding.

**Table 6-1 Measured steps using a profilometer for the high stress and low constant stress experiments on YAG bi-crystalline compression samples.**

<i>Face Measured</i>	<i>MP6 (High stress) (<math>\pm x \mu\text{m}</math>)</i>	<i>MP7 (Low constant stress) (<math>\pm x \mu\text{m}</math>)</i>	<i>MPI (<math>\pm x \mu\text{m}</math>)</i>
Boundary Face (side 1)	0.2 $\mu\text{m}$ (0.05)	0 $\mu\text{m}$	2.5 (0.3)
(side 2)	0.12 $\mu\text{m}$ (0.05)	0 $\mu\text{m}$	Not measured
Edge Face (side 1)	0.38 $\mu\text{m}$ (0.02)	0 $\mu\text{m}$	0.5 (0.3)
(side 2)	0.05 $\mu\text{m}$ (0.04)	0.25 $\mu\text{m}$ (0.04)	Not measured

The steps at each face, however, are typically not of equal magnitude. For example, for sample MP6, the height of the steps on the boundary face are 0.2  $\mu\text{m}$  and 0.12  $\mu\text{m}$  while the steps on the edge faces are considerably different from each other. Specifically, the height of one step is 0.05 $\mu\text{m}$  and the other is 0.4 $\mu\text{m}$ . The anisotropy or the presence of different sized steps at each face of the samples suggests that sliding is not a homogeneous process along the entire boundary/surface line. Others have observed that the sliding rates of the same bi-crystals can vary significantly due to local inhomogeneities, such as poor bonding areas and impurities at the bonded surfaces [22].

Thus, the difference in step sizes observed here is not surprising. However, sliding studies in metals have not revealed any directional sliding as is observed here.

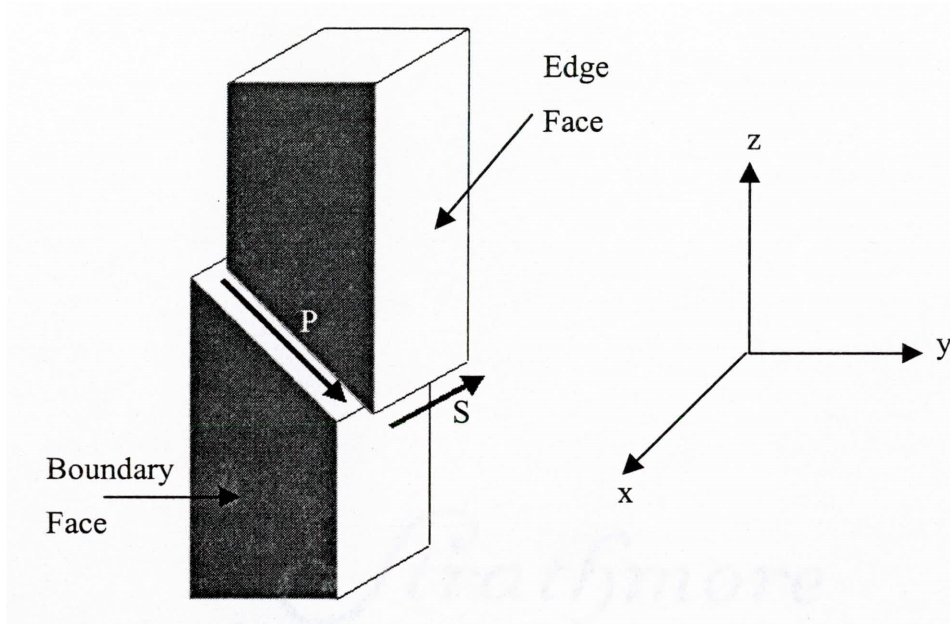


**Figure 6-6 Relative movement of bi-crystals past each other. The axis shows that the boundary has moved in all three directions. The boundary did not slide only in the expected P direction.**

To address the relative importance of diffusion and motion of dislocations at the boundary, a high stress ( $\sim 200\text{MPa}$ ) and a low constant ( $60\text{MPa}$ ) stress experiment were conducted. The philosophy behind conducting these two experiments was based on altering the relative driving force for diffusion and dislocation motion. In particular, the high stress experiment was designed to increase the driving force for dislocation motion. Past work has revealed the stress dependence of deformation mechanisms, as summarized in Figure 6-7 [9]. Specifically, high stresses activate intragranular dislocation motion

whereas low stresses activate diffusion aided mechanisms. Dislocations, requiring higher stresses than diffusion, will become more active as the stress is increased. For low stress deformation, only diffusion of atoms is occurring and dislocations are not activated. Figure 6-7 also compares the creep behavior of ceramics as the grain size changes. Small grain size materials more likely deform from diffusional deformation mechanisms.

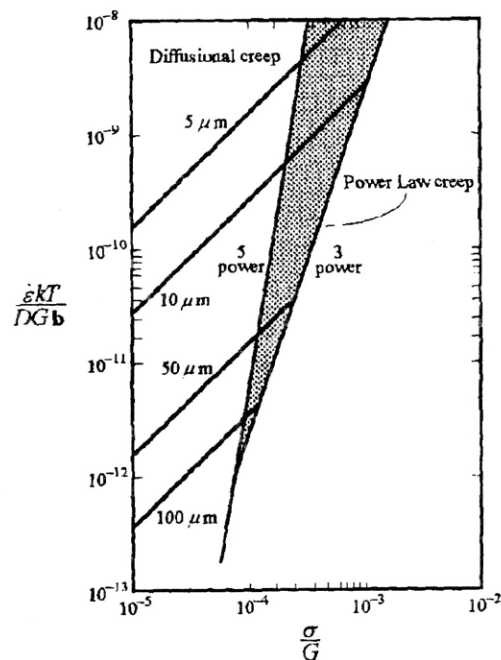


**Figure 6-7 Graph illustrating the stress dependence of diffusion and dislocation mechanisms in ceramics [9]. Higher stresses activate dislocation deformation mechanisms whereas low stresses only activates diffusion aided deformation mechanisms.**

While the magnitude of the stress necessary to activate dislocations was not known, a stress of 60 MPa was chosen for the constant stress experiment based on earlier

observations made on low stress compressed experiments that resulted in small plastic strain.

The results from the high stress experiment compared with the low constant stress experiment (MP7 and MP6, table 6-1) suggests that for each of the conditions, a different mechanism governs the deformation of the boundary. The directionality of the deformation of the high stress sample (MP6) suggests a dislocation aided deformation mechanism. The lack of steps in the S component suggests that for the low stress sample, a non-slip (diffusion controlled) mechanism is governing the deformation of the boundary because slip occurred only in the P direction as shown in Figure 6-6 and based also on the profilometry scans taken of the low stress sample (Figures 5-18 through 5-21). However, for the high stress experiment, steps at the boundary are distinct and indicate directional sliding. Thus, it is sustained that dislocation movement is governing the grain boundary sliding direction in the bi-crystal.

For a compression sample (MP1), the steps measured on one boundary face and one edge face were 2.5 microns and 0.5 microns, respectively as shown in Figures 5-15 and 5-16. The step measurements were used to calculate the apparent grain boundary sliding direction for this sample. The calculated angle at which this boundary moved is  $79^\circ (\pm 1^\circ)$  as shown in Figure 6-8. The angle of sliding compares with  $53^\circ (\pm 1^\circ)$  for sample MP3 in which the direction of the oblong features were used as a measurement of the sliding direction. The angles of slip for these two samples, however are not preferred slip directions for either crystal as determined by Laue comparison.

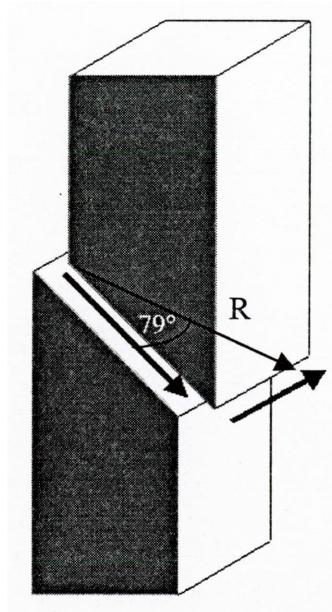


**Figure 6-8 Direction of slip of one YAG bi-crystal determined by surface step measurements. The boundary slid 79 degrees from the P direction.**

As with the other measurements (MP6), the sliding result direction unequivocally reveals that there is directionality to the deformation of the boundary. The directionality implies that dislocations, being dependent on orientation and structure, govern boundary deformation. The directionality could not be attributed to diffusion since the diffusion of anions/cations should not be directional.

#### ***6.4. Deformation Grain Boundary Shape***

The oblong features on the fractured deformed boundary face (MP3) shown in Figure 5-8 were scanned in the atomic force microscope to reveal the height of the

features. An undeformed boundary surface is shown in Figure 5-7 by surface features which are distinctly different from the deformed oblong surface features. The features (Figure 6-9) are long troughs which are directional and are inclined at  $53^\circ (\pm 1^\circ)$  to vector P in Figure 6-6. Since these troughs were produced during sliding, their direction should be indicative of the sliding direction. The directionality of the deformed boundary suggests once again that dislocations govern the deformation of the boundary.

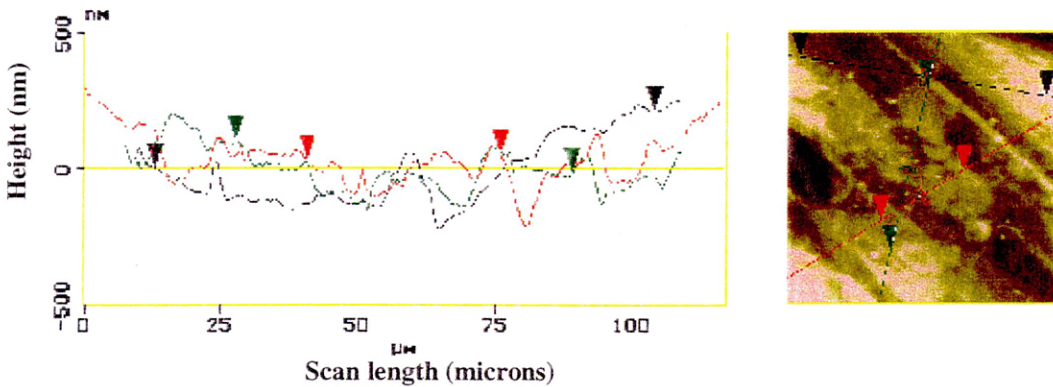


**Figure 6-9 AFM scan and profiles of the fractured YAG bi-crystal boundary surface. The features are measured to be a maximum of 250nm high.**

The calculated sliding direction was further examined by comparing it to the indexing of Laue patterns obtained for the bi-crystal. From the Laue indexing analysis, it was found that the features were not located on a major slip direction for YAG for either of the crystals. One approach to explain the directionality of slip would be to examine the grain boundary structure in more detail to understand possible dislocation structures

within the boundary. It would be expected that the motion of grain boundary dislocations would be restricted to particular well-defined directions. It is hypothesized that a sufficient understanding of the atomic arrangement of the grain boundary would provide a rationale for describing the directional slip observed in the present study. The boundary structure analysis, however, is not considered in the present study.

### **6.5. *The Role of Dislocations at the Boundary***

All TEM analyses of the bi-crystal boundary have shown that dislocations exist at the boundary. However, it is important to separate the dislocations present before deformation (Figure 6-1) from the dislocations produced during deformation (Figures 5-9 to 5-13).

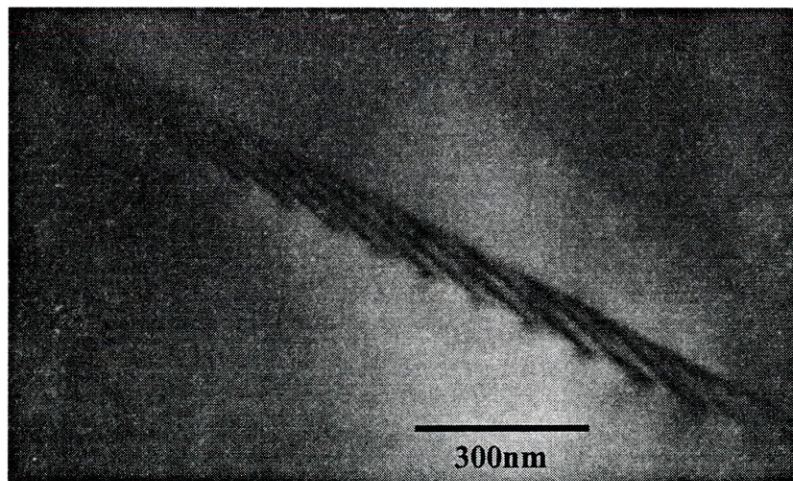


**Figure 6-10 TEM image of YAG bi-crystal boundary deformed under a high stress. A dislocation spacing of 84nm ( $\pm 5$ nm) was measured.**



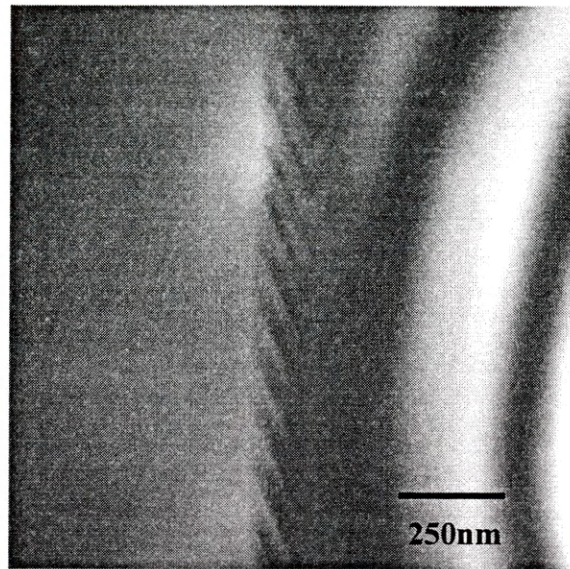


**Figure 6-11 TEM image of YAG bi-crystal boundary deformed under a constant low stress. A dislocation spacing of 113nm ( $\pm 6$ nm) was measured.**

From TEM performed on the undeformed YAG boundary, dislocations are present at the boundary; however, they are not as extensive in number as for the deformed YAG boundaries. The dislocation spacings for the low stress and high stress samples were measured. The high stress compression sample has a line dislocation spacing of 84nm ( $\pm 5$ nm) and is shown in Figure 6-10. The dislocation spacings were measured by using TEM images of each boundary perpendicular to the plane of the image. The constant low stress sample (MP7) tested at 1700°C has a line spacing measured from Figure 6-11 to be 113nm ( $\pm 6$ nm). The decrease in dislocation spacing (i.e. increase in dislocation density) is approximately 34%. Thus, it was observed that the dislocation density between the undeformed and the deformed bi-crystals increased. An increase in the observed dislocation density between the low and high stress experiments is also observed.

### 6.5.1. *Dislocations at Grain Boundaries*

The mechanism by which dislocations interact with grain boundaries can vary significantly depending on factors such as grain boundary structure, impurity levels at grain boundaries, Burger's vector, temperature and other various factors. Dislocations can move by a process of dislocation climb, glide, a combination of both and can change their character through other mechanisms such as dislocation splitting (formation of partial dislocations).

The  $\Sigma 5$  YAG grain boundary was made by rotating the crystal structure 180 degrees about plane A in Figure 6-12 [36]. An atomic model was used to represent the grain boundary but the model did not use atomic bond strengths to model the grain boundary structure. The resulting model of the grain boundary structure is complex and is shown in Figure 6-13. Figure 6-13 shows a view in the [001] direction [36]. The model does not take into account possible dislocations at the boundary and the situation has not been examined.

The pinning of a dislocation to a grain boundary can effectively change the structure of the grain boundary. For the grain boundary structure shown in Figure 6-13, the positioning of atoms at the grain boundary is quite structured. Under applied stresses or by thermal energy, lattice dislocations can move along glide planes or by a climb mechanism towards the structured boundary and can result in the formation of a step at

the grain boundary as shown in Figure 6-14 for a simple grain boundary structure of zinc [38]. Figure 6-14a depicts a symmetric boundary without a dislocation where Figure 6-14b is a drawing of the grain boundary after a lattice dislocation has interacted with the grain boundary. For a larger angle grain boundary, a step is produced after a lattice dislocation interacts with the boundary and is shown in Figure 6-14d [38].

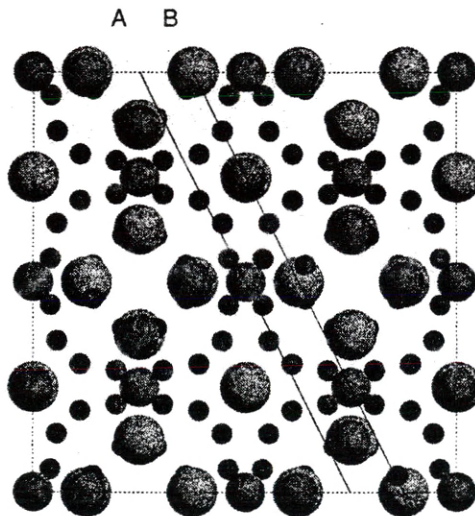


**Figure 6-12 YAG crystal structure viewed along [001] direction showing two possible planes which will result in grain boundary symmetry when rotated 180 degrees. There are a number of possibilities for modeling the grain boundary structure of the (210)  $\Sigma 5$  YAG grain boundary [36].**

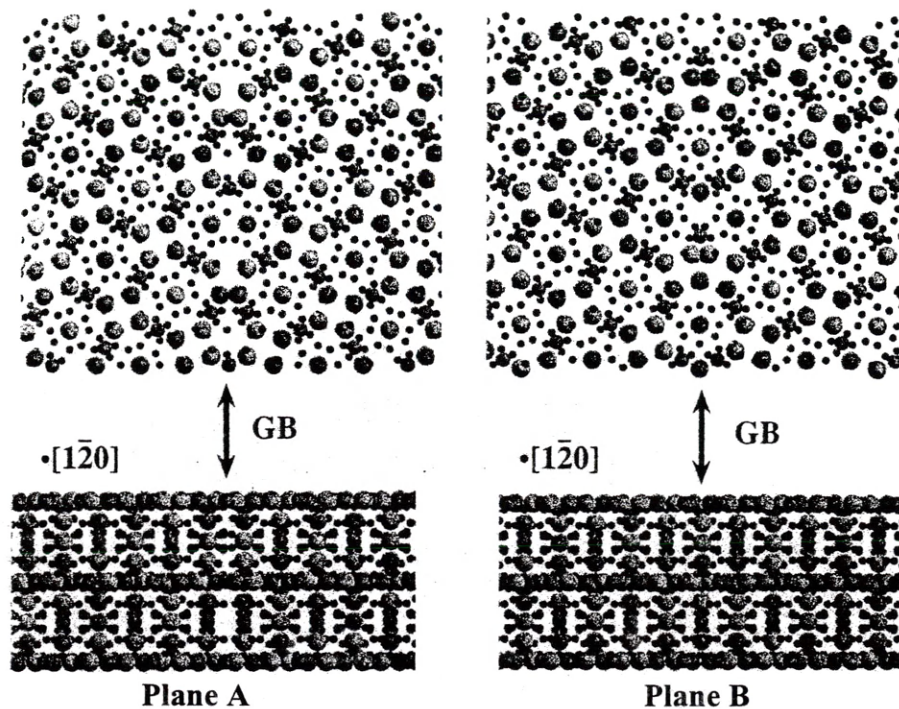


**Figure 6-13** Resulting grain boundary atomic positioning for planes A and B resulting from an atomic model. A top view of the model shows the structure formed at the boundary [36]. The modeling of grain boundary structure with dislocations has not been attempted.

The interaction of the dislocation at the boundary can be difficult to determine. For body centered cubic materials and for large unit cells (which produce large Burger's vectors), dislocation splitting provides a lower energy defect. For example, the  $1/2[111]$  Burger's vector can split to 2 vectors ( $1/2[111] + 1/3[111]$ ) or three ( $1/8[110] + 1/4[112] + 1/8[110]$ ) depending on the plane of splitting. Figure 6-15 shows some of the possible split dislocations [39].

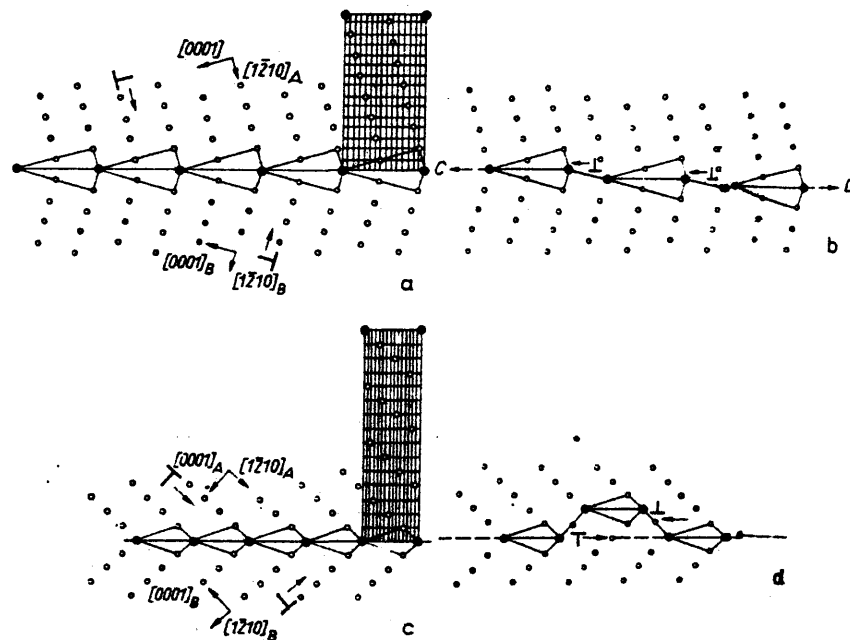


**Figure 6-14 Two symmetric grain boundaries shown before dislocation and boundary interaction (14-a, c) and after interaction (14b,d). The different grain boundary angles result in different grain boundary structure after dislocation and boundary interaction. Steps from after the dislocation and boundary interaction [38].**

Once at the grain boundary, dislocations can also move about the grain boundary plane. Arzt et al. define an atomistic model for interface controlled creep [40]. The model defines the grain boundary as a path for dislocation climb as opposed to a purely diffusional creep where the grain boundary is a perfect sink for matter as shown in Figure 6-16 [40]. The dislocation model takes into account the structure of the boundary and uses the dislocations present at the boundary to account for the creep of the material. The model compares favorably to experimental results for creep of materials that cannot be described with “Nabarro-Herring” and “Coble” creep. Dissociation of dislocations is

believed to be possible since the Burger's vector of the dislocation must be part of the boundary structure and not of the lattice dislocations or the dislocation could move out of the boundary [48].

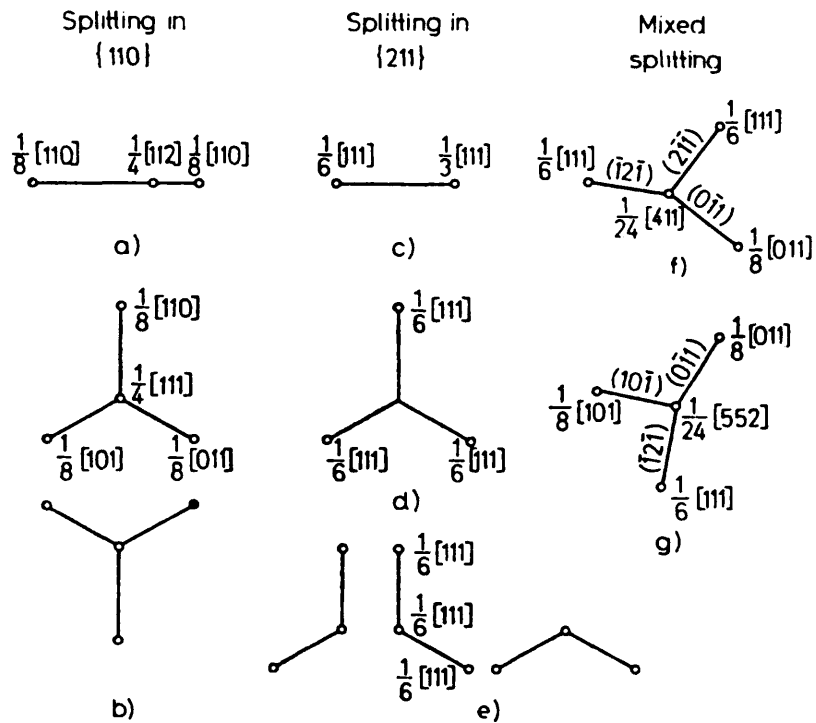


**Figure 6-15 Possible dislocation splitting for BCC materials. Dislocation splitting results in lower energy defects and provides a means by which dislocations can change when they interact with boundaries such that their movement is restricted to the grain boundary plane [39].**

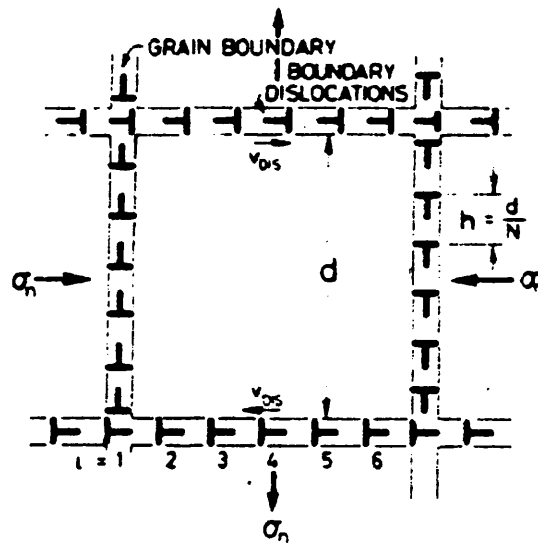


**Figure 6-16** A simple sketch showing the movement of dislocations moving along the grain boundary of a grain. A stress provides the energy necessary to allow the dislocation to move by a climb process [40].

### 6.6. Migration of YAG Grain Boundary (Grain Boundary Mobility)

An interesting outcome of the grooving observations was the geometry differences found for the grain boundary grooves produced after heat treatment and compression of the bi-crystals. Figure 5-30 shows a typical residual groove formed on the edge face during compression testing. Residual grooves are common during the migration of grain boundaries. The residual groove and the grain boundary groove are  $4.7 \mu\text{m}$  ( $\pm 0.1 \mu\text{m}$ , 20:1) apart. The scanned sample was tested for 2.5 hours, indicating an average grain boundary migration rate of  $\sim 2 \mu\text{m}/\text{hour}$ .

The presence of migration in these studies indicates that the YAG boundary is mobile (i.e. there is significant atomic movement at the boundary) and would open the

possibility to large changes in the shape of the grain boundary. The migration (most probably not homogeneous throughout the boundary) would change the boundary shape as discussed by Raj and Ashby [22]. The grain shape change would explain the presence of the oblong features on the boundary surface of the fractured compression sample (MP3). The presence of these features is attributed to the diffusion and migration of the boundary under stresses and high temperatures.

The migration of the boundary was not expected to occur for the  $\Sigma 5$  YAG boundary, as the driving force for migration (impurities and curvature) was not significantly present [25]. However, it has been pointed out that coincident site lattice boundaries are not sensitive to impurities [25]. The lack of residual grooves on the boundary face (Face A) suggests that driving force for the observed migration is the angle at which the boundary intersects the surface of the sample which is  $45^\circ$  for the edge face.

#### ***6.7. Cavitation Deformation of YAG Boundary***

Cavitation under compression has been observed to occur for alumina as well as various other polycrystalline ceramics [41, 30]. Two conditions must exist for cavitation to initiate. First, there must be an irregularity (steps, or other stress concentrator) at the boundary, which is capable of inducing large stresses. Second, large stresses must be formed at these irregularities (generally 5 to 20 times the applied stress) [30]. For ceramics which do not have a grain boundary glassy phase, the mechanism of cavitation is vacancy diffusion towards the cavity. Vacancy diffusion cavitation involves the



sliding of grains against each other. Grain boundary sliding produces large localized stresses at irregularities followed by the nucleation of cavities. The growth and coalescence of the cavities can induce failure in the material if cavitation is extensive [9].

There were two observations made to suggest that a mechanism of deformation for the YAG boundary involves cavitation. Voids were observed through SEM analysis for one compressed bi-crystal (MP1, Figure 5-14) and through TEM analysis of MP7, the low constant stress tested bi-crystal and is shown in Figure 6-17 noting the measured voids. The voids observed using the SEM (sample MP1) in the deformed boundary are sub-micron. The voids found in the TEM (MP7, the low constant stress experiment) in Figure 6-17 are also sub-micron in size (~100nm). The shapes of the voids appear to be spherical for MP1 and ellipsoidal for MP7 and agree with possible void shapes used for modeling creep cavitation [30]. The observed void formation for the YAG boundary is consistent with cavitation formation in materials in general.

The formation of these voids suggests that diffusion is an important mechanism in the deformation of the boundary and for an irregular boundary [30], cavitation can play a vital role in the deformation of the YAG bi-crystal boundary. For these two samples, low stresses (~50MPa) were used to deform the boundary. Voids were not found for any of the other observed boundaries for different testing conditions.

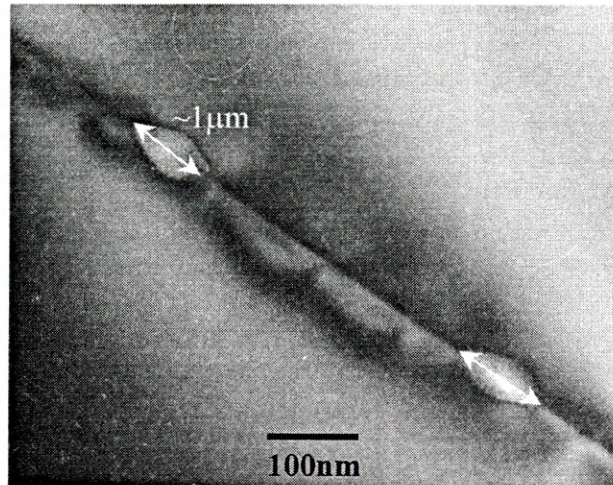


**Figure 6-17 TEM of the MP7 YAG bi-crystal showing voids approximately 1nm ( $\pm 0.2$ nm) along the axis of the boundary. Voids are a form of accommodating plastic deformation at grain boundaries.**

#### **6.8. Observations on Migration and Sliding**

Clear examples of migration in materials can be found for metallic systems. Previous experiments on metals have observed surface deformation at grain boundaries of bi-crystals using marker lines as shown in Figure 6-18 [23,24]. Ando [23] performed tensile tests on zinc bi-crystals that gives clear evidence of migration and sliding occurring in one tensile test. However, the two processes can occur independent of each other. As seen by the micrograph, the marker lines have been broken and are slanted. Slip lines and the migration of the boundary result in the broken marker lines. The observations made by Ando have also been made on aluminum material [23, 42, 43, 44]. The movement of the grain boundary in the migration and grain boundary sliding

processes, although they are independent processes, are thought to be correlated. Figure 6-19 shows the correlation between grain boundary sliding and grain boundary migration.

The process by which boundaries migrate and slide is complex and can involve mechanisms aided by both dislocations and diffusion. Further study of these two processes is needed to more clearly understand their relationship.

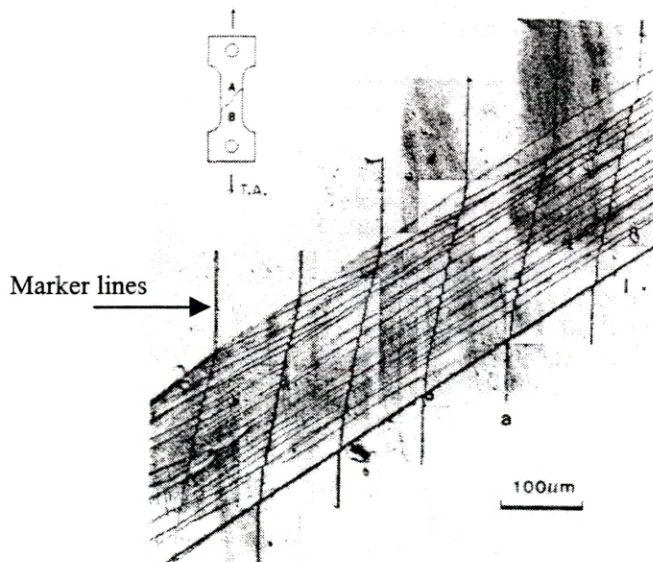


**Figure 6-18 Surface of a zinc bi-crystal showing the movement and shape change of marker lines [23]. Slip and migration occurred in the zinc bi-crystal.**

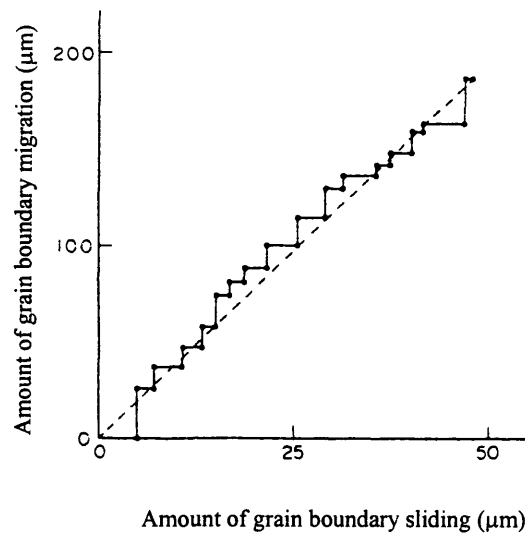


**Figure 6-19** The correlation between grain boundary sliding and grain boundary migration for a zinc bi-crystal [23]. The correlation is  $\sim 4:1$ , migration to sliding distances.

### 6.9. Observations on Dislocations

The role of dislocations present at the grain boundary and the observation of an increased number of dislocations after deformation can be more clearly understood by comparing the results found here with bi-crystalline studies performed on other materials. In a study of a  $\Sigma 13$  silicon grain boundary, dislocations were observed at the grain boundary after deformation [45]. These dislocations were a combination of intrinsic dislocations and the interaction of the grain boundary and lattice dislocations. These interactions resulted in the formation of partial dislocations at the grain boundary. Figure 6-20 shows a TEM micrograph of the boundary and the dislocations present and Figure 6-21 shows a detailed sketch of the different dislocations present at the boundary.

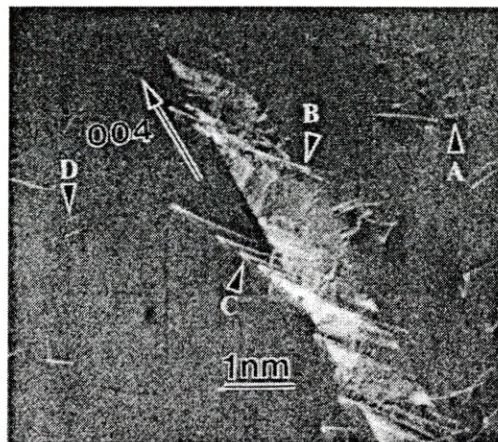


**Figure 6-20 TEM micrograph of a deformed silicon grain boundary with intrinsic and partial dislocations [45]. Partial dislocations are a result of lattice dislocations interacting with the boundary.**

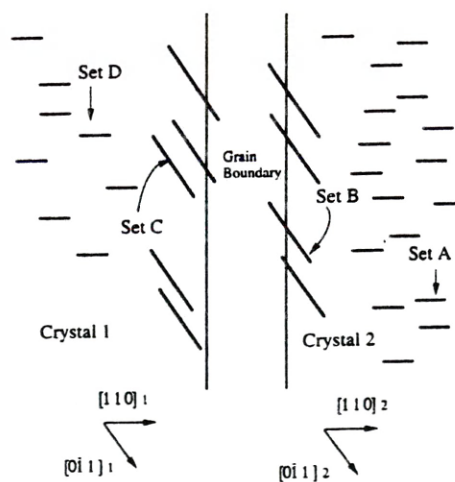


**Figure 6-21 Sketch of the different dislocations present at a deformed silicon grain boundary [45]. An analysis of the boundary resulted in the presence of different sets of dislocations.**

Lopez discussed the possibility of dislocation pinning at the grain boundary during grain boundary migration. The increasing dislocation density could be attributed

to the added dislocations at the grain boundary as the boundary migrates. Although bulk dislocations were not observed in the limited TEM analysis done on the YAG boundaries, previous single crystal results [4] have shown that dislocations are present in the bulk of YAG. Thus, it is possible that the increase in dislocation density found in the YAG boundaries is a result of the dislocation pinning as seen by Lopez.

Although misfit dislocations are present for the YAG boundary studied here, the increase in the number of dislocations with increased applied stress suggests that a multiplication process occurred. However, the lack of lattice dislocation observation suggests that the increase in dislocation density occurred at the grain boundary and not by lattice dislocation motion towards the boundary as was observed by Sagalowicz [45]. The analysis of the dislocations at the YAG boundary was not possible here but it is feasible that dislocations are being pinned at the boundary after moving under applied stresses.

#### ***6.10. Diffusion Coefficient Calculations***

The grain boundary grooving experiments have produced values for the diffusion coefficient at 5 different temperatures and are summarized in Table 5-2. Using these calculated diffusion coefficient values, and assuming self diffusion, a prediction of the average atomic movement (M) can be made using Equation 6-4 [46].

$$M = \sqrt{4D_v t} \quad (6-1)$$

M is the average distance an atom moves in the bulk of the material. The values for M range from 0.12 $\mu\text{m}$  to 0.22 $\mu\text{m}$  ( $\pm 8\%$ ) and are summarized in Table 6-2. The calculation for the atomic movement of atoms will give a further understanding of the role diffusion plays in the deformation of the boundary since the atomic movement is on the same order of magnitude as the step heights observed (Table 6-1). The calculated atomic movement values suggest that deformation of the boundary can be affected by the diffusion of atoms in YAG. Diffusion along the grain boundary can result in combined diffusion aided deformation mechanisms such as migration, cavitation and diffusion accommodated sliding. Thus, these combined processes can locally deform the boundary extensively.

**Table 6-2 Average atomic distances traveled by the YAG atoms in 2.5 hours.**

Temperature ( $^{\circ}\text{C}$ )	Average atomic distance traveled in 2.5 hours ( $\mu\text{m}$ ) ( $\pm 8\%$ )
1550	0.18
1625	0.13
1650	0.16
1663	0.28
1700	0.36

The activation energy of the diffusion of YAG in the range of 1550 to 1700°C is calculated by constructing a graph of the diffusion coefficient and temperature, as shown in Figure 5-30. The correlation between  $\log D$  and  $1/T$  results in a linear function which is described in equation 2-8. The slope ( $m$ ) of the linear function is related to the activation energy ( $Q$ ) of the diffusion mechanism and the activation energy as follows [47]:

$$Q = 2.3R(m) \quad (6-2)$$

The slope of the curve in Figure 5-30 was -18,300 and the activation energy was calculated to be ~330 kJ/mol ( $\pm 75$ kJ/mol). The equation which describes the diffusion of the YAG bi-crystals is:

$$D(Y_3Al_5O_{12}) = 3.9 \times 10^{-10} \exp(-330 \pm 75(kJ/mol)/RT) \quad (6-3)$$

The calculated value for the activation energy of the diffusion mechanism is similar to the activation energy of the diffusion of oxygen in YAG found by Haneda (~297-325kJ/mol) suggesting that the diffusion of oxygen is limiting the formation of the grain boundary grooves.

The study of other materials using Mullins theory [30], in particular alumina and magnesia are discussed here. The diffusion mechanism by which alumina grooving develops is surface diffusion. The equation which describes the diffusion of alumina is [48]:



$$D_{Al_2O_3} = 0.48 \exp\left(\frac{-256(kJ/mol)}{RT}\right) m^2 / s \quad (6-4)$$

A study performed on a SrTiO<sub>3</sub> bi-crystal by employing Mullins theory with the aid of an atomic force microscope resulted in the diffusion expressed as [49]:

$$D_{SrTiO_3} = 2.12 \times 10^3 \exp\left(\frac{-440(kJ/mol)}{RT}\right) m^2 / s \quad (6-5)$$

Since surface diffusion is controlling the diffusion of these other studies, the possibility of surface rather than volume diffusion was considered. The diffusion coefficients (calculated between 1600 and 1700°C) were calculated assuming surface diffusion and were in the order of 10<sup>-9</sup> and 10<sup>-10</sup> cm<sup>2</sup>/sec compared with the calculated values of 10<sup>-14</sup> and 10<sup>-15</sup> cm<sup>2</sup>/sec for volume diffusion. However, the activation energy assuming surface diffusion is also in the order of 300kJ/mol. Thus, for the possibility of pure surface diffusion controlling the formation of the grain boundary groove, the diffusion of the oxygen ions is controlling the groove growth rate.

The calculated value for the activation energy of diffusion of YAG in the present study does not agree with the activation energy of the creep diffusion in the polycrystalline YAG study [31]. The difference in activation energy can be accounted to the role of a possible dislocation mechanism interacting with the diffusion creep for the polycrystalline study. These dislocation mechanisms may include grain boundary sliding assisted by dislocation, dislocation disassociation and intragranular slip [24].

Furthermore, the grain geometry between the polycrystalline material studied by Parthasthary [31] and the bi-crystals studied here is drastically different.

### ***6.11. Deformation Mechanisms.***

The results of the mechanical tests and diffusion tests YAG suggest that at least two mechanisms are responsible for the deformation of the boundary. One mechanism is controlled by diffusion of oxygen in the YAG bi-crystal. Diffusion is responsible for the formation of voids at the boundary, migration of the boundary and a possible diffusion aided grain boundary sliding mechanism. Cavitation or void formation is possible through a vacancy diffusion mechanism.

The other activated mechanism is a dislocation mechanism that results in the directional deformation of the YAG bi-crystal as seen in the step formation at the bi-crystal surface and the directional features at the surface of a deformed grain boundary. The increase in the dislocation density, as the applied stress on the bi-crystal boundary is increased, suggests that dislocations play a vital role in the deformation of the boundary. The increase in dislocation density results from the multiplication of grain boundary dislocations and not from the interaction of lattice dislocations with the grain boundary since lattice dislocations were not found in the bi-crystals.

## 7. SUMMARY

The following is a summary of the observed deformation at the YAG boundary after deformation in compression:

- 1) Sub-micron step formation at the boundary/surface intersection was observed after deformation.
- 2) Dislocation multiplication at the grain boundary was observed using transmission electron microscopy and was measured. An increase in the dislocation density is also observed at the boundary after deformation.
- 3) Grain boundary shape change was observed as directional oblong features and are a result of the deformation of the boundary.
- 4) Migration of the boundary was observed and is approximately 2 $\mu\text{m/hr}$ .
- 5) Diffusion coefficients for four temperatures were measured using grain boundary grooving experiments.
- 6) Activation energy of the diffusion of YAG in the temperature range of 1550 to 1700°C was calculated from the diffusion coefficient values to be ~330kJ/mol ( $\pm 75\text{kJ/mol}$ ) which compares with the published value of 300 to 325kJ/mol for the diffusion of oxygen in YAG [1].

$$D(\text{Y}_3\text{Al}_5\text{O}_{12}) = 3.9 \times 10^{-10} \exp(-330 \pm 75 (\text{kJ/mol}) / RT) \text{m}^2/\text{s}$$

Although diffusion at high temperatures is responsible for some of the deformation at the boundary, the directionality of the deformation of the YAG boundary suggests that the slip deformation of the boundary occurred with the aid of a dislocation mechanism. The increase in dislocation density at the boundary, coupled with the lack of a preferred slip system of either crystal also suggests that the directionality of the deformation is governed by the grain boundary structure.

## APPENDIX

### *Determination of Crystal Orientation Using the Backscatter Laue Technique*

Laue patterns consists of diffraction spots collected on film. These spots are generated by the Bragg diffraction of x-ray beams from planes in a single crystal. For backscatter Laue, the spots form hyperbolas that reflect the planes from one pole as shown in Figure A-1.

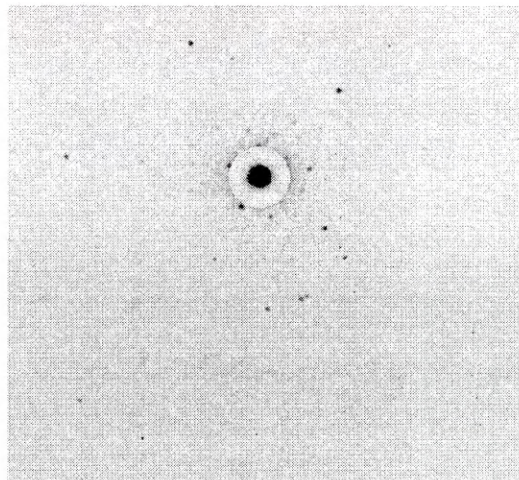


**Figure A- 1 Backscatter Laue pattern for MP3 showing the hyperbolas produced by the diffraction spots.**

Different approaches are possible for determining the orientation of single crystals. The major intersections (spots which have various hyperbolas intersecting) on

the Laue pattern are identified by two angles,  $\delta$  and  $\gamma$ . A Greninger chart (Figure A-2) is used to identify both these angles. The correct Greninger chart must be used to correspond to the correct camera length. For the scans taken, the camera length was 3cm.

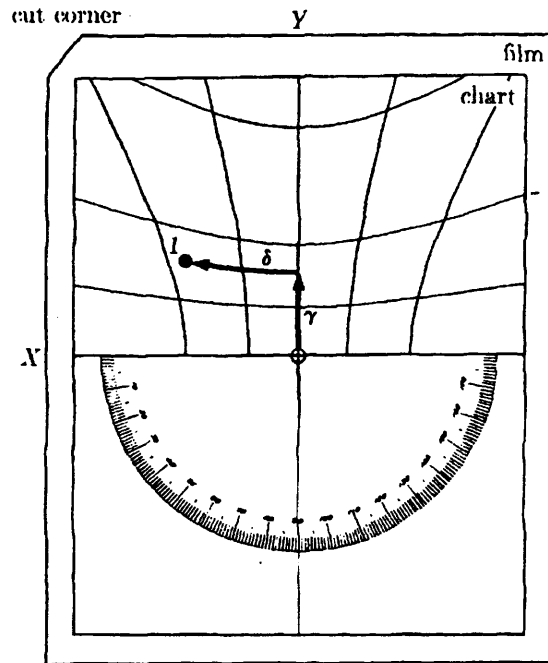


**Figure A- 2 Greninger chart used to identify the angles on a backscatter Laue diffraction pattern [49].**

Each spot of major intersection is plotted on a tracing paper which is placed over the Wulff net (Figure A-3). The tracing paper can then be spun about the center of the Wulff net to index the pattern. To index, a chart of interplanar angles for the material crystal structure is used. For YAG, cubic interplanar angles was used (Figure A-4).

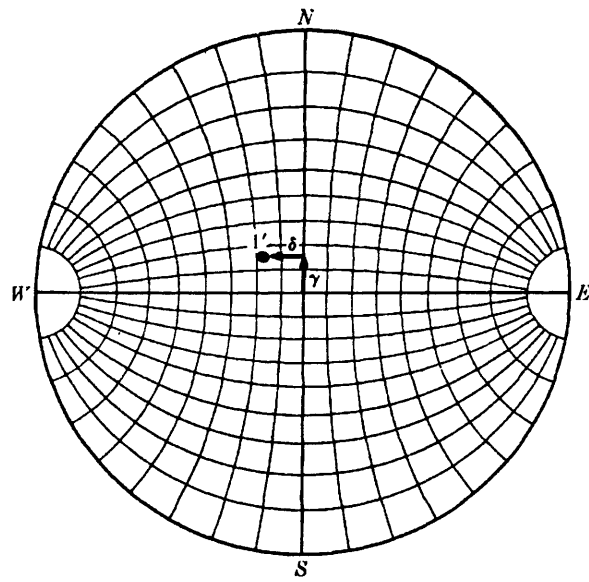


**Figure A- 3 Wulff net used with the Greninger chart to translate the Laue spots for indexing [49].**

Indexing can be a trial and error process that begins with taking two spots and rotating the tracing paper such that the two points lie on a great circle (shown in Figure A-3). The number of units between the spots is the angle between the planes. The planar angles are compared to the angles in the chart (Figure A-4). However, this must be done between at least 3 spots to begin eliminating planes. The elimination process is continued until spots of interest are indexed. For a more detailed explanation the Wulff net and spot patterns see Edington [50].

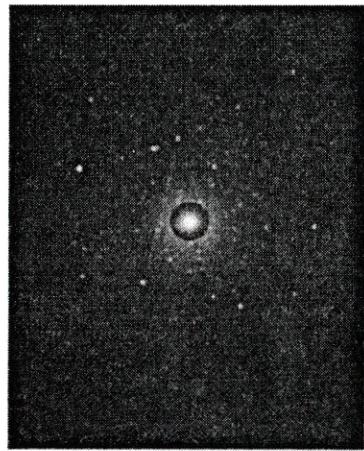
$\{h_2k_2l_2\}$	$\{h_1k_1l_1\}$						
	100	110	111	210	211	221	310
100	0						
	90						
110	45	0					
	90	60					
		90					
111	54.7	35.3	0				
		90	70.5				
			109.5				
210	26.6	18.4	39.2	0			
	63.4	50.8	75.0	36.9			
	90	71.6		53.1			
211	35.3	30	19.5	24.1	0		
	65.9	54.7	61.9	43.1	33.6		
		73.2	90	56.8	48.2		
		90					
221	48.2	19.5	15.8	26.6	17.7	0	
	70.5	45	54.7	41.8	35.3	27.3	
		76.4	78.9	53.4	47.1	39.0	
		90					
310	18.4	26.6	43.1	8.1	25.4	32.5	0
	71.6	47.9	68.6	58.1	49.8	42.5	25.9
	90	63.4		45	58.9	58.2	36.9
		77.1					
311	25.2	31.5	29.5	19.3	16.0	25.2	17.6
	72.5	64.8	58.5	47.6	42.4	45.3	40.3
		90	80.0	66.1	60.5	59.8	55.1
320	33.7	11.3	36.9	7.1	25.2	22.4	15.3
	56.3	54.0	80.8	29.8	37.6	42.3	37.9
	90	66.9		41.9	55.6	49.7	52.1
321	36.7	19.1	22.2	17.0	10.9	11.5	21.6
	57.7	40.9	51.9	33.2	29.2	27.0	32.3
	74.5	55.5	72.0	53.3	40.2	36.7	40.5
		90					
331	46.5	13.1	22.0				
510	11.4						
511	15.6						
711	11.3						

Largely from R. M. Bozorth, *Phys. Rev.* 26, 390 (1925); rounded off to the nearest 0.1°. A much longer list is given on p. 120-122 of Vol. 2 of [G.11].

**Figure A- 4 Table of interplanar spacings for a cubic material [49].**

Figures A-5 show all the Laue scans obtained for the bi-crystals. Note that Figure A-5d is the scan for the standard sample used for diffusion coefficient measurements.

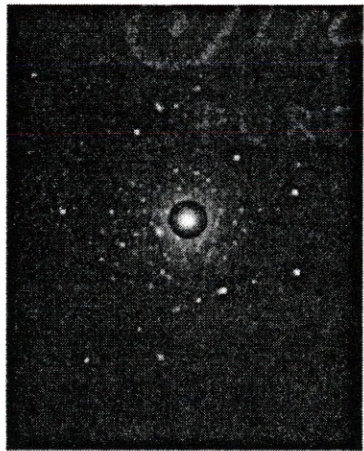




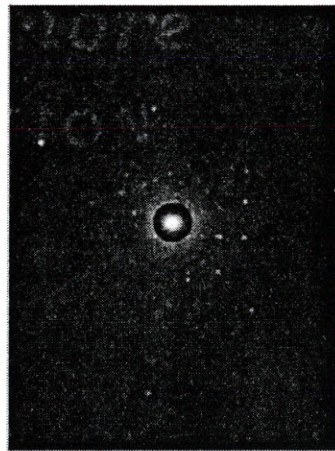
a)



b)



c)



d)

**Figure A- 5 Laue Patterns a) MP7, b) MP6, c) MP8 and d) diffusion standard sample.**

## REFERENCES CITED

1. H. Haneda, Y. Miyazawa and S. Shirasaki, *J. of Cryst. Growth*, 68 (1984) 581.
2. T. Watanabe, *Mat. Sci and Engr. A*, 166 (1993) 11.
3. G.S. Corman, *J. Mater. Sci. Lett.*, 12 (1993) 379.
4. W.R. Blumenthal and D.S. Phillips, *J. Am. Ceram. Soc.*, 79 no. 4 (1996) 1047.
5. G. Campbell, personal interaction.
6. W.D. Kingery, H.K. Bowen, D.R. Uhlmann, **Introduction to Ceramics**, 2<sup>nd</sup> Edition, John Wiley & Sons, New York (1960).
7. T. Hirano, *Scripta Metall. Mater.*, 25, (1991) 1747.
8. T. Hirano, *Acta Metall.*, 38 (1990) 2667.
9. M. Barsoum, **Fundamentals of Ceramics**, The McGraw-Hill Companies, New York NY (1997).
10. F.R.N. Nabarro, **Proceedings of Conference on Strength of Solids**, Physical Society, London (1948).
11. C. Herring, *J. Appl. Phys.*, 21 (1950) 437.
12. R.L. Coble, *J. Appl. Phys.*, 34 (1963) 1679.
13. R.F. Cook, G.M.K. Pharr, *Structure and Properties of Ceramics*, M.V. Swain (editor), Volume 2, VCH Publishers, New York (1994).
14. I.M. Lifshitz, *Soviet Phys. JETP*, 17 n.4 (1963) 909.
15. T.G. Langdon, *Mat. Sci. and Engr. A*, 166 (1993) 67.
16. K.J. Roberts, *J. of Mat. Sci.*, 16 (1981) 2517.
17. D. Hull, **Introduction to Dislocations**, 2<sup>nd</sup> Edition, Pergamon Press, Great Britain (1975).

18. J. Weertman, *J. Appl. Phys.*, 28 (1957) 362.
19. F.R.N. Nabarro, *Philos. Mag.* 16 (1967) 231.
20. C.R. Barret, W.D. Nix, *Acta Metall.*, 13 (1965) 1247.
21. W.A. Rachinger, *J. of the Inst. Of Metals*, 81 (1952-1953) 33.
22. R. Raj and M.F. Ashby, *Met. Trans.*, 2 (1971) 1113.
23. H. Ando, J. Sugita, S. Onaka, and S. Miura, *J. of Mat. Sci. Lett.*, 9 (1990) 314.
24. A.D. Sheikh-ali, *Acta Materialia*, 45 n.8 (1997) 3109.
25. D.A. Smith, *Mat. Sci. Forum*, 94-96 (1992) 221.
26. P. Shewmon and G. Meyrick, **Interface Migration and Control of Microstructures**, edited by Pande, Smith, King and Walter, ASM (1985)(7-17).
27. J.D. Pan and R.W. Balluff, *Acta Metal.*, 30 (1982) 861.
28. Fu-sen Chen and A.H. King, *Scripta Metal.*, 20 (1986) 1401.
29. C. Li and M. Hillert, *Acta Metal.*, 29 (1981) 1949.
30. C.R. Blanchard and K.S. Chan, *J. Am. Ceram. Soc.* 76 n.7 (1993) 1651.
31. T.A. Parthasarathy, T. Mah and K. Keller, *J. Amer. Ceram. Soc.*, 75 n.7 (1992) 1756.
32. W.W. Mullins, *Trans. Metall. Soc. AIME*, 218 (1960) 354.
33. M. Jin, E. Shimada, Y. Ikuma, *J. Mater. Res.*, 14 n.6 (1999) 2548.
34. B.C. Allen, *Trans. Am. Inst. Min. Engrs.*, 245 (1969) 1621.
35. S. Karato, Z. Wang and K. Fujino, *J. Mat. Sci.*, 29 (1994) 6458.
36. G. Campbell, *J. Am. Ceram. Soc.*, 79 n.11 (1996) 2883.
37. S.J. Kline, F.A. McClintock, *Mech. Eng.* 75 (1953) 3.
38. A.D. Sheikh-Ali, R.Z. Valiev, *Phys. Stat. Sol. (a)* 117 (1990) 429.
39. I. Kovacs, L. Zsoldos, *Dislocations and Plastic Deformation*, Edited by D. Ter Haar, Pergamon Press, Budapest (1973).
40. E. Arzt, M.F. Ashby, R.A. Verrall, *Acta Metall.* 31 n.12 (1983) 1977.
41. R. Raj, *Acta Met. Soc. AIME*, 233 (1965) 305.
42. F. Weinburg, *Trans. Met. Soc AIME*, 233 (1965) 305.
43. F.B. Cuff and N.J. Grant, *Trans. Met. Soc. AIME*, 212 (1958) 355.

44. J.L. Walter and H.E. Cline, *Trans. Met. Soc. AIME*, 242 (1968) 1823.
45. L. Sagalowicz and W.A.T. Clark, *Phil. Mag. A*, 72 n.3 (1955) 561.
46. R.J. Borg, G.J. Dienes, **An Introduction to Solid State Diffusion**, Academic Press, New York (1988).
47. R.E. Reed-Hill, **Physical Metallurgy Principles**, 2<sup>nd</sup> Edition, PWS Engineering, Boston MA (1973).
48. A. Tsoga, *J. Amer. Ceram. Soc.*, 77 n.4 (1994) 954.
49. M. Jin, E. Shimada, Y. Ikuma, *J. Mat. Res.*, 14 n.6 (1999) 2548.
50. B.D. Cullity, **Elements of X-Ray Diffraction**, 2<sup>nd</sup> Edition, Addison-Wesley Publishing, Reading MA (1978).
51. J.W. Edington, **Typical Electron Microscope Investigations**, Philips, Great Britain (1976).